Analytic and numerical treatment of an effective lattice theory for heavy QCD at zero and finite density

Dissertation
zur Erlangung des Doktorgrades
der Naturwissenschaften

vorgelegt beim Fachbereich Physik
der Johann Wolfgang Goethe-Universität
in Frankfurt am Main

von
Anh Quang Pham
aus Nam Dinh, Vietnam

Frankfurt am Main 2022
D30

vom Fachbereich Physik der
Johann Wolfgang Goethe-Universität als Dissertation angenommen.

Dekan: Prof. Dr. Harald Appelshäuser

Gutachter: Prof. Dr. Owe Philipsen
Prof. Dr. Dirk Rischke

Datum der Disputation:

TO MY FAMILY

Analytic and Numerical Treatment of an Effective Lattice Theory for Heavy QCD at Zero and Finite Density

Anh Quang Pham[1]

Institut für Theoretische Physik, Goethe-Universität Frankfurt, Max-von-Laue-Str. 1, 60438 Frankfurt am Main, Germany

Abstract

We discuss aspects of the phase structure of a three-dimensional effective lattice theory of Polyakov loops derived from QCD by strong coupling and hopping parameter expansions. The theory is valid for the thermodynamics of heavy quarks where it shows all qualitative features of nuclear physics emerging from QCD. In particular, the SU(3) pure gauge effective theory also exhibits a first-order thermal deconfinement transition due to spontaneous breaking of its global Z_3 center symmetry. The presence of heavy dynamical quarks breaks this symmetry explicitly and consequently, the transition weakens with decreasing quark mass until it disappears at a critical endpoint. At non-zero baryon density, the effective theory can be evaluated either analytically by the so-called high-temperature expansion which does not suffer from the sign problem, or numerically by standard Monte-Carlo methods due to its mild sign problem. The first part of this work devotes to a systematic derivation of the effective theory up to the 6th order in the hopping parameter κ. This method combined with the SU(3) link update algorithm provides a way to simulate the $\mathcal{O}(\kappa^6)$ effective theory. The second part involves a study of the deconfinement transition of the pure gauge effective theory, with and without static quarks, at all chemical potentials with help of the high-temperature expansion. Our estimate of the deconfinement transition and its critical endpoint as a function of quark mass and all chemical potentials agrees well with recent Monte-Carlo simulations. In the third part, we investigate the $N_f \in \{1, 2\}$ effective theory with zero chemical potential up to $\mathcal{O}(\kappa^4)$. We determine the location of the critical hopping parameter at which the first-order deconfinement phase transition terminates and changes to a crossover. Our results for the critical endpoint of the $\mathcal{O}(\kappa^2)$ effective theory are in excellent agreement with the determinations from simulations of four-dimensional QCD with a hopping expanded determinant by the WHOT-QCD collaboration. For the $\mathcal{O}(\kappa^4)$ effective theory, our estimate suggests that the critical quark mass increases as the order of κ-contributions increases. We also compare with full lattice QCD with $N_f = 2$ degenerate standard Wilson fermions and thus obtain a measure for the validity of both the strong coupling and the hopping expansion in this regime.

[1]pham@itp.uni-frankfurt.de

Contents

The PhD thesis is based on the following publications:

1. *The Yang-Mills deconfinement transition from a high-temperature expansion*, PoS LATTICE 2019 [arXiv:1912.01705], with J. Kim, O. Philipsen, J. Scheunert.
2. *The SU(3) spin model with chemical potential by series expansion techniques.* JHEP (2020) [arXiv:2007.40187], with J. Kim, O. Philipsen, J. Scheunert.
3. *Deconfinement critical point of heavy quark effective lattice theories*, PoS LATTICE 2021 [arXiv:2112.06505], with J. Kim, O. Philipsen.

Deutsche Zusammenfassung

> The effort to understand the universe is one of the very few things which lifts human life a little above the level of farce and gives it some of the grace of tragedy.
>
> *Steven Weinberg*

Es ist allgemein anerkannt, dass Quantenchromodynamik (QCD) die richtige Theorie zur Beschreibung der starken Wechselwirkung zwischen Quarks und Gluonen ist. Diese Theorie ist ein wichtiger Bestandteil einer größeren Theorie namens Standardmodell (SM) der Teilchenphysik. Diese Theorie fasst die wesentlichen Erkenntnisse der Teilchenphysik nach aktuellem Stand zusammen und vereint drei der vier bekannten Grundkräfte im Universum: die elektromagnetische Wechselwirkung, die schwache Wechselwirkung und die starke Wechselwirkung, während die vergleichsweise sehr schwache Gravitation vernachlässigt wird. Die Elementarteilchen der QCD - Quarks und Gluonen unterscheiden sich deutlich von z.B. Elektronen und Photonen der Quantenelektrodynamik (QED). Es gibt keinen Zweifel, dass Quarks und Gluonen existieren, weil sie mit einem Großteil der erfolgreichen Phänomenologie der starken Wechselwirkungen konsistent zu sein scheinen, andererseits können sie jedoch in der Natur nicht direkt beobachtet werden. Dies deutet darauf hin, dass Quarks nicht als getrennte Teilchen in einem Endzustand erscheinen, sondern nur als Bestandteile von Hadronen wie dem Proton oder dem Neutron auftreten können. Ein wichtiger Effekt der QCD ist die sogenannte asymptotische Freiheit, die in den frühen Siebzigern von D. Politzer, F. Wilczek und D. Gross gefunden wurde (Nobelpreis 2004). Dies bedeutet, dass bei hohen Energien $E \sim 100\,\mathrm{GeV}$ oder kurzen Entfernungsskalen $r \sim 10^{-2}\,\mathrm{fm}$ die Stärke der Wechselwirkung, die durch eine Kopplungskonstante charakterisiert wird, im Wesentlichen verschwindet, d.h. Quarks können aus dem Confinement befreit werden. Andererseits scheint diese Kopplungskonstante unendlich groß zu werden, wenn die Entfernungsskala etwa eine Energieskala von $E \sim 100\,\mathrm{MeV}$ oder $r \sim 1\,\mathrm{fm}$ erreicht. Für sehr kleine Distanzen können wir Berechnungen im Rahmen von Methoden der Störungsentwicklung durchführen. Bei großen Distanzen wird die Theorie wegen der unkontrollierbaren Feynman-Diagramme allerdings sehr anspruchsvoll. Der Unterschied zwischen Regionen, in denen die Berechnungen kontrollierbar und in denen sie anspruchsvoll sind, wird in Bezug auf eine Energieskala, die als QCD-Skala $\Lambda_{\mathrm{QCD}} \sim 200\,\mathrm{MeV}$ bekannt ist, charakterisiert. Für die anspruchsvollen Regionen ist es erforderlich, die Dynamik von Quarks mit einem nicht-perturbativen Ansatz zu untersuchen.

In der zweiten Hälfte des 20. Jahrhunderts wurde die Gittereichtheorie nach diesem Bedarf konstruiert, die auf mathematischen Konzepten basiert und die Untersuchung der nichtperturbativen Phänomene durch numerische Simulationen ermöglicht. Obwohl die numerische Gitter-QCD im Laufe der Jahre viele wichtige Innovationen erfahren hat, befindet sie sich auf-

grund einiger großer Herausforderungen bei den Berechnungen derzeit noch in gewissem Maße in einer Entwicklungsphase. Die Grundidee dieses Ansatzes besteht darin, die vierdimensionale Raumzeit in ein vierdimensionales Gitter zu diskretisieren und die Felder der QCD Lagrange-Funktion auf die Punkte dieses Gitters zu beschränken. Diese Theorie ist der einzige nicht-perturbative, systematisch einstellbare Ansatz für QCD, und im Grunde genommen, durch die Gittereichtheorie können Informationen über Quarks und Gluonen ausschließlich unter Verwendung von ersten Prinzipien - die Lagrange-Funktion der QCD - extrahiert werden. Außerdem, die Schwierigkeiten der unendlichen Freiheitsgrade von der Quantenfeldtheorie werden durch die Gitterfeldtheorie vereinfacht, weil die Quantenfeldtheorie durch eine andere Theorie ersetzt wird, die eine endliche, wenn auch sehr große Zahl von Freiheitsgraden hat. Trotz der Vereinfachung hat das Zustandsintegral immer noch eine sehr große Dimension, was übliche numerische Integrationstechniken ausschließt. Solche Integrale können normalerweise nur mit stochastische Monte-Carlo (MC)-Methoden, die auf Stichprobenentnahme nach Wichtigkeit und den Eigenschaften der Ergodizität basieren, berechnet werden.

Da wir nun eine etablierte Theorie der starken Wechselwirkung besitzen, ist es naheliegend, die Eigenschaften hadronischer Materie in ungewöhnlichen Umgebungen zu erforschen, insbesondere bei endlichen Temperaturen oder endlichen Baryonendichten. Die Erforschung dieses Bereichs ist von großer Bedeutung, da für das Verständnis einiger Phänomene die Kenntnis über die Zustandsgleichung und die Natur der Phasen hadronischer Materie essentiell ist. Zum Beispiel: das Innere von Neutronensternen, wo die Dichte deutlich größer ist als die nukleare Dichte; die Kollisionen schwerer Ionen mit sehr hoher Energie pro Nukleon, bei denen sich ein Materieklumpen wie ein thermalisiertes System verhält, gekennzeichnet durch eine Temperatur und ein chemisches Potential. Dieses System wird verwendet, um eine Trajektorie auf dem Phasendiagramm zu verfolgen. Solche Kollisionen werden derzeit im Large Hadron Collider (LHC) am CERN, im Relativistic Heavy Ion Collider (RHIC) des Brookhaven National Laboratory oder bei der Facility for Antiproton and Ion Research (FAIR) in Darmstadt durchgeführt; oder die Zustände des frühen Universums, als seine Temperatur viel höher war als die QCD-Skala Λ_{QCD}.

Ein wichtiger Aspekt der Erforschung der Phasenübergänge sind kritische Punkte, die Endpunkte der Linie erster Ordnung, an denen die Grenze zwischen Phasen verschwindet. Sie spielen eine zentrale Rolle bei der Untersuchung von Phasenübergängen in der Materie, beginnend mit der Beobachtung des kritischen Punktes im Wasser im 19. Jahrhundert. Eine wichtige Frage im Zusammenhang mit der Erforschung stark-wechselwirkender Materie ist, ob im Phasendiagramm ein kritischer Punkt existiert. Das Phasendiagramm der QCD ist durch die Temperatur T und das chemische Potential μ charakterisiert. Das chemische Potential bezieht sich direkt auf die Nettoquarkdichte, die als die Differenz der Dichte von Quarks und Antiquarks definiert ist. Leider leiden bei endlicher Dichte $\mu/T > 1$ alle Monte-Carlo Algorithmen unter dem sogenannten Fermion-Vorzeichenproblem, das auftaucht, wenn man baryonchemisches Potential in die Gitter-QCD einführt. Die Fermion-Determinante wird dann komplex und kann nicht mehr als die Verteilung der Feldkonfigurationen verwendet werden. Es existiert eine Reihe verschiedener Ansätze wie die Reweighting-Technik, die komplexe Langevin-Methode, die Taylor-Expansion-Methode oder die Methode des rein imaginären chemischen Potentials um indirekt Einblicke auf das tatsächliche QCD Phasendiagramm zu gewinnen. Diese Ansätze basieren normalerweise auf Techniken der analytischen Fortsetzung. Es gibt bisher jedoch keine zuverlässigen Informationen über die QCD-Phasenstruktur bei hohen Dichten und niedrigen Temperaturen. In dieser Arbeit untersuchen wir die QCD der schweren Quarks bei endlicher Dichte und endlicher Temperatur mithilfe der Gittereichtheorie der Wilson-Fermionen

durch eine effektive dreidimensionale Gittertheorie, die nur von den Polyakov-Loops abhängt.

Das zentrale Thema dieser Arbeit ist die effektive Gittertheorie von Polyakov-Loops. Diese Theorie erlaubt es, das Phasendiagramm der QCD mit schweren Quarks in vollem Parameterraum (m_q, T, μ) zu untersuchen. Sie ist erhalten, indem alle räumliche Linkvariablen aus der Zustandssumme heraus integriert werden. Dadurch wird der Beitrag zum Fermion-Vorzeichenproblem in der effektiven Theorie stark reduziert. Des Weiteren basiert die Herleitung der effektive Gittertheorie auf einer Kombination aus Starkkopplungsentwicklung und Hopping-Parameter-Entwicklung um schwere Quarkmassen. Das milde Vorzeichenproblem der effektiven Gittertheorie ermöglicht mehrere Ansätze, z.B. die direkte Monte-Carlo Simulation mit der Reweighting-Technik, die komplexe Langevin-Methode oder die Reihenentwicklungsmethoden, die verwendet werden können, um die Theorie bei endlicher Dichte auszuwerten. Die Entwicklungen wurden in vorherigen Arbeiten angewendet und wir fassen die notwendigen mathematischen Grundlagen zu den Entwicklungen zusammen. Schließlich präsentieren wir eine frühe Arbeit zur systematischen Ableitung der effektiven Gittertheorie durch die Ordnung $\mathcal{O}(\kappa^6)$ im Hopping-Expansion-Parameter, die auf einer Graphendarstellung basiert. Durch diese Methode werden komplizierte Ausdrücke von räumlichen Sprüngen und zeitlichen Propagatoren in der kinetischen Determinante in Form von Graphen dargestellt, welche dann auf einem Computer erzeugt werden können. Diese Graphendarstellungen können bei Bedarf leicht in die analytischen Ausdrücke zurückkonvertiert werden. Mit Hilfe von Computern kann diese Methode genutzt werden, um die effektive Theorie um höhere Ordnungen zu erweitern.

Zur Simulation der SU(3) effektiven Gittertheorie gibt es eine Standardparametrisierung des Polyakov-Loops, bei der eine SU(3)-Matrix unter der Wirkung der Spur zu einer diagonalen Form transformiert werden kann. Der Vorteil dieser Parametrisierung besteht darin, dass die Freiheitsgrade für die Durchführung von Monte-Carlo-Methoden reduziert werden, jedoch zu ihrer Verwendung muss das Integrationsmaß zunächst transformiert werden. Diese Transformation führt ein zusätzliches effektives Potenzial ein. Außerdem, der Ansatz leidet an einem kombinatorischen Problem, das auftritt, wenn Terme der kinetischen Determinante in Polyakov-Loops neu ausgedrückt werden. Diese große Anzahl von Termen verlangsamt erheblich den Simulationsprozess bereits bei der $\mathcal{O}(\kappa^4)$ effektiven Gittertheorie. In dieser Arbeit wird eine alternative Parametrisierung des Polyakov-Loops eingeführt, bei der die Technik des SU(3) Linkvariable-Updates verwendet wird. Diese neue Parametrisierung wird dieselben Ergebnisse wie die Standardparametrierung reproduzieren und dazu dienen, Ausdrücke der effektiven Theorie nicht zu groß zu halten. Dies wiederum wird die Effizienz der Simulationen erhöhen und kann die Simulationen der $\mathcal{O}(\kappa^6)$ effektiven Gittertheorie ermöglichen, wo es deutlich mehr Terme als die $\mathcal{O}(\kappa^4)$ effektive Gittertheorie gibt.

In dieser Arbeit konzentrieren wir uns auf die Untersuchung der deconfinement Phasenübergänge und ihres kritischen Endpunkts im Rahmen von der effektiven Gittertheorie. Die Bewertung umfasst zwei Teile: analytische Berechnungen und numerische Simulationen. Wir verwenden den analytischen Ansatz basierend auf Reihenentwicklungsmethoden für die effektive Theorie von reinen Eichfeldern und statischen Quarks bei allen chemischen Baryonenpotentialen. Obwohl diese Theorie nur eine Approximation der Gitter-QCD, enthält sie bereits wichtige Eigenschaften der QCD. Dazu gehören die Z_3-Zentrumssymmetrie des reinen Eichsektors, die Symmetriebrechung durch Quarks mit endlichen Massen, sowie die Roberge-Weiss-Symmetrie für komplexes chemisches Potential. Es gibt mehrere Reihenexpansionsmethoden wie zum Beispiel die Linked-Cluster-Expansion, die Hochtemperaturexpansion oder die molekulare Feldexpansion. Aufgrund der Natur der logarithmischen Wirkung der

effektiven Gittertheorie ist jedoch die Hochtemperaturexpansion das einzig geeignete Schema. Diese Reihenentwicklungsmethode basiert hauptsächlich auf den Techniken der Graphentheorie. Die Hochtemperaturexpansion kann als Summe von Termen geschrieben werden, wobei jeder Term durch einen Graphen in der Ebene dargestellt wird, der aus Knoten (vertices) und Kanten (bonds) besteht. Auch hier wird die Berechnung der Zustandssumme oder der Suszeptibilität des Polyakov-Loops von Hand nach einigen führenden Ordnungen mühsam, dann treten die kombinatorischen Probleme auf. Glücklicherweise lassen sich mit Hilfe von Computern und dem sogenannten 'Pegs in Holes' (PIH) Algorithmus Graphengenerierungen und Graphenzählungen systematisch archivieren.

Wir haben die effektive Zustandssumme $Z_{\text{eff}}(\lambda_1, h_1, \bar{h}_1)$ und die Suszeptibilität der Polyakov-Loop $\chi_L(\lambda_1, h_1, \bar{h}_1)$ zur 13. Ordnung in der effektiven Nächsten-Nachbar-Eichkopplung λ_1 sowie in den Kopplungen h_1 und $\bar{h}_1$ berechnet. Daraus lässt sich leicht die Zustandsgleichung durch die logarithmische Funktion der effektiven Zustandssumme berechnen, jedoch interessieren wir uns eher die kritischen Punkte der Theorie, deshalb werden wir uns auf die Auswertung der Suszeptibilität χ_L konzentrieren, um Informationen über die Kritikalität unseres Systems zu extrahieren. Für Systeme mit einer Variablen bzw. einer Kopplung, wie die effektive reine Eichtheorie, funktioniert der Padé-Approximant sehr gut, andererseits für multivariate Systeme wie die effektive reine Eichtheorie mit statischen Quarks, kann der Padé-Approximant jedoch immer noch die Phasengrenze anzeigen, nicht den kritischen Endpunkt. Aus diesem Grund müssen wir den Padé-Approximant mit einer anderen Methode namens Canterbury-Approximant - eine natürliche Generalisierung vom Padé-Approximant für multivariate Serien - kombinieren. Dies sind zwei verschiedene Methoden, aber sie funktionieren am besten für die Endpunkte zweiter Ordnung, daher können wir aus den Schnittpunkten ihrer Approximanten den kritischen Endpunkt schätzen. Unsere analytische Ergebnisse bei allen chemischen Baryonenpotentialen stimmen mit denen aus Simulationen überein, wo das Fermion-Vorzeichenproblem durch die Flux-Darstellung der Zustandssumme gelöst wurde. Dies beweist auch die Konsistenz unseres analytischen Ansatzes.

Trotz konsistenter Ergebnisse der Hochtemperaturexpansion für die effektive reine Eichtheorie mit den statischen Quarks ist es schwierig, die Reihenentwicklungsmethode auf die effektive Gittertheorie bei höheren Ordnungen als $\mathcal{O}(\kappa^2)$ in der Hopping-Parameter anzuwenden. Aus diesem Grund ist die Monte-Carlo-Methode besser geeignet, es sei denn, es gibt eine Möglichkeit, alle Ordnungen des Hopping-Parameters ähnlich der Charakter-Expansion für die reine Eichtheorie zu reorganisieren. Ein prominenter Ansatz dafür wäre die Verwendung der Finite-Cluster-Methode in einer numerischen Bestimmung der effektiven Kopplungen der effektiven Theorie. In dieser Arbeit wenden wir die Monte-Carlo-Methode auf die $N_f \in \{1, 2\}$ effektive Theorie ohne chemisches Potential bis zu $\mathcal{O}(\kappa^4)$ im Hopping-Parameter bei $N_t \in \{4, 6\}$ an, um die deconfinement Phasenübergänge zu untersuchen, sowie die kritische Quarkmasse zu bestimmen.

Wir haben den Metropolis-Algorithmus in Verbindung mit dem Verfahren des Linkvariable-Updates auf die effektive Gittertheorie angewendet, da ihre Wirkung nur eine Funktion von SU(3)-Linkvariablen ist. Wir vergleichen unsere Ergebnisse ebenfalls mit vollständigen QCD-Simulationen und beobachten, dass die Phasenstruktur der vierdimensionalen QCD durch die effektive Gittertheorie auf einer halbquantitativen Ebene reproduziert wird, so dass ihre Anwendung dem kalten und dichten Regime vertraut werden kann. Hinsichtlich der quantitativen Genauigkeit erlaubt der Vergleich entweder mit Hopping-Expansion oder voller QCD detaillierte und getrennte Rückschlüsse auf die Starkkopplungsentwicklung und die Hopping-Parameter-Entwicklung: Die dreidimensionale effektive Gittertheorie stimmt fast quantitativ

überein mit der vierdimensionalen QCD mit einer erweiterten Hopping-Determinante, während beide mit voller QCD größere Unterschiede aufweisen wenn N_t wächst. Das bedeutet, dass die Charakter-Expansion ein gutes Konvergenzverhalten zeigt und für thermodynamische Anwendungen bis $N_t = 6$ ausreichend ist, während Korrekturen höherer Ordnung in der Hopping-Expansion bereits bei $N_t = 6$ erforderlich sind.

Abschließend geben wir eine Fazit unserer Ergebnisse, einen Ausblick auf mögliche Projekte, die auf den Resultaten der Dissertation aufbauen und diese erweitern könnten. Hierbei sei insbesondere auf die Möglichkeit hingewiesen, die Graphendarstellung für die Herleitung der effektiven Polyakov-Loop-Theorie von höheren Ordnungen in einer Kombination mit dem Linkvariable-Update zu verwenden. Wir verlagern einige technische Details unserer Berechnungen in dieser Dissertation in die Appendizes.

Acknowledgements

First of all, I would like to thank my supervisor Owe Philipsen for his help and support during my time in Frankfurt. The research projects suggested by him were not only challenging but also within my ability to obtain interesting results, in particular for someone like me who was unfamiliar with concepts of lattice gauge theory at the beginning. I have benefited a lot from his passion and enthusiasm for physics. His knowledge and intuition in physics helped guide me to stay on the right track. I also would like to thank Dirk Rischke for being my second supervisor, and for the fruitful conversations during the Ph.D. committee meetings.

I would like to say many thanks to Jangho Kim with whom I can collaborate very well. He was always there for me whenever I wanted to discuss physics. His knowledge in numerical studies and his programming skills had inspired and helped me a lot throughout my Ph.D. I also would thank Jonas Scheunert, with whom we worked together in various projects presented in this work.

I am indebted to Bastian Brandt, Gergely Endrődi, and Francesca Cuteri for teaching me lattice gauge theory, without this course the numerical results of this work might not be possible. I also owe many thanks to Alessandro Sciarra who taught me a lot about programming, and whom I could always turn in for technical questions.

I would like to thank Sebastian Schmalzbauer for his helps, Miguel Salg, and Alena Zmarsly for useful discussions. I am grateful to Christopher Winterowd, Alena Zmarsly, Bastian Brandt, Jangho Kim, Francesca Cuteri, and Alessandro Sciarra who helped proofread this thesis. Although I do not know Jonas Glesaaen personally, I would like to thank him for the source code of many figures in this work. I would like to extend a thank to the entire working group, who has made my stay here a pleasant one.

My research was carried out at the Institute for Theoretical Physics at the Goethe University Frankfurt. My work was supported by the HGS-HIRe in form of a scholarship. Computations were performed on the Goethe-HLR cluster.

Next, I am especially thankful to my parents who dedicated their life to my education and have always encouraged me to pursue physics, although they never went to college. Finally, I am deeply indebted to my wife Thao for her constant support and encouragement, she has done an excellent job taking care of our daughter so that I could focus on my work.

Chapter 1

Introduction

> We are driven to the conclusion that the Hamiltonian method for strong interaction is dead and must be buried, although of course with deserved honor.
>
> *From a memorial volume to Wolfgang Pauli by Lev Landau*

Particle physics plays a remarkable role in our understanding of the laws of nature. It is concerned with the constituents of the universe at fundamental levels such as how the elementary particles form bound states and how they interact with each other. The Standard Model of particle physics covers a big part of our current understanding, it serves as a unified picture of the strong, weak, and electromagnetic interactions. The strong interaction influences nuclear binding and the interactions of the constituents of nuclei, the weak force is responsible for the nuclear β-decays of certain radioactive isotopes, and the electromagnetic interaction, which is described by the well-known quantum electrodynamics (QED), coupled weakly to all charged quarks and leptons. Amazingly, the Standard Model stands today under precision tests in numerous colliding experiments including, for instance, those at the Large Hadron Collider at CERN and in the Fermi National Accelerator Laboratory in the USA.

By now there is no doubt that the theory of hadronic physics is the SU(3) gauge theory of quarks and gluons called quantum chromodynamics (QCD). This theory describes a wide range of phenomena, including the notion of confinement of color, dynamical mass generation, and chiral symmetry breaking. Although we have the correct theory for the strong interaction, which was proposed independently a long time ago by Gell-Mann and Zweig in 1963 [1, 2], there are many features of the theory that are still poorly understood, in particular from aspects of quantitative calculations. For example, it is very challenging to obtain a reliable computation for the baryon spectrum, because the signal-to-noise ratio of the associated two-point functions decreases exponentially at large distance [3], or the study of strongly interacting matter under extreme conditions in particular at finite chemical potential where standard Monte-Carlo methods suffer from the fermion sign problem. The study of QCD under extreme conditions is relevant to several experimental windows, for example, the physics of the early universe, heavy-ion collisions, or compact star interiors.

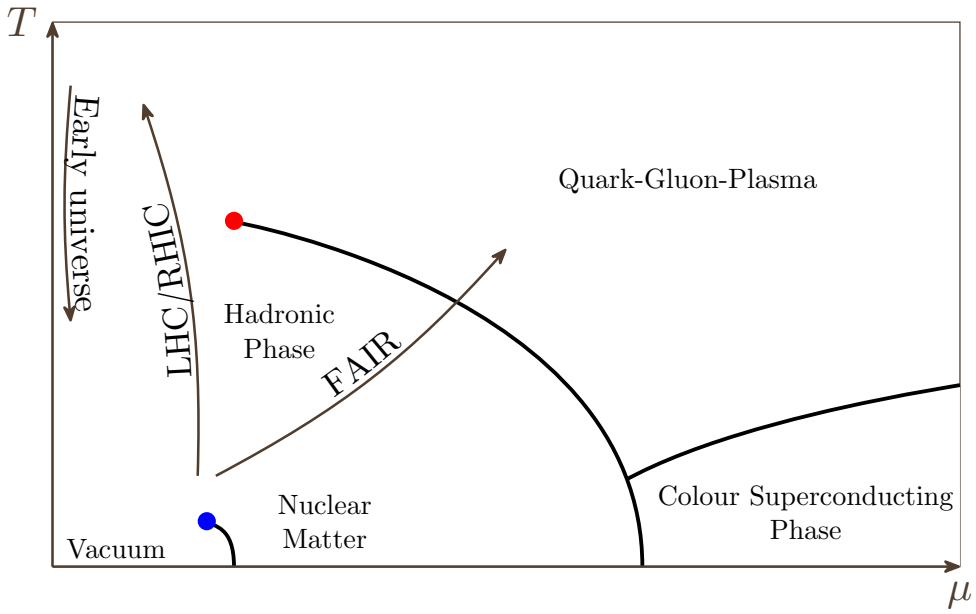

Figure 1.1: A schematic, conjectured QCD phase diagram as a function of chemical potential μ and temperature T.

1.1 The phase diagram of QCD

A very common critical phenomenon in condensed matter physics is the endpoint of a first-order line is a critical point of the second-order where the boundary between phases disappears. For example, water possesses a critical point, when the line of the water boiling transition terminates at temperature $T_c = 374^\circ C$ and pressure $p_c = 218$ atm. At present, due to its unique properties, finding critical points and studying phase transitions of QCD at finite temperature and density becomes one of the major challenges of modern physics.

The phase diagram of QCD is characterized by the temperature T and the chemical potential μ, see fig. 1.1. The chemical potential is associated directly with the net density of quarks[1]. At a fixed temperature the net quark density becomes larger when the chemical potential increases. Consider the case of the early universe, when the number of quarks and antiquarks were roughly the same, so $\mu = 0$, it was at the state of a very high temperature. This temperature was much higher than the QCD scale ($\Lambda_{\mathrm{QCD}} \sim 200$ MeV). Asymptotic freedom indicates that quarks interact weakly with each other when approaching such high energy scales. In other words, at such high temperatures of the Early universe quarks are free from confinement, they together with gluons form a new state of matter called plasma state or quark-gluon plasma (QGP). For further discussions of the quark-gluon plasma, see [4, 5].

Confinement is restored, i.e. there exists a transition from QGP to hadronic matter, as the universe's temperature decreases to about the confinement scale ~ 1 fm, where the interaction becomes strong. According to lattice QCD calculations, this transition is likely to be an analytic crossover [6], which implies that the confinement transition from low- to high-temperature phases of QCD need not proceed through a singularity. Similar transitions occur in later states in the evolution of the universe, like the electroweak transition associated with the spontaneous breaking of the electroweak symmetry in the Standard Model [7,8] or the transition of electrons

[1]The difference of the density of quarks by the density of antiquarks.

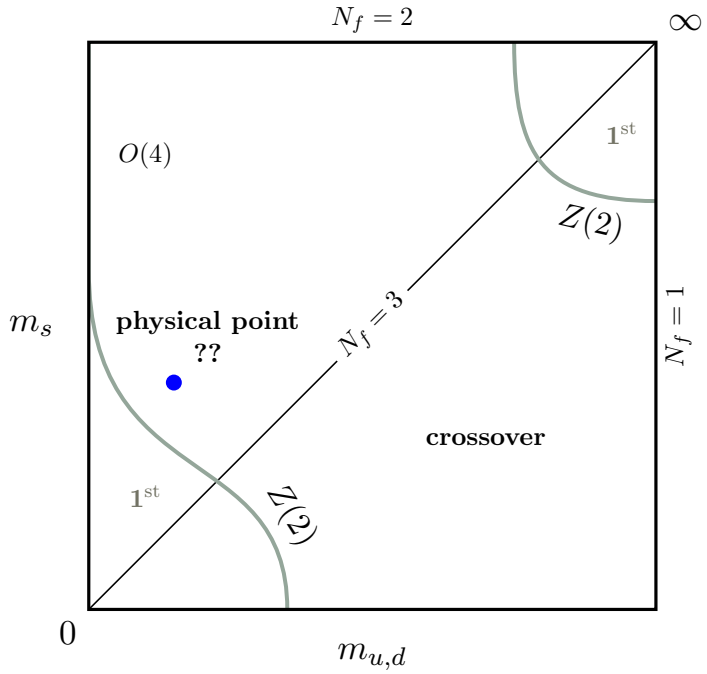

Figure 1.2: The Columbia plot: showing the order of the QCD phase transition as function of quark masses $(m_{u,d}, m_s)$ at zero chemical potential.

and protons into hydrogen in the recombination era [9].

By compressing hadronic matter, i.e. along the line, where the temperature is kept fixed at $T = 0$ and the quark chemical potential increases[2], there is a jump from vacuum to nuclear matter - the matter that is responsible for forming atomic nuclei. There is very little reliable information about the value of μ at which this phase transition occurs, but one can determine that this transition is of first-order [10, 11]. At higher temperatures, this first-order phase transition will continue and terminate when a critical endpoint is reached. We know far less about what happens at higher densities and small temperatures, but it was predicted in [12] that the QCD phase diagram processes a color-flavor-locking (CFL) or color superconductivity phase in this regime. This region is also of particular theoretical interest because thanks to asymptotic freedom and new insights from the theory of superconductivity analytical controllable calculations are possible. The recent developments for this regime of the phase diagram can be found in [4, 12, 13].

The temperatures and densities, which are relevant for QCD, can only be probed by relativistic heavy-ion collisions experiments. For small densities, the heavy-ion collisions experiments are performed at the Large Hadron Collider (LHC) or the Relativistic Heavy Ion Collider (RHIC), while the Facility for Antiproton and Ion Research (FAIR) currently runs experiments aiming for larger densities. The region of the QCD phase diagram, which can be archived through such experiments, is the temperature roughly of the QCD scale $T \sim 100$ MeV, and a small to medium chemical potential $\mu \sim 0 - 600$ MeV [14]. In order to build next generation experiments, it is crucial to have a better understanding of the QCD phase diagram.

[2]At low temperature, it is believed that a very rich spectrum of possibilities of ordering exists.

The qualitative picture for the order of the three-flavor QCD phase transition at zero baryon density as a function of the quark masses is shown in fig. 1.2. Due to its rich structures and the gradual improvements in the field, it is useful to give a short overview of the so-called Columbia plot. Starting with the lower-left and upper-right corners, moving along the $N_f = 3$ line, when the three quarks are massless or infinite, one can define order parameters associated with the symmetry breaking, i.e. there will be true phase transitions. Backed by lattice computations, these transitions are first-order. At intermediate quark masses, an analytic crossover appears, implying that there must be a second-order line that bounds the region of first-order transition at each corner. The lower-left corner is called *chiral region*, and the upper-right corner is called the *deconfinement region* according to the chiral transitions and the deconfinement transitions, respectively. From [15,16], the line bounding the chiral region is located to the left of the physical point. In the case of two light quarks, in the upper-left-hand side of the Columbia plot, the transition is of second-order and in the universality class of three-dimensional $O(4)$ spin models. Currently, there is no evidence for this universality but one can expect a confirmation in the near future. If the transition is indeed second-order, then there must be a tricritical strange quark mass m_s^{tric}, which separates the region of first-order transitions from the line of second-order transitions. A detailed overview of the Columbia plot can be found in [17,18].

At present, despite a lot of effort that has been invested in studying the phase diagram of strongly interacting matter under extreme conditions, the QCD phase diagram at finite quark chemical potential remains unknown, because all Monte-Carlo methods suffer from the fermion sign problem. This problem can be partially controlled if the chemical potential is not too large $\mu = \mu_B/3 \simeq T$ [19,20], where it is unlikely that the critical point would locate within this region [15]. Some attempts have been considered, for example: the complex Langevin simulations which are based on stochastic quantization methods, and do not suffer a sign problem, but for complex actions the correct results are not guaranteed [21,22]; the reweighting technique which faces the overlap problem for $\mu/T > 1$ [15]; or Taylor expansion [23–25] or simulations at imaginary chemical potential [26] followed by analytic continuation all give additional systematic errors and require $\mu/T < 1$ to be valid.

This motivates the development of alternative formulations and algorithms to remedy this problem. The formulation of effective theories, which are derived directly from first principles by integrating out some degrees of freedom, shows great potential in dealing with the fermion sign problem, at least in the regime of heavy quarks [27–29]. On one hand, with part of the degrees of freedom integrated out, the sign problem of the effective theory becomes milder. Thus, it is possible to simulate with standard Monte-Carlo methods or complex Langevin algorithms. On the other hand, one can use series expansion methods to carry out analytic computations [30–32], for which the sign problem is irrelevant. Although the Polyakov loop effective theory is just an approximation of lattice QCD, it exhibits similar behavior to QCD, for example in the SU(3) pure gauge theory, the deconfinement transition spontaneously breaks the global Z_3 center symmetry, and is of first-order. The presence of dynamical quarks breaks the center symmetry explicitly and leads to a weakening of the deconfinement transition with decreasing quark mass until it vanishes at a critical point in the three-dimensional Ising universality class. For still lighter quark masses, the transition becomes an analytic crossover. Furthermore, at large the N_c limit the existence of quarkyonic matter is supported by calculations from effective theories [33].

Because of the complexity of phenomena which QCD or the effective theory describes, we cannot even dream of solving them exactly. In the absence of exact solutions, there is a set

of quantitative approaches which can be used such as series expansion methods, Monte-Carlo simulations, or renormalization methods. Each of these has its strengths and weaknesses for different problems. In this work, we will employ the series expansion method and the Monte-Carlo method for different regimes of the effective theory. Of course, the series expansion techniques are not new and have long been used in statistical mechanics, and more recently, also in quantum field theory [34], for reviews of series expansion methods see [35, 36]. These techniques are usually based on graph representations, and proved to be highly systematic and mechanical since graphs can be generated and evaluated fully by computer.

This work aims at exploring lattice QCD of heavy quarks at zero and finite chemical potential by means of using effective lattice theories. We have tested the consistency of our methodology by applying a series expansion method called the linked cluster expansion to the SU(3) spin model at finite chemical potential [31]. In this work, we investigate an improved effective theory, which contains the SU(3) pure gauge effective theory and the static quark determinant. This effective theory has better convergence and possesses features closer to QCD in comparison with the SU(3) spin model. It is necessary to point out that the linked cluster expansion is not suitable for the improved effective theory due to the logarithmic function in the action. Thus, we will apply a different expansion scheme called high-temperature expansion instead[3], whose generated graphs are different from those generated by the linked cluster expansion.

The standard Monte-Carlo methods - the most important numerical methods used for solving statistical physics problems - are also applied to the effective theory with zero chemical potential at higher orders of the hopping parameter κ. For the SU(3) effective theory, there exists a standard parametrization of the Polyakov loop, by which we write the trace of a SU(3) matrix by rotating it to its diagonal form. The advantage of this parametrization is that the degrees of freedom for performing Monte-Carlo methods are reduced, however, to use it one first needs to transform the integration measure which introduces an additional effective potential, and then re-express the effective action fully in terms of Polyakov loops, which will make the expression of the effective theory very large at higher κ-corrections[4]. In this thesis, an alternative parametrization of the Polyakov loop is introduced, as we will see, this new parametrization will reproduce the same results as the standard one, and will serve to keep expressions of the effective theory not too large. This in turn will increase the efficiency of the simulations.

1.2 Outline

The contents of this thesis are as follows. We begin with a brief review of the general concepts in chapter 2, including the definition of QCD action in the continuum, and how QCD can be formulated via the lattice discretization approach. As a preparation for the next chapter, we show how temperature and chemical potential are defined on the lattice. Center symmetry, which plays an important role for confinement, is discussed. In section 2.5 the thermodynamic properties of quantum field theory and lattice gauge theory are discussed in more details. The challenges that arise at large chemical potential from the aspect of lattice simulation, will be

[3]The name 'high-temperature expansion' is taken from statistical mechanics literature, where the expansion parameter is defined as the inverse of temperature, i.e. at high temperature the parameter is supposed to be sufficiently small for performing series expansion. Here in the context of the effective theory, the effective couplings play a role as an expansion parameter.

[4]The coupling κ is related directly to the quark mass m_q.

described.

After having discussed some of the basic elements of lattice QCD, we turn to present the detailed derivation of the effective theory in chapter 3. Three main expansion schemes; strong coupling expansion, character expansion, and hopping expansion, are introduced. We then present a graph representation method for deriving the effective theory at $\mathcal{O}(\kappa^6)$, which can be generalized to the effective theory at higher orders in κ, where graphs of the kinetic quark determinant will be generated and evaluated by computer. This method combined with the link-variable update provides a way to simulate the effective theory at higher orders, i.e. it can be used to deal with combinatorial problems that appear when converting all terms of the action into a function of Polyakov loops.

The next topic concerns an expansion scheme called the high-temperature expansion. We start the discussion by recalling the basic notions of graph theory relevant for the high-temperature expansion. Similar to Feynman diagrams, the high-temperature expansion can be written as a sum of terms, where each term is represented by a graph in the plane consisting of vertices and edges joining them. In this way, complicated expressions from the partition function or some observable are converted to the form of simple graphs. For the lattice effective theory of QCD with heavy quarks, where we obtain a log-action after the resummation of higher-order terms, the high-temperature expansion is the only suitable expansion scheme, because it reproduces the correct leading-order results of the effective theory. We also discuss two series analysis methods: Padé and Canterbury approximant, which are used to extract information about the criticality of asymptotic series.

Chapter 5 is devoted to general concepts of the Monte-Carlo method, where it is explained how Markov chains and the concept of importance sampling can simulate the effective theory. In particular, the Metropolis algorithm for SU(3) link variables is discussed in some detail. The estimation of the statistical errors in numerical lattice QCD is discussed. A resampling technique called the jackknife method, which allows the errors of the calculated observables to be estimated, is described.

Finally, in chapter 6 we discuss our results from analytic and numerical calculations. Our results obtained from the high-temperature expansion are presented along with a discussion of the checks and comparisons with numerical simulations. The validity of our method is shown by a good agreement with simulation results. This method is not affected by the fermion sign problem and is applied to determine the phase transition and its critical endpoint of the effective theory that contains pure gauge action and static quarks. It is important to point out that it is impossible to publish all expansions coefficients on paper since there are several thousands of them. We therefore only print some special cases and make the full listing available somewhere else. Furthermore, we apply the Monte-Carlo method to the $N_f \in \{1, 2\}$ effective theory with zero chemical potential up to $\mathcal{O}(\kappa^4)$ to determine the critical hopping parameter, at which the first-order deconfinement phase transition terminates. The critical endpoint obtained from the effective theory to order $\mathcal{O}(\kappa^2)$ is in excellent agreement with those by the WHOT-QCD collaboration, where the endpoint is determined by studying the quenched QCD simulations combined with the hopping-expanded determinant for $N_f \in \{1, 2, 3\}$ on $N_t \in \{4, 6, 8\}$. We also compare with full QCD simulations with the temporal extent $N_t = 6$ for $N_f = 2$ and thus obtain a measure for the validity of both the strong coupling and the hopping expansion in this regime. We relegate some technical details of our calculations throughout this thesis to appendices.

Chapter 2

Lattice gauge theory

> ... the difficulty is only that the exact application of these laws leads to equations much too complicated to be soluble.
>
> *by P.A.M. Dirac*

2.1 QCD and strong interactions

Without doubt, the strong interactions can be described by QCD. It is one of the biggest triumphs of the quantum field theory. The breakthrough which provided much of the support for QCD, was the discovery of the property of *asymptotic freedom* of non-Abelian gauge theory [37–39]. This feature of the theory offers an explanation of Bjorken scaling which has been observed in the deep inelastic scattering of leptons off hadrons and can be used to make many quantitative predictions of scaling deviations at high energy [40, 41]. In addition, according to the crucial property of asymptotic freedom that the effective coupling constant tends to be small for large momentum scale, many predictions of perturbative QCD at short distances were confirmed, e.g., quark and gluon jets or charm-anticharm bound states as a narrow resonance in e^+e^- annihilation [42, 43]. The success of these predictions and many more recent quantitative results from lattice calculations have greatly increased our confidence in the theory.

QCD is a renormalizable, non-Abelian quantum field theory describing the strong interactions. It was shown that among the known class of four-dimensional quantum field theories only the non-Abelian gauge theory exhibited the property of asymptotic freedom [39]. The fundamental building blocks of QCD are spin 1/2 fermions called quarks which carry a fractional electric charge and non-Abelian spin 1 gauge fields called gluons. On one hand, similar to QED gluons play a role as a mediating particle that transmits the interaction between color-charged quarks, on the other hand, gluons also have an additional property that they can interact among themselves due to self-interaction terms in the QCD Lagrangian, and thus possess a color quantum number.

To begin our description of this theory, we introduce the fermion and antifermion fields ψ and $\bar{\psi}$ known as "quarks" and "antiquarks". These fields are Dirac spinor fields that transform in the fundamental representation of the gauge (color) group SU(3). The main idea of QCD is to make the SU(3) symmetry a local symmetry[1], and to explore this local symmetry one must

[1]Note that QCD also has a global symmetry which gives us $N_c^2 - 1$ conserved currents, but in contrast to QED these currents and the corresponding charges are not physical because they are not gauge invariant. In

take into account the gauge field A_μ. Analogous to QED, the dynamics of the gauge field is governed by the field strength tensor $F_{\mu\nu}$ which is defined as a commutator of two covariant derivatives

$$F_{\mu\nu} = -i[D_\mu, D_\nu] = \partial_\mu A_\nu - \partial_\nu A_\mu + i[A_\mu, A_\nu], \tag{2.1}$$

where the covariant derivative[2] is $D_\mu = \partial_\mu + iA_\mu$. To avoid a complex probability distribution in numerical studies, we use the Euclidean path integral as the standard tool for quantizing fields and performing calculations on the lattice. Finally, in Euclidean space[3] the Lagrangian density of QCD for N_f number of quark flavors is

$$\mathscr{L} = \frac{1}{2g^2}\,\mathrm{tr}\,(F_{\mu\nu}F^{\mu\nu}) + \sum_{f=1}^{N_f} \bar{\psi}_f(\gamma^\mu D_\mu + m_f)\psi_f. \tag{2.2}$$

Here we can regard the gauge field A_μ as a matrix and expand over a basis of the Lie algebra $\mathfrak{su}(3)$. In contrast to the Standard Model where we cannot explain the various coupling constants, the parameters that characterize QCD are the gauge coupling g and six quark masses m_f corresponding to six flavors of quarks; up, down, strange, charm, top and bottom. However, in many calculations, one can neglect the contributions of heavy quarks at the non-perturbative scale of $T_c \sim 200$ MeV and include only the lightest two to four flavors of quarks [44].

It is simple to show that the QCD action is invariant under SU(3) transformations, where the quark fields ψ transforms in the fundamental representation and the gauge field A_μ transforms in the adjoint representation of the gauge group SU(3) respectively as

$$\psi(n) \to \psi'(n) = \Omega(n)\psi(n), \quad \bar{\psi}(n) \to \bar{\psi}'(n) = \bar{\psi}(n)\Omega^\dagger(n), \tag{2.3}$$

$$A_\mu(n) \to A'(n) = \Omega(n)A_\mu(n)\Omega^\dagger(n) + i\partial_\mu\Omega(n)\Omega^\dagger(n). \tag{2.4}$$

Here Ω is an arbitrary element of the SU(3) group, i.e. it fulfills unitary $\Omega^\dagger = \Omega^{-1}$ and $\det[\Omega] = 1$ at each space-time position n. We notice that with A_μ transforming as in (2.4), the transformation property for the covariant derivative and the field strength tensor are

$$D_\mu(n) \to D'_\mu(n) = \partial_\mu + iA'_\mu(n) = \Omega(n)D_\mu(n)\Omega^\dagger(n), \tag{2.5}$$

$$F_{\mu\nu}(n) \to F'_{\mu\nu}(n) = \Omega(n)F_{\mu\nu}(n)\Omega^\dagger(n). \tag{2.6}$$

This transformation of the covariant derivative and the field strength tensor ensures that $D_\mu\psi$ and ψ transform in the same way, which also implies the invariance of the kinetic term in the Lagrangian.

Before we proceed with the discretization of the QCD action, let us finish this section by writing down explicitly all indices that the quark fields and the gauge fields carry. First, the quark fields carry several indices and arguments: the space-time position denoted by n, Dirac index $\alpha = 1, 2, 3, 4$ according to their spinor property, the flavor index $f = 1, \ldots, N_f$ and the color index denoted by $c = 1, 2, 3$. The gauge fields on the other hand are vector fields on space-time which can be expanded over a basis $T^a = \lambda^a/2$ of the Lie algebra $\mathfrak{su}(3)$, which are constructed from the so-called Gell-Mann matrices[4] λ^a where the index $a = 1, \ldots, 8$. All

particular, they cannot be used to give a notion of an electric charge.

[2] An alternative convention can be obtained by rescaling the gauge field as $A_\mu/g \to A_\mu$, this way the coupling g is moved to the covariant derivative.

[3] In the following we will only work with the Euclidean signature.

[4] We restrict ourselves to the fundamental representation (a non-trivial representation of the smallest di-

together the explicit expression of the fields in QCD reads

$$\psi_f^{c\alpha}(n), \quad \bar{\psi}_f^{c\alpha}(n), \quad A_\mu(n) = \sum_{a=1}^{8} A_\mu^a(n) T^a.$$

In the following those indices will often be suppressed for simplicity.

2.2 Quantum field theory on the lattice

Despite the fact that quantum field theory provides an amazingly accurate theoretical framework for describing the behavior of subatomic particles and forces, understanding the strong coupling dynamics of QCD remains one of the daunting challenges of theoretical particle physics. This is because at large separation, forces between quarks become strong and this precludes the usage of perturbation theory. Fortunately, there exists a formalism called *lattice gauge theory* which was originally introduced by Wilson in 1974 [45]. This theory opens a new window for studying QCD non-perturbatively, and the early work of application of the Monte-Carlo method to lattice gauge theory [46, 47] in connection with our current computer power gives us a very practical reason for studying lattice gauge theory. It is instructive to review briefly a lattice gauge theory with the so-called Wilson fermions which will be a central object throughout this thesis. A full and detailed formal introduction can be found in, for example [48–50].

2.2.1 Gauge fields on the lattice

It is convenient to start with the concepts of lattice gauge theory in the SU(3) Yang-Mills theory or SU(3) pure gauge theory. As we will see later, the pure gauge theory on the lattice is much easier concerning numerical simulations, and its effective theory derived by using a strong and a character expansion can be evaluated analytically by means of series expansion methods. While the presence of fermion fields increases complexity for both analytic and numerical calculations drastically. We emphasize that even though pure gauge theory is much simpler to deal with, this theory shows already most of the relevant phenomena in lattice gauge theory.

The first step in the lattice formulation is the introduction of the four-dimensional lattice Λ with lattice spacing a and four basis vectors $\hat{\mu}$ each of unit length where $\mu = 0, 1, 2, 3$

$$\Lambda = \{n = \sum_{\mu=0}^{3} a n_\mu \hat{\mu} | n_1, n_2, n_3 = 0, 1, \ldots, N_s - 1, n_0 = 0, 1, \ldots, N_t - 1\}. \tag{2.7}$$

Here N_s is the spatial extent and N_t is the temporal extent of the lattice. The lattice spacing plays the role of the inverse ultra-violet cut-off in our theory

$$a = \frac{1}{\Lambda_{UV}}. \tag{2.8}$$

The lattice becomes a good approximation only if a is much smaller than other physical length scales in the system.

---

mension) of the $\mathfrak{su}(3)$ Lie algebra.

To derive the formalism of pure gauge theory on the lattice, it is instructive to understand the naive discretization of free fermions before trying to involve interactions. The Lagrangian for a free fermion in Euclidean spacetime is given by

$$\mathscr{L}(\psi, \bar{\psi}) = \bar{\psi}(n)(\gamma_\mu \partial_\mu + m)\psi(n). \tag{2.9}$$

To formulate the corresponding action on the lattice one needs to discretize both the integral over space-time and the partial derivative. The integral and the partial derivative are replaced by a sum over Λ and the $\mathcal{O}(a)$-improved derivative, i.e. lattice artifacts are of $\mathcal{O}(a)$, respectively

$$\partial_\mu \psi(x) \to \frac{1}{2a}\left(\psi(n+\hat{\mu}) - \psi(n-\hat{\mu})\right). \tag{2.10}$$

To ensure the discretized action invariant under gauge transformations, gauge fields $U_\mu(n)$ - elements of the gauge group SU(3) - must be introduced. These matrix-valued variables are oriented and should be attached to the links connecting the sites n and $n+\hat{\mu}$ rather than on the sites themselves, thus they are often called *link variables*. In the continuum, the so-called gauge transporter is defined as

$$G(n,m) = P \exp\left(i \int_{\mathcal{C}_{nm}} A \cdot \mathrm{d}s\right), \tag{2.11}$$

where $G(n,m)$ is the path-ordered exponential integral of the gauge field A_μ along some curve $\mathcal{C}_{nm}$ connecting two points n and m and transforms under a gauge transformation (2.4) as

$$G(n,m) \to \Omega(n) G(n,m) \Omega(m). \tag{2.12}$$

The link variables $U_\mu(n)$ with a path where n and $n+\hat{\mu}$ are endpoints of this path, share the same transformation properties with parallel transporters in the continuum. In the presence of matter field, the link variable $U_\mu(n)$ parallel transports a matter field from the site n to $n+\hat{\mu}$ on the SU(3) gauge manifold. Thus, one can associate the link variables $U_\mu(n)$ to the A_μ gauge fields as follows

$$U_\mu(n) = \exp(-iaA_\mu(n)) \in \mathrm{SU}(3). \tag{2.13}$$

It is easy to see that the SU(3) properties of the link variables are preserved because the A_μ gauge fields are elements of the $\mathfrak{su}(3)$ Lie algebra. The definition of the link variables in (2.13) also implies that to obtain a link variable that point in negative μ direction we can take its Hermitian conjugate at $n-\hat{\mu}$

$$U_{-\mu}(n) = U_\mu^\dagger(n-\hat{\mu}). \tag{2.14}$$

The discretized partial derivative in (2.10) can be combined with the link variables and leads to the *improved covariant derivative*

$$D_\mu \psi(n) = \frac{1}{2a}\left(U_\mu(n)\psi(n+\hat{\mu}) - U_{-\mu}(n)\psi(n-\hat{\mu})\right). \tag{2.15}$$

The Lagrangian including the lattice covariant derivative is invariant under gauge transforma-

tions, i.e. the fermion fields and the links transform respectively as

$$\psi'(n) = \Omega(n)\psi(n), \tag{2.16}$$
$$U'_\mu(n) = \Omega(n)U_\mu(n)\Omega^\dagger(n+\hat{\mu}). \tag{2.17}$$

Let us make some comments on the native continuum limit of the fermion action. The Lagrangian from (2.9) including the lattice covariant derivative indeed reproduces the continuum action up to artifacts of $\mathcal{O}(a^2)$ when taking $a \to 0$, but this naive discretization has a problem called *fermion doubling*, i.e. there are 16 times too many fermions as we take the continuum limit. These doublers are unphysical poles of the lattice Dirac operator in momentum space within the Brillouin zone $-\pi/a < p \leqslant \pi/a$. As mentioned in the introduction, throughout this thesis we mainly focus on the Wilson fermion action, which removes the doubles by adding a new term to the action. Unfortunately, there is a drawback that this new term cannot preserve the chiral symmetry of QCD action even for the $m \to 0$ limit. This is a consequence of the Nielsen-Ninomiya theorem [51] which states that on the lattice chiral symmetry through the relation

$$\{D, \gamma_5\} = D\gamma_5 + \gamma_5 D = 0 \tag{2.18}$$

and a doubles-free theory cannot be implemented at the same time. This theorem held the development of lattice QCD for many years before the discovery of the Ginsparg-Wilson equation [52]. More details of the Nielsen-Ninomiya theorem and chiral symmetry on the lattice can be found in e.g. [48].

With the introduced link variables $U_\mu(n)$ we can write down an action that satisfies the following demands; gauge invariance, locality, and isotropy. We can achieve this by first considering the simplest gauge invariant combination of gauge fields on the lattice that can be constructed by multiplying together a string of four neighboring link variables and then taking the trace. This shortest, nontrivial closed loop on the lattice is called the *plaquette*. The plaquette variable $U_{\mu\nu}(n)$ is given by

$$U_P = U_{\mu\nu}(n) = U_\mu(n)U_\nu(n+\hat{\mu})U^\dagger_\mu(n+\hat{\nu})U^\dagger_\nu(n), \tag{2.19}$$

which is the smallest loop of size $a \times a$ on the lattice. Based on the plaquettes the Wilson gauge action can be constructed by summing over all plaquettes as follows

$$S_G[U] = \beta \sum_{n,\mu<\nu} \left[1 - \frac{1}{3}\mathrm{Re\,tr}\, U_{\mu\nu}(n)\right], \tag{2.20}$$

which takes the simplest real and gauge invariant expression. Here each plaquette is counted with only one orientation. The sum runs over all lattice points n as well as over the Lorentz indices where $\mu < \nu$. β is called the lattice coupling and for SU(3) group it is related to the bare coupling g as $\beta = 6/g^2$. It is possible to show that the action of (2.20) approaches the continuum gauge action up to terms of $\mathcal{O}(a^2)$. It is important to point out that the lattice artifacts of $\mathcal{O}(a^2)$ can be eliminated by applying the so-called Symanzik improvement program [53,54], which leads to an improved action that includes additional larger loops which cancel precisely the terms of higher order in a.

2.2.2 Fermion fields on the lattice

The naive discretization of the free fermion fails to give the correct continuum limit due to the problem of fermion doubling. In this section, we consider the fermion contribution with the correct statistics and the correct continuum limit to obtain the full action of lattice QCD. From the naive discretization combined with the Wilson term which is a discretization of a second derivative $-a/2\partial_\mu\partial_\nu$[5], the pre-factor a implies that the Wilson term vanishes as the action approaches the continuum limit $a \to 0$ [45]. This term helps decouple the physical from the double sector. The total QCD Lagrangian is given by

$$S[U, \psi, \bar{\psi}] = S_G[U] + S_F[U, \psi, \bar{\psi}], \tag{2.21}$$

where the Wilson gauge action S_G is given in (2.20), and the fermion term S_F is quadratic in fermions which takes the following form

$$S_F[U, \psi, \bar{\psi}] = a^4 \sum_{f=1}^{N_f} \sum_{n,m} \bar{\psi}_f(n) D(n|m) \psi_f(m). \tag{2.22}$$

Here $D(n|m)$ is called the Wilson-Dirac operator. According to the indices of the Lagrangian; the number of lattice site $n = 1, \ldots, N$, the number of colors $c = 1, 2, 3$ and the Dirac index $\alpha = 1, \ldots, 4$, this matrix has the size of $12N \times 12N$. The Wilson-Dirac operator can be written in the following form

$$D(n|m) = -\frac{1}{2a} \sum_{\mu=1}^{4} \left[(r - \gamma_\mu) U_\mu(n) \delta_{n,m-\hat{\mu}} + (r + \gamma_\mu) U_{-\mu}(n) \delta_{n,m+\hat{\mu}} \right] + \left(m_f + \frac{4r}{a} \delta_{n,m} \right), \tag{2.23}$$

where we have defined

$$\gamma_{-\mu} = -\gamma_\mu, \qquad \mu = 0, 1, 2, 3. \tag{2.24}$$

With this representation for the Wilson-Dirac operator one can easily show that it satisfies the condition of γ_5-hermiticity

$$\gamma_5 D \gamma_5 = D^\dagger. \tag{2.25}$$

Here we note that physical quantities cannot depend on the coefficient r since the Wilson term is a lattice artifact that vanishes in the continuum, therefore it can be chosen freely. From now on, for our convenience we set $r = 1$. Furthermore, for $r \neq 0$ this action breaks chiral symmetry even for zero quark masses at finite lattice spacing. This is evident from the additional $4/a$ term which is added to the bare quark mass in (2.23). The quark mass and the chiral condensate $\langle \bar{\psi}\psi \rangle$ obtain an additive renormalization. For Wilson fermions, the bare quark mass is consequently given by the following quark mass

$$m_b = m - m_c, \quad m_c = m_c(\beta) \neq 0 \text{ for finite } \beta \tag{2.26}$$

Within the scope of numerical simulations, it is important to properly renormalize the mass before approaching the continuum limit. This step can be done by choosing a fixed renormalized

[5]There exists another method to overcome the doubling problem called the Kogut-Susskind or staggered discretization, but this method is out of the scope of this thesis.

quark mass when reaching the continuum.

The Wilson term has a lattice artifact of $\mathcal{O}(a)$, while the naive discretization has the lattice artifact of $\mathcal{O}(a^2)$, indicating that we have introduced a term that slows down the approach to the continuum. We emphasize again that this problem can be solved by the usage of the Symanzik improvement program. This program leads to additional terms in the action when it is applied to remove the artifacts of $\mathcal{O}(a)$ [55]. The final result is known as $\mathcal{O}(a)$-improved Wilson fermions, which are normally used in large scale simulation projects rather than unimproved ones.

For completeness, we also want to point out the discrete symmetries of the Wilson action. The Wilson-Dirac operator is invariant under parity P, charge conjugation C, and time reversal T. These discrete symmetries ensure the consistency of the Wilson action.

2.2.3 Hopping parameter representation

There is another convenient form for the fermion action called the hopping parameter representation. This representation later will become important for deriving an effective theory from lattice QCD. The hopping parameter

$$\kappa = \frac{1}{2(am_b + 4)} \tag{2.27}$$

is a real number and related to the bare quark mass m_b. The hopping parameter κ is proportional to the inverse of the quark mass, thus it becomes small for large quark mass. As the hopping parameter κ is introduced, the Wilson-Dirac operator in (2.23) can be reformulated as

$$D = C(\mathbb{1} - \kappa H). \tag{2.28}$$

Here H is called the hopping operator, and the pre-factor C is irrelevant, since it can be absorbed in a rescaled fermion fields as follows

$$\psi \to \sqrt{C}\psi, \qquad \bar{\psi} \to \sqrt{C}\bar{\psi}. \tag{2.29}$$

These fermion fields are integrated out later to avoid direct simulations of fields that take values in a Grassmann algebra. We then obtain a new form of the Wilson-Dirac operator

$$D = \mathbb{1} - \kappa H, \tag{2.30}$$

which allows us to perform the so-called hopping expansion in the limit of large quark mass. The hopping parameter expansion provides an analytic way of studying the effects of dynamical fermions on physical observables.

2.2.4 The path integral for lattice gauge theory

Since the thermodynamic aspect of the theory is what we are interested in, in this section we consider the formal lattice formalism of statistical QCD. The finite-temperature behavior of any theory is specified by the canonical partition function

$$Z(T) = \mathrm{tr}(e^{-\beta\mathscr{H}}), \tag{2.31}$$

where $\mathscr{H}$ is the Hamiltonian of the theory, and the quantum mechanical trace is a sum over all energy eigenstates of the Hamiltonian. For a system with N_q quarks, it must be treated in the grand canonical ensemble, which allows us to study the case where there is an exchange of particles with the reservoir. This ensemble gives the same description as the canonical ensemble for physical observables in the thermodynamic limit. The grand canonical partition function of the theory reads

$$Z_g(\mu, T) = \operatorname{tr} e^{-\beta(\mathscr{H}-\mu N_q)}, \tag{2.32}$$

where μ is the chemical potential. The thermal expectations of physical observables in the canonical and grand canonical ensemble are given by

$$\langle \mathcal{O} \rangle = \frac{1}{Z} \operatorname{tr}\left(e^{-\beta\mathscr{H}}\mathcal{O}\right) \qquad \text{or} \qquad \langle \mathcal{O}_g \rangle = \frac{1}{Z_g} \operatorname{tr}\left(e^{-\beta(\mathscr{H}-\mu N_q)}\mathcal{O}_g\right). \tag{2.33}$$

Here with the natural unit $k_B = 1$, the coupling $\beta = 1/T$ is the inverse temperature.

Based on [56], the path integral representation for gauge theories [57,58] has been developed. For lattice gauge theory, the ground-state expectation value of physical observables as functions of the link variables U, and the fermion fields, is given by

$$\langle \mathcal{O}[U, \psi, \bar{\psi}] \rangle = \frac{1}{Z} \int \mathscr{D}U \mathscr{D}\psi \mathscr{D}\bar{\psi} \exp\left(-S[U, \psi, \bar{\psi}]\right) \mathcal{O}[U, \psi, \bar{\psi}]. \tag{2.34}$$

Here Z is the partition function

$$Z = \int \mathscr{D}U \mathscr{D}\psi \mathscr{D}\bar{\psi} \exp\left(-S[U, \psi, \bar{\psi}]\right), \tag{2.35}$$

and the integration measure for a generic field ϕ takes the simple product form over all lattice sites and its indices as

$$\mathscr{D}\phi = \prod_{n,\alpha} \mathrm{d}\phi_\alpha(n), \tag{2.36}$$

where for $\phi = U$, $\mathrm{d}U(n)$ is the Haar measure on the continuous compact group G. Explicitly, for the link variables and the fermion fields the path integral measure is defined by

$$\mathscr{D}U = \prod_{n,\mu} \mathrm{d}U_\mu(n), \qquad \mathscr{D}\psi = \prod_{n,c,\alpha} \mathrm{d}\psi^c_\alpha(n). \tag{2.37}$$

The Haar measure is chosen based on the gauge invariance of the path integral. The group measure should fill the group volume uniformly so that it is not changed by a gauge transformation, thus it makes sense to demand

$$\mathrm{d}U = \mathrm{d}(UV) = \mathrm{d}(VU), \tag{2.38}$$

for an arbitrary group element $V \in G$, and we also impose a normalization condition so that

$$\int \mathrm{d}U = 1. \tag{2.39}$$

A more detailed discussion of the Haar measure can be found in, for example [48].

From quantum field theory, we know that the fermion fields satisfy a so-called Grassmann algebra[6], and in the QCD functional integral the integration over fermions can be performed analytically and leads to the fermion determinant $\det[D]$. This step is necessary for lattice gauge theory because so far, there is no practical method that would allow performing numerical simulations on Grassmann-valued fields directly. The path integral of N_f flavor lattice QCD with mass-degenerate Wilson quarks can be written as

$$Z = \int \mathscr{D}U \left(\det\left[D[U]\right]\right)^{N_f} e^{-S_G[U]}. \tag{2.40}$$

We focus on the properties of the expectation values of observables $\mathcal{O}$ under a gauge transformation. Under a gauge transformation of the form $U \to \Omega U \Omega^\dagger$, where Ω represents the gauge transformation for a full configuration of link variables[7], the expectation value reads

$$\langle \mathcal{O} \rangle = \frac{1}{Z} \int \mathscr{D}(\Omega U \Omega^\dagger) \mathcal{O}[\Omega U \Omega^\dagger] \left(\det\left[D[\Omega U \Omega^\dagger]\right]\right)^{N_f} e^{-S_G[\Omega U \Omega^\dagger]}. \tag{2.41}$$

The action and the measure of the path integral are invariant under gauge transformations. Thus,

$$\langle \mathcal{O} \rangle = \frac{1}{Z} \int \mathscr{D}U \mathcal{O}[\Omega U \Omega^\dagger] \left(\det\left[D[U]\right]\right)^{N_f} e^{-S_G[U]}. \tag{2.42}$$

Physical observables are gauge invariant so the above equation implies that physical observables correspond to gauge invariant operators on the lattice. By integrating over all possible gauge fields one obtains that the expectation value of any non-gauge invariant functional is equal to the expectation of its average over the gauge group. This implies that we may integrate over all possible gauge fields Ω without changing the expectation value

$$\langle \mathcal{O} \rangle = \frac{1}{Z} \int \mathscr{D}U \mathscr{D}\Omega \left(\det\left[D[U]\right]\right)^{N_f} e^{-S_G[U]} \mathcal{O}[\Omega U \Omega^\dagger] = \int \mathscr{D}\Omega \langle \mathcal{O}[\Omega U \Omega^\dagger] \rangle. \tag{2.43}$$

The consequence of (2.43) is that for operators which include both gauge invariant and gauge variant contributions, only the gauge invariant remains after performing the path integral. Furthermore, due to the demand of gauge invariance all observable which only include gauge degrees of freedom are necessarily made of closed loops of link variables. If fermionic degrees of freedom are absent, then a closed loop is the only possibility to maintain gauge invariance. In addition, gauge invariance can be ensured by either taking the trace or the determinant for each closed loop.

2.3 The continuum limit

To obtain physical results from lattice calculations, which are independent of the underlying lattice structure, one must take the continuum limit. In a naive sense, this step is related to the procedure of sending the lattice spacing $a \to 0$. However, the lattice spacing a is not a free parameter rather it is generated dynamically in the simulations. In this section, we will explain

[6]Recall that the Grassmann algebra for a fermion field ψ is an anti-commutation relation that yields $\{\psi(x), \psi(y)\} = 0$.

[7]For our convenience, we consider only the link variables here, and the value of Ω can be chosen arbitrarily.

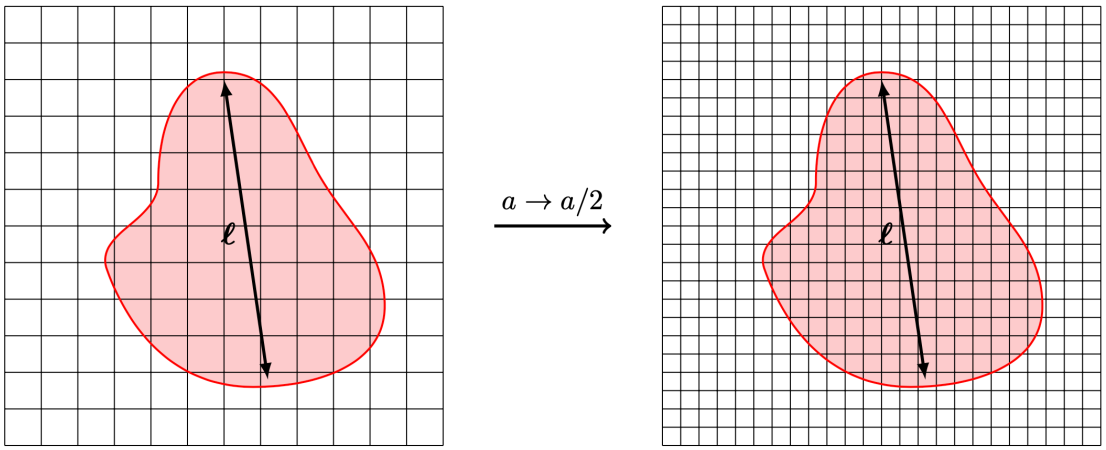

Figure 2.1: Structure with an intrinsic physical length scale ℓ by decreasing the lattice spacing with a factor of two. Figure taken from [59].

briefly how the simulation parameters can be tuned such that one approaches the continuum.

So far, we have regularized the QCD action on the lattice and showed that our regularization is correct by carrying out the naive $a \to 0$ limit. However, the discretization procedure is not unique, in fact, there are infinitely many ways to discretize our theory that give the same continuum limit. When trying to remove the lattice cutoff, physical observables should not depend on a and agree with the corresponding experimental values. This implies that the bare parameters have a nontrivial dependence on the cutoff a. It should be pointed out that to show that a discrete action approaches the correct continuous one in the naive limit is not sufficient to ensure that the discrete theory coincides with continuum QCD.

Asymptotically free theories. For an asymptotically free theory like QCD, decreasing the lattice spacing corresponds to a consideration of the theory at smaller distances. Furthermore, asymptotic freedom demands that the theory becomes free as it approaches the continuum limit and in this case the bare coupling $g \to 0$. We already know from renormalization theory, that this does not mean that the theory in the continuum is free, approaching the continuum is instead a similar step by which the lattice structure as a regulator is removed in the process of renormalization. The relevant coupling is the renormalized coupling g_r at scale μ_E associated with the process of interest.

The continuum limit as a second-order phase. The distinction between the bare and renormalized coupling can be explained as follows, consider a physical quantity such as a meson with an intrinsic length scale ℓ, see fig. 2.1. The fields inside this meson are correlated at a length scale proportional to $\ell \sim \xi$ where ξ is the correlation length of the system. The quantity ℓ is a physical constant, irrespective of how it can be measured on the lattice. On the other hand, when we express ℓ in terms of the lattice spacing a as $\ell = a\xi$. It is clearly that for ℓ to remain constant as $a \to 0$, the corresponding correlation length has to diverge: $\xi \to \infty$. In the language of statistical mechanics, this characterizes a second-order phase transition. In other words, a lattice theory with a well-defined continuum limit needs to approach a second-order phase transition in this limit[8].

The renormalization group equation for g. From QCD renormalization, a given energy

[8]In the strong coupling limit, the required second-order phase does not occur because the correlation length goes to zero as β becomes small. Thus, to approach the continuum limit we must look at the region of intermediate and small coupling

scale μ_E provides a relevant scale for the renormalized coupling g_r[9]. Furthermore, the cutoff $\Lambda \sim 1/a$ is the relevant scale for the bare coupling. By using the renormalization group equation for g_r including the fact that the renormalization constant only depends on the dimensionless ratio Λ/μ_E, the relation between the bare coupling g and the lattice spacing a is determined up to an integration constant through the Callan-Szymanzik lattice β-function [60, 61]

$$\beta_{\text{lat}}(g) = -a\frac{\partial g}{\partial a} = -\beta_0 g^3 - \beta_1 g^5 + \mathcal{O}(g^7). \tag{2.44}$$

Here β_{lat} has the same leading-order perturbative series as β_r. For SU(N_c) groups, the first two leading terms in the β-function do not depend on the regularization and thus are universal for all lattice discretization of QCD as well as equivalent to the ones from perturbation theory. However, we note that at higher orders the β function is in general dependent on the details of regularization. The leading order term for β_{lat} is positive for $N_c \geqslant 2$, which implies that g has to decrease as $a \to 0$, so an ultra-violet fix-point for $g \to 0$ is ensured, as needed for the existence of a continuum limit. A detailed discussion of the renormalization group and the running coupling can be found in [59, 62, 63].

Scaling and perturbative scaling. The fixpoint locates at vanishing coupling, therefore physical quantities will be scaled consistently with the scaling predicted from lattice perturbation theory [62]. We use the term *perturbative scaling*. Note that at leading order the perturbative running is universal. However, simulations with control over systematic effects such as finite size effects are too expensive by setting in perturbative scaling.

In practice, we do not rely on perturbative scaling, rather we consider a dimensionless observable or a dimensionless ratio of physical observables, and simulate in the region where the expectation values scaling with a^q at the leading order. This procedure provides a big advantage over a setting for perturbative scaling, since the scaling region sets in much earlier, so that a controlled continuum extrapolation can be done with lattice spacings in reach for the simulations.

The thermodynamics and continuum limit. We consider the infinite volume limit which is typically called the *thermodynamic limit*

$$N_s \to \infty, \qquad N_t \to \infty.$$

This limit has a peculiar interference with the continuum limit because on one hand, the continuum limit corresponds to a second-order phase transition i.e. the correlation length ξ diverges. On the other hand, if we consider only a finite lattice, ξ is bounded from above by the length N_μ of the smallest lattice direction. Thus ξ can only diverge in the infinite volume limit. Consequently, the infinite volume limit has to be taken before the continuum limit.

However, this is not possible in practice since the infinite volume limit for each lattice spacing becomes expensive. Instead, the continuum limit is performed in a fixed physical volume, i.e. $N_\mu \to \infty$ for $a \to 0$ while keeping $L_\mu = a \cdot N_\mu$ fixed. When the volume is large enough, the finite size effects are negligible. In principle, one still needs to check whether in this case neglecting finite size effects is consistent by performing a similar continuum limit for different volumes.

MC autocorrelation times and the continuum limit. By approaching the continuum limit that is characterized by the second-order point, fluctuations are strongly suppressed. The same phenomenon happens to changes in the Markov chain, so that the autocorrelations increase. The autocorrelation length scales usually like $\xi \sim a^{-z}$ where z is a dynamical critical

[9] We concentrate on the pure gauge theory for simplicity.

exponent which depends on the theory of interest. A measure of the autocorrelations in MC time τ_{auto} is called *autocorrelation length*, and it should scale similar to ξ in the approach to the continuum limit.

2.4 Temperature and chemical potential

In this section, we discuss how temperature and chemical potential, the main quantities that characterize the QCD phase diagram, can be introduced on the lattice and how they can be varied.

2.4.1 Introduction of temperature

Quantum field theory in Minkowski space-time has one distinguished direction, the temporal direction t, and three spatial dimensions. Upon analytic continuation, it becomes a four-dimensional theory where time plays no special role anymore. On the other hand, in the language of *equilibrium statistical mechanics*, there is no time, or in other words, everything is frozen, but there is a temperature T which can be considered as the fourth dimension of equilibrium statistical mechanics. Considerations above point out the very deep relation between quantum field theory and statistical mechanics. Euclidean quantum field theory in four dimensions is equivalent to statistical mechanics in three dimensions: the fourth dimension of quantum field theory, the time t, is mapped to the inverse temperature of a statistical model: $t \sim 1/T$. Generally, one usually refers to this fact as an equivalence between Euclidean quantum field theory in $(d+1)$-dimensional space-time and statistical mechanics in d dimensions.

Again, for a quantum mechanics system the partition function can be expressed as

$$Z(T) = \text{tr}\left[e^{-\beta\mathscr{H}}\right]. \tag{2.45}$$

Here $\beta = 1/k_B T$, where T is temperature and k_B is the Boltzmann constant[10]. To connect our field theory to a statistical mechanics system, due to the trace in (2.45) it is necessary to restrict our fields to be periodic (bosons) and anti-periodic (fermions) in time and the temporal extent to be finite. With these restrictions, the partition function for a generic field ϕ is given by

$$Z(T) = \int \mathscr{D}\phi e^{-S_E[\phi]}. \tag{2.46}$$

Here the field ϕ is periodic or anti-periodic in the finite time direction, and the Euclidean action S_E now is

$$S_E[\phi] = \int_0^\beta \mathrm{d}t \int \mathrm{d}^3x \mathscr{L}[\phi, \partial_\mu \phi]. \tag{2.47}$$

The measure $\mathscr{D}\phi$ and the action S_E are discretized on the lattice in the standard procedure. So far, at zero temperature we were interested in results in the infinite space-time limit. The space-time scale in this case is much larger than the largest correlation length in the system. Now the time extent is restricted to β. For a finite lattice the spatial extent is aN_s and the

[10]It is easy to get confused by the notation of β in this section with the inverse gauge coupling. Unless stated otherwise, we use β here as the inverse temperature

temporal extent is aN_t, the inverse temperature β is related to N_t by

$$\beta = aN_t = \frac{1}{T}, \tag{2.48}$$

where we can obtain the zero temperature limit by sending β to infinity. If N_s is kept fixed, then this can be interpreted as a system with finite spatial volume and fixed temperature T. To approach the continuum limit for this system, the lattice spacing a goes to zero while keeping aN_s and aN_t fixed. The effects of finite volume in numerical simulations can be controlled if the spatial extent N_s is kept as large as possible so that $N_s \gg N_t$. The reader may find a foundation for quantum field theory at finite temperature in [64], and for thermodynamics of lattice QCD in [48, 50, 65].

2.4.2 Introduction of the chemical potential

As already mentioned above, besides the temperature the QCD phase diagram is also characterized by the so-called chemical potential associated with the vertical axis in fig. 1.1. In contrast to the vacuum, the net number of baryons is finite. The effect of finite quark number becomes strong in extreme situations such as heavy-ion collisions, or ultra-dense matter in neutron stars. To describe these systems the partition function of the grand canonical ensemble must be modified by including the chemical potential coupled to the quark number operator N_q as follows

$$Z(T, \mu) = \mathrm{tr}\left[e^{-(\mathscr{H} - \mu N_q)}\right]. \tag{2.49}$$

Note that there is another convention using the baryon number operator $N_B = N_q/3$ and the baryon chemical potential $\mu_B = 3\mu$. The quark number operator N_q takes integer values, so the grand canonical partition function $Z(T, \mu)$ can be expanded in power series of the *fugacity variable*

$$z = e^{\mu/T}. \tag{2.50}$$

Then the partition function can be re-expressed as a sum over canonical partition functions $Z_n(T)$ for a fixed quark number $n \in \mathbb{Z}$

$$Z(T, \mu) = \sum_n z^n Z_n(T). \tag{2.51}$$

Here the negative values of n represent a net surplus of anti-quarks. The sum over the quark number n is bounded by $|n| \leqslant n_{\max}$ on a finite lattice.

From the grand canonical partition function (2.49), one can compute new observables, for instance the quark number density

$$n_q = \frac{1}{V}\langle N_q \rangle = \frac{T}{V}\frac{\partial \log Z(T, \mu)}{\partial \mu}. \tag{2.52}$$

The phase structure and the location and properties of the finite temperature phase transition are now affected by the quark number density. An investigation of the phase diagram of a physical system at finite chemical potential will become increasingly complicated with the additional parameter μ.

Let us now introduce the quark number density in the lattice action. In the Euclidean formulation, the quark number operator N_q is equivalent to the integral of the fourth component $j_4 = \bar{\psi}\gamma_4\psi$ of the conserved vector current $\bar{\psi}\gamma_\mu\psi$ over the spatial volume. This current is conserved due to the charge conjugation transformation or the axial U(1) symmetry. The naive way of introducing chemical potential on the lattice by adding the term μj_4 in the action (even for free fermions) leads to quadratic divergences in the energy density $\sim (\mu/a)^2$ as approaching the continuum limit [66].

A possible solution for this problem is also provided in [66], where the chemical potential μ on the lattice is introduced by replacing the temporal hopping term in (2.23) with

$$-\frac{1}{2a}\left(e^{a\mu}(\mathbb{1}-\gamma_0)U_0(n)\delta_{n+\hat{0},m} + e^{-a\mu}(\mathbb{1}+\gamma_0)U_0^\dagger(n-\hat{0})\delta_{n-\hat{0},m}\right). \tag{2.53}$$

The choice of forward and backward factor $e^{\pm a\mu}$ is natural since at $\mu = 0$ we can obtain back the original action. Furthermore, a hopping expansion method for the Wilson action allows the fermion determinant to be written as a sum over closed loops. In such a loop the forward hopping factors $e^{a\mu}$ and the backward hopping factors $e^{-a\mu}$ cancel out precisely unless the loop winds around the compact Euclidean time direction.

Given $w \in \mathbb{Z}$ the number of windings for a loop, then its total contribution of the chemical potential is given by $(e^{\pm a\mu})^{wN_t}$. Note that to implement the chemical potential on the lattice, instead of changing all link terms in the time direction one might modify all forward time-directed hopping terms on a single time slice, then the total contribution can be cast in the form

$$e^{a\mu N_t} = e^{\mu/T}, \tag{2.54}$$

and the backward time-directed terms with the inverse factor. The introduction of the chemical potential rises a big challenge in numerical simulations. This problem is called *sign problem*, and we will discuss it in more details in section 5.2. The reader is referred to [48] for more details of the chemical potential on the lattice.

2.5 QCD thermodynamics on the lattice

After a brief introduction to the lattice formalism on QCD, in this section, we show how to connect the concept of lattice gauge theory to thermodynamic systems. We will consider the observables and their corresponding symmetries which contribute the main part for characterizing the thermodynamic properties of the system.

2.5.1 Equation of state

The study of the equation of state is of central importance for the understanding of the thermal properties of any thermodynamic system. The equation of state can be established using observables derived directly from the QCD partition function. The definition of these observables will be present in this section.

In addition to the quark number density given in the formula (2.52), the free energy density

is related to the logarithm of the partition function Z and is of the form

$$f = -\frac{T}{V}\log Z. \tag{2.55}$$

The pressure is computed by

$$p = \frac{\partial(T\log Z)}{\partial V}. \tag{2.56}$$

For a large and homogeneous system, the derivative to the volume V is equivalent to dividing by the volume. Thus, the pressure of such systems is given by

$$p = -\lim_{V\to\infty} f \tag{2.57}$$

One needs to check the validity of these definitions on the lattice formalism. The check can be done employing series expansion methods as one can see in [32], or of simulations [44,67]. Since we have the pressure as a function of temperature T then all other thermodynamic observables can also be derived. The interaction measure[11] δS is obtained from the normalized pressure as follows

$$\delta S(T) = \epsilon - 3p = T^5\frac{\partial}{\partial T}\frac{p(T)}{T^5}. \tag{2.58}$$

This quantity measures the deviation from the equation of state of an ideal gas limit $\epsilon = 3p$. Furthermore, the inverse of this equation can be derived simply as

$$\frac{p(T)}{T^4} = \int_0^T \mathrm{d}T'\frac{\delta S(T')}{T'^5}. \tag{2.59}$$

Based on the pressure p and the interaction measure δS, one can readily compute the energy ϵ, the entropy density s, and the speed of sound c_s

$$\epsilon = \delta S + 3p, \qquad s = \frac{\epsilon + p}{T}, \qquad c_s^2 = \left.\frac{\partial p}{\partial \epsilon}\right|_s. \tag{2.60}$$

We note that the definitions that were introduced above, are functions of one variable T, and they must be modified if the chemical potential involves, for more details see [68]. There are other observables such as the chiral condensate, or the chiral susceptibility associated with an $U(N_f)_L \times U(N_f)_R$ chiral symmetry in the limit $m_q \to 0$. These quantities are relevant for studying phase transitions related to chiral symmetry breaking like the lower-left corner of the Columbia plot in fig. 1.2, however, this topic is out of the scope for this thesis. A more detailed discussion of the chiral quantities can be found in [48].

We note that all presented observables above are based on the free energy density. However, these quantities have been proven to be ultraviolet divergent, thus for these observables to get finite results a renormalization scheme must be introduced. It turns out that by subtracting the $T = 0$ contribution from the free energy density one can get rid of the additive divergences

$$f_r(\alpha, T) = f(\alpha, T) - f(\alpha, T = 0). \tag{2.61}$$

[11] The interaction measure is also often called the trace anomaly.

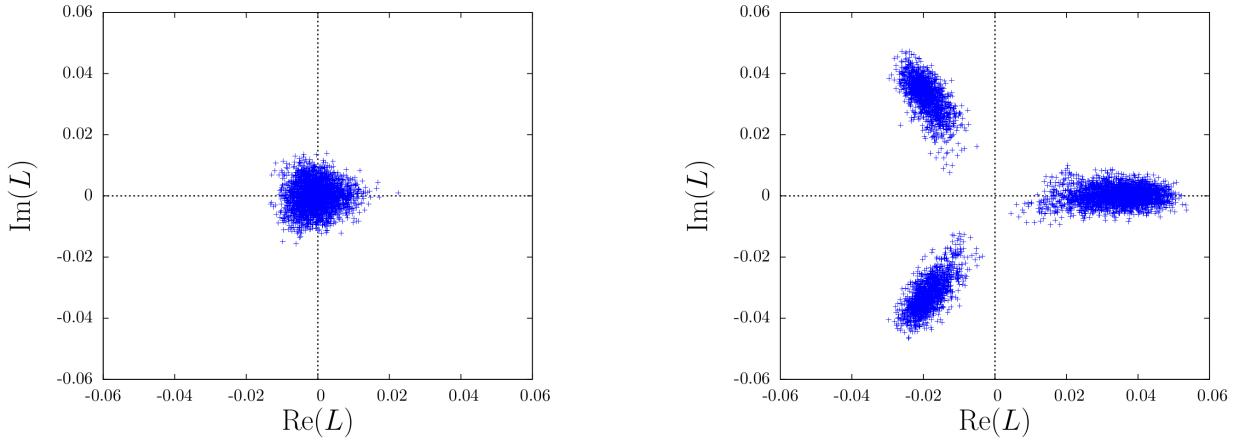

Figure 2.2: Scatters plot of Polyakov loop in the complex plane from SU(3) pure gauge theory. Left: In the confined phase. Right: In the deconfined phase. Figure taken from [71].

Here α is a general bare parameter of the theory, and f_r is the renormalized free energy density. Moreover, the free energy density cannot be directly accessible in Monte-Carlo calculations, on the other hand, expectation values can be calculated easily. Thus, we should compute the difference of the free energy density at two different temperatures

$$\left.\frac{f}{T^4}\right|_{T_0}^{T} = -\frac{1}{V}\int_{T_0}^{T} \mathrm{d}x \frac{\partial x^{-3} \log Z(x,V)}{\partial x}. \tag{2.62}$$

For detailed reviews of the equation of state in lattice QCD see [44, 69, 70].

2.5.2 Polyakov loop and the center symmetry

In lattice simulations, the partition function itself is difficult to treat, and observables measured on the lattice are results of the partial derivative of $\log Z$. These observables are sensitive to the transitions of the QCD phase diagram depending on the regions where we want to investigate. The observables are often referred to as *approximate order parameters* since in the presence of fermion fields there is no true order parameter that has been found yet. As mentioned before, here we discuss only an observable called the Polyakov loop, and the center symmetry associated with the deconfinement transition. Discussion on observables associated with the chiral symmetry can be found in [48].

Polyakov loops. First, we consider a system of gluons only, without any real or virtual quarks. Since gluons can interact directly, they can form bound states ("glueballs" or gluonium states) and undergo a transition from a gluonium gas to one of deconfined gluons. This simplified world is therefore far from trivial – in contrast to the corresponding system in QED, a gas of photons, which in the absence of electrons cannot interact. As we shall see later on, pure gauge field thermodynamics provides a particularly transparent illustration of deconfinement physics [72]. In the absence of fermion fields, the so-called Polyakov loop is a true order parameter.
We start with the description of the Polyakov loop or the thermal Wilson loop. The Polyakov

loop is of the form

$$L = \frac{1}{V}\sum_{\vec{n}} \mathrm{tr} \prod_{n_0=0}^{N_t-1} U_0(n). \tag{2.63}$$

Here we use a convention that the Polyakov is averaged over the spatial volume since a change of a local Polyakov loop will not have much effect on the average if the averaging procedure is performed over enough spacial sites. The expectation value of the Polyakov loop L is connected to the free energy F_q of a single color charge

$$|\langle L \rangle| \sim e^{-F_q/T}. \tag{2.64}$$

Here F_q is correspondent to the free energy of a static quark-antiquark pair[12] when their distance is taken to infinity, i.e. $F_{q\bar{q}}(r \to \infty)$. At low temperature in pure gauge theory, $F_{q\bar{q}}(r)$ diverges as $r \to \infty$, implying $\langle L \rangle = 0$. This is the well-known phenomenon of confinement where to separate a quark and an anti-quark we need infinite large energy. At high temperatures, quarks are no longer confined, and $F_{q\bar{q}}(r \to \infty)$ is finite, which leads to a nonzero expectation value for the Polyakov loop. A nonzero expectation value means that (2.63) is no longer invariant under center transformations and signals the spontaneous breaking of center symmetry[13]. This makes the Polyakov loop a true order parameter of center symmetry in pure gauge theory, meaning that the center symmetry is preserved at low temperatures, and it is spontaneously broken at high temperatures. This can be seen in fig. 2.2. We can now conclude the temperature dependence of the Polyakov loop expectation value

$$|\langle L \rangle| \quad \begin{cases} = 0 & \text{for } T \leqslant T_c \text{ - confinement} \\ \neq 0 & \text{for } T > T_c \text{ - deconfinement} \end{cases} \tag{2.65}$$

where T_c is the critical deconfinement temperature.
In full QCD, dynamical fermions break the center symmetry explicitly because the QCD action is no longer invariant under the center transformation. This affects the Polyakov loop as well, however, it can be used as an approximate order parameter because the transition from hadronic matter to the QGP is still captured by the Polyakov loop. The susceptibility of the Polyakov loop, which is defined as

$$\chi_L = V\left(\langle L^2 \rangle - \langle L \rangle^2\right), \tag{2.66}$$

will be often used throughout this thesis. This quantity peaks at the transition, and the value and position of the peak obey finite size scaling laws which help extrapolate to the infinite volume from finite volume measurements.
The center symmetry. We close this chapter by discussing center symmetry which plays a central role in our study. A true phase transition is related to the effective breaking, or restoration of a symmetry. In the pure gauge theory, the symmetry associated with the deconfinement phase transition is called *center symmetry*. This symmetry is preserved under a topological non-trivial gauge transformation with the boundary conditions

$$\Omega(\vec{n}, n_0 + N_t) = h\Omega(\vec{n}, n_0). \tag{2.67}$$

[12] $F_{q\bar{q}}$ can be considered as the quark-antiquark potential.
[13] An intuitive picture to explain the phenomenon of confinement is to attach to each quark a string

Here h is a constant matrix and an element in the SU(N_c) group. Let us consider a plaquette in the $(\mu, 0)$-plane starting at $t = N_t - 1$, under the center symmetry the temporal plaquette transform according to

$$\begin{aligned} U_{\mu 0}(\vec{n}, N_t - 1) \to & \Omega(\vec{n}, N_t - 1) U_\mu(\vec{n}, N_t - 1) \\ & U_0(\vec{n} + \hat{\mu}, N_t - 1)\Omega^{-1}(\vec{n} + \hat{\mu}, 0)h^{-1} \\ & \Omega(\vec{n} + \hat{\mu}, 0)U_\mu^\dagger(\vec{n}, 0)\Omega^{-1}(\vec{n}, 0)h\Omega^{-1}(\vec{n}, 0) \\ & U_0^\dagger(\vec{n}, N_t - 1)\Omega^{-1}(\vec{n}, N_t - 1). \end{aligned} \tag{2.68}$$

According to (2.67), the factor h only appears when the link crosses the boundary. Under such a gauge transformation the plaquette action is invariant if the constant matrix h commutes with all elements of SU(N_c), i.e.

$$[U, h] = 0, \qquad \text{for all} \quad U \in \mathrm{SU}(N_c). \tag{2.69}$$

This is precisely the definition of the center Z_{N_c} of SU(N_c)[14], whose elements are

$$h = e^{2\pi i n/N_c}\mathbb{1}, \quad n \in \{0, 1, \ldots, N_c - 1\}. \tag{2.70}$$

A gauge transformation associated with the boundary conditions (2.67) where $h \in Z_{N_c}$ is called *center transformation*. While the action is invariant under center transformations, the Polyakov does not close in a topologically trivial way but instead winds once around the compact temporal direction, which does not hold the invariance of the Polyakov loop under center transformations. The Polyakov loop transform as

$$L \to hL. \tag{2.71}$$

A phase transition is associated with the corresponding symmetry breaking. For $\langle L \rangle = 0$, it follows that center symmetry is restored within the theory, and as soon as the Polyakov loop acquires a non-zero expectation value, or in other words, it is in the deconfined phase, the center symmetry is spontaneously broken. Thus, the finite temperature transition of QCD in the quenched limit possesses a spontaneous breaking of the center symmetry [73]. The Polyakov loop is an order parameter for distinguishing between a confinement phase, where free charges cannot be found, and a deconfinement phase, where single charges are screened and may be observed.
In the case of broken center symmetry and a finite volume the results for the Polyakov loop will populate the different center sectors with equivalent probability so that both the real and the imaginary parts will vanish in the ensemble average [59]. Consequently, the eqn. (2.65) is no longer valid in a strict sense, since it implies that $|\langle L \rangle| = 0$. This is related to a so-called finite volume effect, where the spontaneous breaking of a true symmetry of the action cannot be observed in a finite volume. On the other hand, the tunneling between center sectors is forbidden at infinite volume, meaning the expectation value of an observable is computed within one particular center sector. In the thermodynamic limit, the measurement of a local quantity on a single configuration already provides a reasonably good estimate for the expectation value of the observable. We note that $\langle L \rangle$ vanishes for sufficiently long simulations, and in the infinite volume, we have $|\langle L \rangle| = \langle |L| \rangle$. Thus, $\langle |L| \rangle$ is usually used instead of $|\langle L \rangle|$, which

[14]The center $Z(G)$ of a group G is defined as $Z(G) = \{h \in G \,|\, \forall g \in G, h \cdot g = g \cdot h\}$.

indeed can serve as an estimator for the order parameter in a finite volume. However, series expansion methods are performed on an arbitrary large volume corresponding to an infinite volume, where the standard expectation value of the Polyakov loop $\langle L \rangle$ can still be employed.

Chapter 3

An effective theory for lattice QCD

> The results were very accurate and completely confirmed my hypothesis that the local couplings of the shortest range were the most important.
>
> *K. G. Wilson, Nobel Lecture*

In this chapter, we introduce an effective theory for lattice QCD which will be shown to be a prominent way to handle some difficulties of the sign problem of QCD at finite chemical potential, at least for heavy quarks. Furthermore, the effective theory can reproduce the full theory in a relevant parameter region. The first advantage of the effective theory is that although the sign problem still occurs in simulations at finite chemical potential, it got milder after integrating out some degrees of freedom of the theory. This enables the standard Monte-Carlo methods with reweighting techniques to circumvent the sign problem and access the region of desired chemical potentials. In addition, we can treat the effective theory using analytic approaches which are completely unaffected by the sign problem.

The starting point is the strong coupling expansion and some of its important results. We then consider the character expansion which helps to reorder the coupling β into an effective coupling $u(\beta)$. The effective coupling has a better convergence and plays a role as an expansion parameter in the pure gauge sector. The last expansion scheme is called the hopping parameter expansion, which is used to expand the Wilson-Dirac determinant around heavy fermions. The resulting series is in powers of the hopping parameter κ. We describe a graph representation method that provides a way to derive higher orders of the effective theory.

3.1 Effective Polyakov loop theory

The core idea of the effective theory is to integrate out spatial link variables so that it has fewer degrees of freedom left. This means that the effective theory is easier to solve numerically than full lattice QCD. If the chemical potential is present, then the sign problem becomes milder in the effective theory, allowing the standard Monte-Carlo methods to be used. The effective theory is defined by integrating out the spatial link variables

$$Z = \int \mathscr{D}U_\mu \det[D] e^{-S_G[U]} = \int \mathscr{D}U_0 e^{-S_{\text{eff}}}, \tag{3.1}$$

under which

$$S_{\text{eff}} = -\log \int \mathscr{D}U_i \det[D] e^{-S_G[U]}. \tag{3.2}$$

While the action (3.2) is unique and exact, an analytic evaluation without some sort of approximations and truncations is not possible. Thus, we will introduce two expansion schemes: the character expansion and the hopping parameter expansion, which will then enable us to evaluate the action (3.2).

It is useful to separate the Z_{N_c} center symmetric from a part with symmetry breaking terms

$$S_{\text{eff}}(W) = S_1(W) + S_2(W), \tag{3.3}$$

where the resulting effective theory only depends on W the temporal Wilson lines

$$W_{\vec{n}} = \prod_{t=0}^{N_t-1} U_0(\vec{n}, t) \tag{3.4}$$

Here S_1 contains all contributions from the pure gauge action, and it can be determined requiring the character expansion. On the other hand, the fermion determinant contains the winding fermion loops with gauge corrections and can be determined by using the hopping parameter expansion.

3.2 Character expansion

It is instructive to start this chapter with a strong coupling expansion. This is an expansion in powers of $1/g^2$ and has an important property that it has a finite radius of convergence [74]. The strong coupling expansion provides a method of computation similarly to the high-temperature expansion or hopping expansion for scalar field theories [75]. Even though the strong coupling expansion cannot exhibit the continuum limit, it still gives insight into the qualitative behavior of lattice gauge theory such as confinement and the particle spectrum. In this section we give basic ideas of the strong coupling expansion, and how the character expansion can help order the couplings β in a systematic way. A detailed review for strong coupling expansion can be found in [50, 76].

Consider the pure gauge action, we note that up to a constant which can be absorbed into the normalized factor of the path integral, the pure gauge action (2.20) can be rewritten as follows

$$S_G = -\frac{\beta}{2N_c} \sum_P (\operatorname{tr} U_P + \operatorname{tr} U_P^*) = -\beta \sum_P S_P. \tag{3.5}$$

Here U_P is the elementary plaquette defined in (2.19). At large couplings or small β, it is convenient to expand the Boltzmann weight in powers of β

$$e^{-S_G} = \prod_P e^{\beta S_P} = \prod_P \left[1 + \beta S_P + \beta^2 S_P^2 + \dots\right], \tag{3.6}$$

and to integrate order by order over the link variables. Notice that, in (3.6) a given plaquette can appear an arbitrary number of times due to the power of S_P. In practice, there is a

convenient way to sum part of this expansion such that a given plaquette appears at most once. There is a sophisticated method for organizing the strong coupling expansion called the character expansion. This expansion scheme is used in higher-order calculations to reduce the number of contributions to a given order in the expansion. The character expansion is similar to a Fourier transformation method. Consider the weight of the pure gauge theory in terms of (3.5)

$$e^{-S_G} = \prod_P e^{\beta S_P}. \tag{3.7}$$

Here S_P is constructed from U_P, and it is a gauge-invariant function i.e.

$$S_P(VU_PV^\dagger) = S_P(U_P), \tag{3.8}$$

where V is an element of SU(3). S_P is a function of only the eigenvalues of U_P, and is called *class function* since it depends only on the conjugacy class of U_P. Any class function can be expanded in characters [77]

$$e^{S_P} = u_0(\beta)\left[1 + \sum_{r\neq 0} \mathrm{d}_r u_r(\beta)\chi_r(U_P)\right]. \tag{3.9}$$

Here χ_r is the character, it is the trace of the irreducible representation of the group with matrix elements D_r^{ij}. The characters form a complete orthogonal basis for gauge-invariant functions. d_r is the dimension of the representation. $u_0(\beta)$ is factored out, because it is irrelevant and can be normalized by performing calculations with the partition function. Finally, we use $u_r(\beta)$ as an expansion parameter. Due to the Schur lemma, the matrix elements D_r^{ij} of the representation yields

$$\int \mathrm{d}U \chi_r^*(U)\chi_s(U) = \delta_{rs}. \tag{3.10}$$

Moreover, we have

$$\int \mathrm{d}U \chi_r(VU)\chi_s(WU^{-1}) = \frac{1}{\mathrm{d}_r}\delta_{rs}\chi_r(VW), \tag{3.11}$$

which has a simple graphic representation

$$\int \mathrm{d}U \; V \; \boxed{}^{U} \; W \;=\; \frac{1}{d_r} \; V \; \boxed{} \; W\,. \tag{3.12}$$

It is straightforward to see that the lowest order character expansion coefficient associates to the fundamental representation, and given by $u(\beta) = u_f(\beta) = \beta/18 + \ldots$. It should be mentioned that unlike the case of SU(3), for the U(1) and SU(2) pure gauge theory one can compute the coefficients of the character expansion in a closed-form by the usage of Bessel functions [78]. In practice, the character coefficients shall be smaller than 1, and for that reason, it is convenient to use them as expansion parameters.

We can start our derivation for the effective theory of pure gauge theory with the character expansion at hand[1]. The main idea of constructing an effective theory from first principles

[1]We consider here the pure gauge contribution only, while the fermion contributions will be introduced into

is integrating out some degrees of freedom of the system, and here they are the spatial link variables. The effective action is defined as

$$e^{-S_{G,\text{eff}}} = \int \mathscr{D}U_i \prod_P \left(1 + \sum_{\mathrm{r}\neq 0} \mathrm{d}_r u_r(\beta)\chi_r(U_P)\right). \tag{3.13}$$

Here $\mathscr{D}U_i$ denotes the spatial links configurations. Since the leading contribution is obtained by neglecting spatial plaquettes, i.e. there is no contribution of temporal links. Thus, there are only chains of plaquettes looping through the temporal boundary at the leading order. After integrating out spatial links we obtain two disconnected loops located at the nearest neighbor of spatial lattice sites

$$e^{-S_{G,\text{eff}}} = 1 + \sum_{\langle \vec{n}_1, \vec{n}_2 \rangle} u^{N_t} \left(L_{\vec{n}_1} L^*_{\vec{n}_2} + L^*_{\vec{n}_1} L_{\vec{n}_2}\right) + \mathcal{O}(u^{N_t+4}). \tag{3.14}$$

Here $L_{\vec{n}}$ is a local Polyakop loop

$$L_{\vec{n}} = \mathrm{tr}\, W_{\vec{n}} = \mathrm{tr} \prod_{t=0}^{N_t-1} U_0(\vec{n}, t).$$

It turns out that including several types of higher-order graphs such as larger number of loops, Polyakov loops at distances larger than one and Polyakov loops in higher dimensional representations, we end up with the logarithm expression of the effective theory which improves over the old one [27]. We note in particular that the derivation of the improved effective pure gauge theory for the SU(2) and SU(3) gauge group are analogous, however, since the SU(3) gauge group also involves an anti-fundamental representation, which leads to an inclusion of a complex conjugate Polyakov loop L^* to keep the effective pure gauge action real.

We will work on the effective theory of one-coupling - the nearest-neighbor effective coupling λ_1. Based on Svetitsky and Yaffe conjecture [79], this effective theory describes the short-range Polyakov interactions which are the dominant contributions and the relevant terms for the phase transition. The case of effective couplings at larger distances as well as of higher representations are discussed in [27, 80]. The one-coupling partition function reads

$$Z_{G,\text{eff}} = \int \mathscr{D}W \prod_{\langle \vec{n}_1, \vec{n}_2 \rangle} \left[1 + \lambda_1(u, N_t)(L_{\vec{n}_1} L^*_{\vec{n}_2} + L^*_{\vec{n}_1} L_{\vec{n}_2})\right], \tag{3.15}$$

where the improved effective gauge action is given by

$$S_{G,\text{eff}} = -\sum_{\langle \vec{n}_1, \vec{n}_2 \rangle} \log\left[1 + \lambda_1(u, N_t)(L_{\vec{n}_1} L^*_{\vec{n}_2} + L^*_{\vec{n}_1} L_{\vec{n}_2})\right]. \tag{3.16}$$

Here we replaced the integration over all temporal links with an integration over the Wilson line variables W

$$\mathscr{D}W = \prod_{\vec{n}} \mathrm{d}W_{\vec{n}} = \prod_{\vec{n}} \prod_{t=0}^{N_t-1} \mathrm{d}U_0(\vec{n}, t). \tag{3.17}$$

---

our effective theory later.

The effective coupling λ_1 with corrections of attached plaquettes decorations is obtained for $N_t \geqslant 4$ as

$$\begin{aligned}\lambda_1(4,u) &= u^4 \exp\Bigg[4\Bigg(4u^4 + 12u^5 - 14u^6 - 36u^7 \\ &\qquad + \frac{295}{2}u^8 + \frac{1851}{10}u^9 + \frac{1035317}{5120}u^{10}\Bigg)\Bigg], \\ \lambda_1(N_t \geqslant 6,u) &= u^{N_t} \exp\Bigg[N_t\Bigg(4u^4 + 12u^5 - 14u^6 - 36u^7 \\ &\qquad + \frac{295}{2}u^8 + \frac{1851}{10}u^9 + \frac{1055797}{5120}u^{10}\Bigg)\Bigg]. \end{aligned} \tag{3.18}$$

3.3 The hopping parameter expansion

In general, it is expensive to evaluate the fermion determinant even at zero chemical potential. The inefficiency lies in the step of computing inversion of the Wilson-Dirac operator. For heavy quarks, there is an expansion scheme that makes use of the simplification of the Wilson-Dirac operator, i.e. the operator takes a close to block diagonal form. In this section, we dive into the derivation of an effective theory for heavy quarks by using the so-called hopping expansion [29].

We have introduced the hopping parameter in section 2.2.3. For the sake of simplicity, let us first consider the case of one flavor only, the introduction of multiple fermion flavors is straightforward and will be shown later. The Wilson-Dirac operator for $N_f = 1$ in the hopping parameter representation is refactored to be

$$D_{nm} = \delta_{nm} - \kappa H_{nm}, \qquad \kappa = \frac{1}{2am+8}. \tag{3.19}$$

Again, κ is called the hopping parameter[2] and H denotes the hopping matrix. The hopping matrix for Wilson fermions is

$$H_{nm} = \sum_{\nu=0}^{3}\left[e^{a\mu\delta_{\nu 0}}(1+\gamma_\nu)U_\nu(n)\delta_{n,m-\hat{\nu}} + e^{-a\mu\delta_{\nu 0}}(1-\gamma_\nu)U_{-\nu}(n)\delta_{n,m+\hat{\nu}}\right], \tag{3.20}$$

where we can write $U_{-\nu}(n) = U_\nu^\dagger(n-\hat{\nu})$. The crucial point of the hopping expansion is that for large quark mass κ becomes small, and it enables us to perform calculations in terms of series expansions. The fermion propagator can be expanded with the geometric series

$$D^{-1} = (1-\kappa H)^{-1} = \sum_{i=0}^{\infty}\kappa^i H^i. \tag{3.21}$$

The series converges for $\kappa||H|| < 1$. The norm of the hopping term obeys $||H|| \leqslant 8$, which means that the series converges if $\kappa < 1/8$.

[2]From now on, we drop the index b of the bare quark mass, but the reader should keep in mind that κ is related to the bare quark mass as given in the formula (2.27).

3.3.1 Static quark determinant

Now we turn to the derivation of the static quark determinant. This determinant describes static quarks - infinite heavy quarks and can be computed exactly. All corrections to this limit are given in the so-called kinetic determinant. It is convenient to split the quark matrix into temporal and spatial hops with positive and negative directions, this way we can keep the complete dependence on chemical potential. The Wilson-Dirac matrix can be rewritten as

$$D = 1 - T - S = 1 - T^{+} - T^{-} - S^{+} - S^{-}. \tag{3.22}$$

The static determinant is obtained by neglecting the spatial contributions,

$$\det[D_{\text{stat}}] = \det[1 - T] = \det[1 - T^{+} - T^{-}], \tag{3.23}$$

where T^{+} and T^{-} are explicitly given by

$$T^{+} = \kappa e^{a\mu}(1 + \gamma_0)U_0(n_1)\delta_{n_1,n_2-\hat{0}}, \tag{3.24}$$

$$T^{-} = \kappa e^{-a\mu}(1 - \gamma_0)U_0^{\dagger}(n_1 - \hat{0})\delta_{n_1,n_2-\hat{0}}. \tag{3.25}$$

Here the static quark propagator D_{stat}^{-1} propagates only along the temporal direction. There is no mixed $T^{+}T^{-}$ terms due the no-backtracking constraint $(1 - \gamma_\mu)(1 + \gamma_\mu) = 0$, therefore we can factorize further the static quark determinant into two separated parts

$$\det[D_{\text{stat}}] = \det[1 - T^{+}]\det[1 - T^{-}]. \tag{3.26}$$

Evaluating the space and spin determinant, and taking into account all windings of Wilson lines around the temporal direction and thus the full fugacity dependence leads to the final expression for the static determinant [28, 81]

$$\det[D_{\text{stat}}] = \prod_{\vec{n}}[1 + h_1 L_{\vec{n}} + h_1^2 L_{\vec{n}}^{*} + h_1^3]^2[1 + \bar{h}_1 L_{\vec{n}}^{*} + \bar{h}_1^2 L_{\vec{n}} + \bar{h}_1^3]^2. \tag{3.27}$$

To leading order in the combined expansions, the coefficients are the heavy quark fugacities,

$$h_1(\mu) = (2\kappa e^{a\mu})^{N_t} = e^{\frac{\mu - m}{T}} = \bar{h}_1(-\mu). \tag{3.28}$$

In the strong coupling limit $\beta = 0$, the constituent quark mass is given by $am = -\log(2\kappa)$ [82]. Let us define a leading order term of the effective fermion action associated with the static quark determinant

$$S_0 = -\log\det[D_{\text{stat}}]. \tag{3.29}$$

It is necessary to define the respective terms of the effective action now because we will explicitly evaluate the effective theory for different orders to observe its improvement.

3.3.2 Static quark propagator

The static quark propagator is computed using either the Cayley-Hamilton theorem for calculating the inverse of a matrix directly or expansion in κ and then resume it to all orders. Our goal is to compute the kinetic quark determinant, and a necessary intermediate step is to

compute the static quark propagator. The detailed calculation can be found in [81, 83]. The full static propagator takes the form

$$(D^{-1}_{\text{stat}})_{n_1 n_2} = \delta_{\vec{n}_1\vec{n}_2} \triangle_{t_{n_1}t_{n_2}}(\vec{n_1}) = \delta_{\vec{n}_1\vec{n}_2}\left(\delta_{t_{n_1}t_{n_2}} + \Gamma^0_+ B^+_{t_{n_1}t_{n_2}} + \Gamma^0_- B^-_{t_{n_1}t_{n_2}}\right), \tag{3.30}$$

where we use the following conventions for the gamma matrices

$$\Gamma^0_\pm = \frac{1}{2}(1 \pm \gamma^0), \qquad \Gamma^i_\pm = 1 \pm \gamma^i, \tag{3.31}$$

and the components B^+ and B^- read

$$B^+_{t_{n_1}t_{n_2}} = \frac{h_1 W}{1 + h_1 W}\delta_{t_{n_1}t_{n_2}} + (2e^{a\mu}\kappa)^{t_{n_1}-t_{n_2}}\frac{U_0(t_{n_1} \to t_{n_2})}{1 + h_1 W}(\theta_{t_{n_1}t_{n_2}} - h_1 W \theta_{t_{n_2}t_{n_1}}), \tag{3.32}$$

$$B^-_{t_{n_1}t_{n_2}} = \frac{\bar{h}_1 W^\dagger}{1 + \bar{h}_1 W^\dagger}\delta_{t_{n_1}t_{n_2}} + (2e^{-a\mu}\kappa)^{t_{n_2}-t_{n_1}}\frac{U_0(t_{n_1} \to t_{n_2})}{1 + \bar{h}_1 W^\dagger}(\theta_{t_{n_1}t_{n_2}} - \bar{h}_1 W^\dagger \theta_{t_{n_2}t_{n_1}}). \tag{3.33}$$

Here θ is the Heaviside step function, and $U_0(t_{n_1} \to t_{n_2})$ is called the gauge transporter which is defined to be

$$U_0(t_n \to t_m) = \begin{cases} \prod_{t=t_{n_1}}^{t_{n_2}-1} U_0(t) & : t_{n_1} < t_{n_2} \\ \prod_{t=t_{n_2}}^{t_{n_1}-1} U_0(t) & : t_{n_1} \geqslant t_{n_2} \end{cases} \tag{3.34}$$

3.3.3 Kinetic quark determinant

With the static quark propagator we can proceed with the derivation of the kinetic quark determinant. First we perform a factorization for the determinant of (3.22) as

$$\begin{aligned} \det[D] &= \det(1 - T - S) = \det(1 - T)\det(1 - \frac{S}{1 - T}) \\ &= \det(1 - T)\det(1 - P - M), \end{aligned} \tag{3.35}$$

where P and M are given in the form

$$P = \sum_{i=1}^{3} P_i = \frac{\kappa}{1 - T}\sum_{i=1}^{3} S^+_i, \tag{3.36}$$

$$M = \sum_{i=1}^{3} M_i = \frac{\kappa}{1 - T}\sum_{i=1}^{3} S^-_i. \tag{3.37}$$

The P and M are called the forward and backward hopping operators representing a single lattice hop in positive and negative spatial directions, respectively, while allowing arbitrary movement in the temporal direction, including all windings. Substituting the eqn. (3.30) into P and M gives their explicit form

$$P_{n_1 n_2} = \kappa \sum_i P_{i n_1 n_2} = \kappa \triangle_{t_{n_1}t_{n_2}}(\vec{n}_1)\sum_i \Gamma^i_+ U_i(t_{n_2}, \vec{n}_1)\delta_{\vec{n}_1 + \hat{i}\vec{n}_2}, \tag{3.38}$$

$$M_{n_1 n_2} = \kappa \sum_j M_{j n_1 n_2} = \kappa \triangle_{t_{n_1}t_{n_2}}(\vec{n}_1)\sum_j \Gamma^j_- U^\dagger_j(t_{n_2}, \vec{n}_1 - \hat{j})\delta_{\vec{n}_1 - \hat{j}\vec{n}_2}. \tag{3.39}$$

The derivation can be simplified by using an approach of graph representations. Let us represent the building blocks contributed to kinetic diagrams, where the temporal, forward and backward spatial hoppings are represented by lines encoded with colors as follows

$$\triangle_{t_{n_1} t_{n_2}}(\vec{n_1}) \tag{3.40}$$

$$\Gamma^i_+ U_i(t_{n_2}, \vec{n}_1)\delta_{\vec{n}_1+\hat{i}\vec{n}_2} \tag{3.41}$$

$$\Gamma^i_- U^\dagger_i(t_{n_2}, \vec{n}_1 - \hat{i})\delta_{\vec{n}_1-\hat{i}\vec{n}_2} \tag{3.42}$$

From (3.35) we can see that the factorization step is useful, since we can expand further the kinetic quark determinant

$$\det[D_{\text{kin}}] = \det(1 - P - M) = \exp\left(-\sum_{n=1}^{\infty} \text{tr}(P + M)^n\right). \tag{3.43}$$

It is clear that only closed loops have non-vanishing contributions, so we need an equal number of positive and negative hops (neglecting finite size corrections). The expansion up to order $n = 6$ reads

$$\begin{aligned}\det[D_{\text{kin}}] = \exp\Bigg\{-\Bigg[&\text{tr}\, PM + \text{tr}\, PPMM + \frac{1}{2}\,\text{tr}\, PMPM + \text{tr}\, PPPMMM \\ &+ \text{tr}\, PPMPMM + \text{tr}\, PPMMPM + \frac{1}{3}\,\text{tr}\, PMPMPM + \mathcal{O}(\kappa^8)\Bigg]\Bigg\}.\end{aligned} \tag{3.44}$$

Here it is convenient to work with the effective theory associated with the order in the hopping parameter κ. We denote Z_i for $i \in \{2, 4, 6\}$ to be the effective theory of orders $2, 4$ and 6 in the hopping parameter κ, respectively. Let us demonstrate how to derive the $\mathcal{O}(\kappa^2)$ effective theory Z_2 in full detail, and its graph representation is also provided. For the effective theory of higher orders Z_4 and Z_6, their detailed expression after the complete evaluation is simply too long to be printed here, therefore we will present only a few particular terms of these orders, while the rest is given in terms of graph representations. We prefer the reader to [29, 81] for more details of how to perform the conversion of the $\mathcal{O}(\kappa^4)$ effective action into expressions that depend solely on the Polyakov loops.

As shown in (3.2), the effective theory is given by integration over the spatial links, therefore for the calculation of the spatial gauge integrals to be possible it is required to expand the exponential. The expanded kinetic determinant $\det[D_{\text{kin}}]$ reads

$$\begin{aligned}\det[D_{\text{kin}}] = 1 - \text{tr}\, PM &- \left(\text{tr}\, PPMM + \frac{1}{2}\,\text{tr}\, PMPM - \frac{1}{2}\,\text{tr}\, PM\,\text{tr}\, PM\right) \\ &- \Bigg(\text{tr}\, PPPMMM + \text{tr}\, PPMPMM + \text{tr}\, PPMMPM + \frac{1}{3}\,\text{tr}\, PMPMPM \\ &\quad - \text{tr}\, PM\,\text{tr}\, PPMM - \frac{1}{2}\,\text{tr}\, PM\,\text{tr}\, PMPM + \frac{1}{6}\,\text{tr}\, PM\,\text{tr}\, PM\,\text{tr}\, PM\Bigg).\end{aligned} \tag{3.45}$$

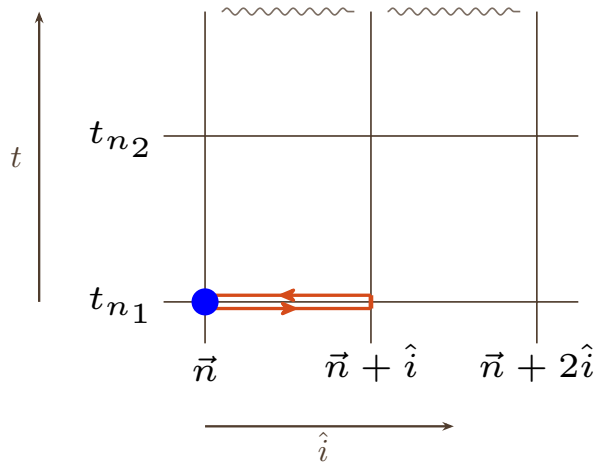

Figure 3.1: Contribution from the lowest order spatial hopping expansion K_2 in terms of a graph representation.

Let us focus on the evaluation of Z_2. The leading order of the kinetic determinant is defined to be

$$\int \mathscr{D}U_\mu \det[D_{\text{stat}}] e^{-\operatorname{tr} PM} = \int \mathscr{D}U_\mu \det[D_{\text{stat}}](1 - \operatorname{tr} PM + \mathcal{O}(\kappa^4)). \tag{3.46}$$

The static quark determinant $\det[D_{\text{stat}}]$ only depends on the temporal link variables, which can be factored out from the spatial integral. Substituting (3.38) and (3.39) into (3.46) gives the following integral

$$\begin{aligned} Z_2 = \int \mathscr{D}U_i \operatorname{tr} PM &= \kappa^2 \int \mathscr{D}U_i \sum_{n_1,n_2} \sum_{k,l} \operatorname{tr}\left[P_{kn_1n_2} M_{ln_2n_1}\right], \\ &= \kappa^2 \int \mathscr{D}U_i \sum_{k,l,\vec{n}} \operatorname{tr}\Big[\triangle_{t_{n_1}t_{n_2}}(\vec{n}) \Gamma^k_+ U_k(t_{n_2},\vec{n}) \\ &\qquad \triangle_{t_{n_2}t_{n_1}}(\vec{n}+\hat{k}) \Gamma^l_- U^\dagger_l(t_{n_1},\vec{n}+\hat{k}-\hat{l}) \delta_{\vec{n},\vec{n}+\hat{k}-\hat{l}} \Big]. \end{aligned} \tag{3.47}$$

This integral is non-vanishing only if the two links overlap due to the gauge integral selection rule, i.e. $k = l$ and $t_{n_1} = t_{n_2}$. Thus, we can rewrite the integral (3.47) as

$$\int \mathscr{D}U_i \operatorname{tr} PM = \kappa^2 \int \mathscr{D}U_i \sum_{k,t_n,\vec{n}} \operatorname{tr}\Big[\triangle_{t_nt_n}(\vec{n}) \Gamma^k_+ U_k(t_n,\vec{n}) \triangle_{t_nt_n}(\vec{n}+\hat{k}) \Gamma^k_- U^\dagger_k(t_n,\vec{n}) \Big]. \tag{3.48}$$

We emphasize that the expression (3.48) can be represented graphically. Its corresponding graph-representation is simply given in fig. 3.1. Next, the evaluation of the trace can be divided into its three remaining indices; spin, color and temporal. First, the components $B^\pm$ of the static propagator given in (3.32) and (3.33) take a very simple form for $t_{n_1} = t_{n_2}$

$$B^+_{t_nt_n}(\vec{n}) = \frac{h_1 W_{\vec{n}}}{1 + h_1 W_{\vec{n}}}, \qquad B^-_{t_nt_n}(\vec{n}) = \frac{\bar{h}_1 W^\dagger_{\vec{n}}}{1 + \bar{h}_1 W^\dagger_{\vec{n}}}. \tag{3.49}$$

They are simply picked out from the diagonal pieces of $B^{\pm}$. The spin indices are unrelated to the group integral and can be evaluated immediately. Inserting the expression for D^{-1}_{stat} and computing gamma matrices we get

$$\begin{aligned}\left(1+\Gamma^0_+ B^+_{\vec{n}}+\Gamma^0_- B^-_{\vec{n}}\right)\Gamma^k_+\left(1+\Gamma^0_+ B^+_{\vec{n}+\hat{k}}+\Gamma^0_- B^-_{\vec{n}+\hat{k}}\right)\Gamma^k_- \\ = 2(B^+_{\vec{n}}-B^-_{\vec{n}})(B^+_{\vec{n}+\hat{k}}-B^-_{\vec{n}+\hat{k}}).\end{aligned} \tag{3.50}$$

Substituting (3.50) back into eqn. (3.48) we obtain

$$\int \mathscr{D}U_i \,\mathrm{tr}\, PM = 2\kappa^2 N_t \,\mathrm{tr}\sum_{\vec{n},k}(B^+_{\vec{n}}-B^-_{\vec{n}})_{ab}(B^+_{\vec{n}+\hat{k}}-B^-_{\vec{n}+\hat{k}})_{cd}\int \mathrm{d}U U_{bc}U^\dagger_{da}. \tag{3.51}$$

Summing over the time-slice gives us a factor N_t. Furthermore, note that we sum over the color indices, carry out the unoccupied link integrals and rename the spatial links to U. We now can use the result of the group integral given in (A.1)

$$\begin{aligned}\int \mathscr{D}U_i \,\mathrm{tr}\, PM &= \frac{2\kappa^2 N_t}{N_c}\,\mathrm{tr}\sum_{\vec{n},k}(B^+_{\vec{n}}-B^-_{\vec{n}})_{ab}(B^+_{\vec{n}+\hat{k}}-B^-_{\vec{n}+\hat{k}})_{da}\delta_{ba}\delta_{cd}, \\ &= \frac{2\kappa^2 N_t}{N_c}\sum_{\vec{n},k}\mathrm{tr}(B^+_{\vec{n}}-B^-_{\vec{n}})\,\mathrm{tr}(B^+_{\vec{n}+\hat{k}}-B^-_{\vec{n}+\hat{k}}).\end{aligned} \tag{3.52}$$

Inserting (3.49) into (3.52) we obtain the final expression for the kinetic determinant to leading order

$$\int \mathscr{D}U_i \,\mathrm{tr}\, PM = 2\frac{\kappa^2 N_t}{N_c}\sum_{\langle\vec{n}_1,\vec{n}_2\rangle}\mathrm{tr}\left(\frac{h_1 W_{\vec{n}_1}}{1+h_1 W_{\vec{n}_1}}-\frac{\bar{h}_1 W^\dagger_{\vec{n}_1}}{1+\bar{h}_1 W^\dagger_{\vec{n}_1}}\right)\mathrm{tr}\left(\frac{h_1 W_{\vec{n}_2}}{1+h_1 W_{\vec{n}_2}}-\frac{\bar{h}_1 W^\dagger_{\vec{n}_2}}{1+\bar{h}_1 W^\dagger_{\vec{n}_2}}\right) \tag{3.53}$$

Analyzing this expression we see that since there is no color mixing between sites, the lowest order contribution to the spatial hopping expansion of the kinetic determinant is simply a nearest-neighbor interaction between Polyakov loop-dependent objects. We will see later that it is useful to introduce the shorthand notation

$$W_{nm}(\vec{n}) = \mathrm{tr}\,\frac{(h_1 W_{\vec{n}})^m}{(1+h_1 W_{\vec{n}})^n}, \qquad \bar{W}_{nm}(\vec{n}) = \mathrm{tr}\,\frac{(\bar{h}_1 W^\dagger_{\vec{n}})^m}{(1+\bar{h}_1 W^\dagger_{\vec{n}})^n}. \tag{3.54}$$

Finally the lowest order spatial hopping contribution to the effective action can be written as

$$e^{S_{2,\text{eff}}} = 1-\frac{\kappa^2 N_t}{N_c}\sum_{\langle\vec{n},\vec{m}\rangle}\left(W_{11}(\vec{n})-\bar{W}_{11}(\vec{n})\right)\left(W_{11}(\vec{m})-\bar{W}_{11}(\vec{m})\right)+\mathcal{O}(\kappa^4). \tag{3.55}$$

New terms both in the nearest-neighbor contribution as well as non-local terms spanning further on the lattice will appear in the next-to-leading order in κ.

Since the $\mathcal{O}(\kappa^4)$ effective lattice theory has been computed many times before, for example see [29, 30, 81], so we will not cover its detailed computation, and only give the corresponding graph representations instead. Starting with the expanded kinetic determinant (3.45), we

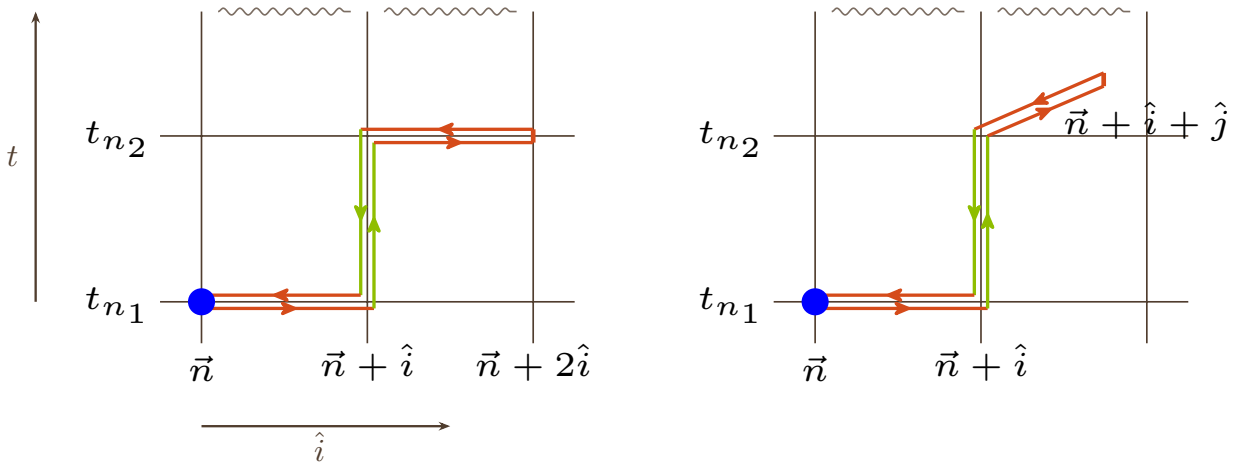

Figure 3.2: The graphic contributions associated with the term tr $PPMM$.

denote the κ^4-contributions as follows

$$Z_4 = Z_4^1 + Z_4^2 + Z_4^3 = \int \mathscr{D}U_i \left(\operatorname{tr} PPMM + \frac{1}{2} \operatorname{tr} PMPM - \frac{1}{2} \operatorname{tr} PM \operatorname{tr} PM \right). \tag{3.56}$$

The graphs associated with Z_4^1 are given in fig. 3.2. Let us briefly describe those graphs: The blue point is an arbitrary point on the lattice and serves as our starting point at which the static propagator does not move, corresponding to a static propagator of the form $\triangle_{t_{n_1} t_{n_1}}$. The red line represents a spatial hop in a lattice unit, for example, from $\vec{n}$ to $\vec{n}+\hat{i}$, while the green line represents a temporal hop from t_{n_1} to t_{n_2}. In particular, the graph on the right involves hoppings in two different spatial directions i, j where $i \neq j$. It should be pointed out that to ensure a non-vanishing contribution these graphs need to form a closed loop, which they do as one can see in fig. 3.2 where the last spatial hop ends at the blue point.

3.4 The $\mathcal{O}(\kappa^6)$ effective action

We now turn to the derivation of the $\mathcal{O}(\kappa^6)$ effective action. We demonstrate only one term in the κ^6-contribution of the effective action due to the fact that the total expression is too long to write down. Similar to the κ^4-contributions, we can define the κ^6-contributions from (3.45) as follows

$$Z_6 = Z_6^1 + Z_6^2 + Z_6^3 + \frac{1}{3} Z_6^4 - Z_6^5 - \frac{1}{2} Z_6^6 + \frac{1}{6} Z_6^7. \tag{3.57}$$

Each term Z_6^i contains several sub-terms which correspond to their different spatial and temporal occupations. Thus, we present only an explicit derivation for the Z_6^1 term, and will provide the full expressions in Appendix D. The computations of Z_6^1 can be carried out as follows

$$\begin{aligned} Z_6^1 &= \int \mathscr{D}U_i \operatorname{tr} PPPMMM \\ &= \int \mathscr{D}U_i \sum_{i_1 \ldots j_3} \sum_{n_1 \ldots n_6} \operatorname{tr} P_{i_1 n_1 n_2} P_{i_2 n_2 n_3} P_{i_3 n_3 n_4} M_{j_1 n_4 n_5} M_{j_2 n_5 n_6} M_{j_3 n_6 n_1}. \end{aligned}$$

We then substitute the spatial forward and backward hopping operators defined in (3.38) and (3.39), and obtain

$$
\begin{aligned}
Z_6^1 = \int \mathscr{D}U_i \sum_{i_1 \ldots j_3} \sum_{\vec{n}} \mathrm{tr} \Bigg[& \triangle_{t_{n_1} t_{n_2}}(\vec{n}) \Gamma_+^{i_1} U_{i_1}(t_{n_2}, \vec{n}) \\
& \triangle_{t_{n_2} t_{n_3}}(\vec{n} + \hat{i}_1) \Gamma_+^{i_2} U_{i_2}(t_{n_3}, \vec{n} + \hat{i}_1) \\
& \triangle_{t_{n_3} t_{n_4}}(\vec{n} + \hat{i}_1 + \hat{i}_2) \Gamma_+^{i_3} U_{i_3}(t_{n_4}, \vec{n} + \hat{i}_1 + \hat{i}_2) \\
& \triangle_{t_{n_4} t_{n_5}}(\vec{n} + \hat{i}_1 + \hat{i}_2 + \hat{i}_3) \Gamma_-^{j_1} U_{j_1}^\dagger(t_{n_5}, \vec{n} + \hat{i}_1 + \hat{i}_2 + \hat{i}_3 - \hat{j}_1) \\
& \triangle_{t_{n_5} t_{n_6}}(\vec{n} + \hat{i}_1 + \hat{i}_2 + \hat{i}_3 - \hat{j}_1) \Gamma_-^{j_2} U_{j_2}^\dagger(t_{n_6}, \vec{n} + \hat{i}_1 + \hat{i}_2 + \hat{i}_3 - \hat{j}_1 - \hat{j}_2) \\
& \triangle_{t_{n_6} t_{n_1}}(\vec{n} + \hat{i}_1 + \hat{i}_2 + \hat{i}_3 - \hat{j}_1 - \hat{j}_2) \Gamma_-^{j_3} U_{j_3}^\dagger(t_{n_1}, \vec{n}) \Bigg] \delta_{0 i_1 + i_2 + i_3 - j_1 - j_2 - j_3}
\end{aligned}
$$

For the delta function $\delta_{0 i_1 + i_2 + i_3 - j_1 - j_2 - j_3}$ to be non-zero, we have 16 combinations of the indices i's and j's

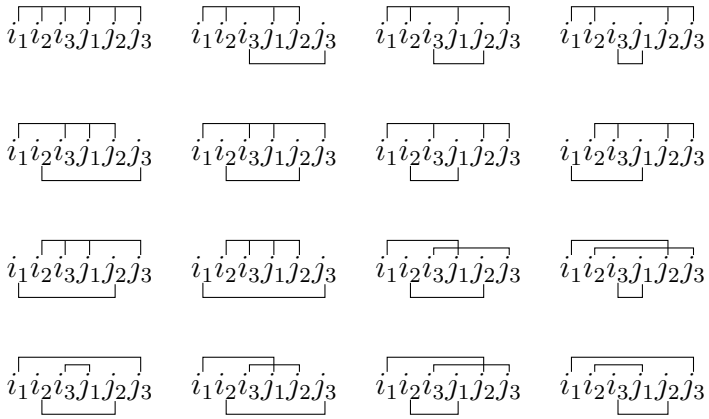

Due to the constraints of group integrals on spatial links $U_i(t, \vec{n})$, for example the second combination $i_1 = i_2 = j_1 = j_2 \neq i_3 = j_3$ is not allowed, because for $i_3 = j_3 = j$ the spatial integral performed on $U_j(\vec{n} + 2\hat{i}) U_j^\dagger(\vec{n})$ vanishes due to the difference of their spatial position. Thus, only 5 contractions are non-vanishing

a. $i_1 = i_2 = i_3 = j_1 = j_2 = j_3$,
b. $i_1 = i_2 = j_2 = j_3 \neq i_3 = j_1$,
c. $i_1 = i_3 = j_1 = j_3 \neq i_2 = j_2$,
d. $i_1 = j_3 \neq i_2 = i_3 = j_1 = j_2$,
e. $i_1 = j_3 \neq i_2 = j_2 \neq i_3 = j_3$.

The first non-vanishing term corresponding to the case $i = i_1 = i_2 = i_3 = j_1 = j_2 = j_3$ which

is denoted as Z_6^{1a}, and can be computed as follows

$$Z_6^{1a} = \int \mathscr{D}U_i \sum_{i,t_n,\vec{n}} \mathrm{tr}\Bigg[\triangle_{t_{n_1}t_{n_2}}(\vec{n})\Gamma^i_+ U_i(t_{n_2},\vec{n}) \cdot \triangle_{t_{n_2}t_{n_3}}(\vec{n}+\hat{i})\Gamma^i_+ U_i(t_{n_3},\vec{n}+\hat{i}) \\ \triangle_{t_{n_3}t_{n_4}}(\vec{n}+2\hat{i})\Gamma^i_+ U_i(t_{n_4},\vec{n}+2\hat{i}) \cdot \triangle_{t_{n_4}t_{n_5}}(\vec{n}+3\hat{i})\Gamma^i_- U_i^\dagger(t_{n_5},\vec{n}+2\hat{i}) \\ \triangle_{t_{n_5}t_{n_6}}(\vec{n}+2\hat{i})\Gamma^i_- U_i^\dagger(t_{n_6},\vec{n}+\hat{i}) \cdot \triangle_{t_{n_6}t_{n_1}}(\vec{n}+\hat{i})\Gamma^i_- U_i^\dagger(t_{n_1},\vec{n})\Bigg]. \quad (3.58)$$

Again, for this integral to be non-vanishing, based on constraints of the group integral we obtain further conditions on the temporal extent

$$\delta_{t_{n_1}t_{n_2}}, \qquad \delta_{t_{n_3}t_{n_6}}, \qquad \delta_{t_{n_4}t_{n_5}}. \quad (3.59)$$

After redefining t_n, then K_6^{1a} takes the form

$$Z_6^{1a} = \int \mathscr{D}U_i \sum_{i,t_n,\vec{n}} \mathrm{tr}\Bigg[\triangle_{t_{n_1}t_{n_1}}(\vec{n})\Gamma^i_+ U_i(t_{n_1},\vec{n}) \cdot \triangle_{t_{n_1}t_{n_2}}(\vec{n}+\hat{i})\Gamma^i_+ U_i(t_{n_2},\vec{n}+\hat{i}) \\ \triangle_{t_{n_2}t_{n_3}}(\vec{n}+2\hat{i})\Gamma^i_+ U_i(t_{n_3},\vec{n}+2\hat{i}) \cdot \triangle_{t_{n_3}t_{n_3}}(\vec{n}+3\hat{i})\Gamma^i_- U_i^\dagger(t_{n_3},\vec{n}+2\hat{i}) \\ \triangle_{t_{n_3}t_{n_2}}(\vec{n}+2\hat{i})\Gamma^i_- U_i^\dagger(t_{n_2},\vec{n}+\hat{i}) \cdot \triangle_{t_{n_2}t_{n_1}}(\vec{n}+\hat{i})\Gamma^i_- U_i^\dagger(t_{n_1},\vec{n})\Bigg]. \quad (3.60)$$

It is the same for the effective theory at order $\mathcal{O}(\kappa^6)$, that each non-vanishing term has to form a closed loop, which one can observe in eqn. (3.60). This is basically done because the spin indices are unrelated to the group integral and can be evaluated immediately by using (3.31). While we have three pairs of spatial link integrals as in eqn. (A.1). We note that at this stage if we re-express terms of κ^6-contributions in terms of eqn. (3.54), then implementing the effective theory will be very challenging, even if one considers only the nearest-neighbor interaction terms of the $\mathcal{O}(\kappa^6)$ effective theory. The readers will see that the efficiency of our code decreases exponentially with the number of terms in the effective theory already at order $\mathcal{O}(\kappa^4)$. Fortunately, with the direct SU(3) link update we can just use the original expression of the static quark propagator (3.30) without re-expressing everything in terms of the Polyakov loop, and then take the trace afterward. We will get back to this point later in chapter 6.2.

The rest of this section dedicates to the graph representations of K_6^1 on the lattice, while the graph representation of $K_6^2, \ldots, K_6^7$ is again partly given in appendix D. With graph representation, one can easily convert it back to the analytic expression. Another advantage of the graph representation is that given a set of constraints higher orders of the effective theory can be achieved with the use of a computer, and the software that computes the effective theory in the limit of cold QCD [84] might serve as a starting point. In fig. 3.3, one can easily see how the eqn. (3.60) corresponds to this graph. The red bonds represent the spatial hopping in positive and negative directions, and the green ones represent the temporal hoppings. The graph starts at $(t_{n_1},\vec{n})$, propagate to $(t_{n_3},\vec{n}+3\hat{i})$ and finally travels back to $(t_{n_1},\vec{n})$, which forms a closed loop.

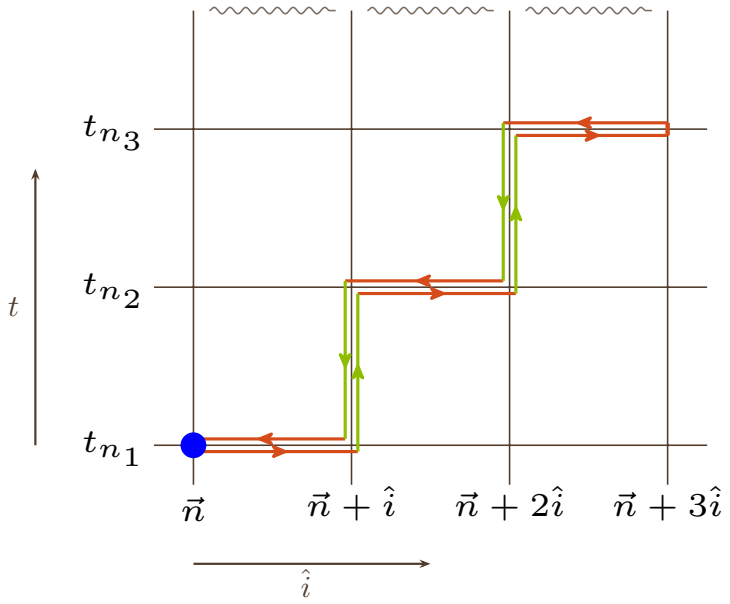

Figure 3.3: The graph representation of K_6^{1a}.

Let us briefly describe the interpretation of particles hopping between the lattice sites in terms of the kinetic quark determinant. The incoming and outgoing arrows at each lattice site simply represent composite states that locate at these sites. For example, in fig. 3.3 there is an incoming and an outgoing arrow at $(t_{n_1}, \vec{n})$, meaning that at this site we have a meson - a composite particle of an equal number of quarks and antiquarks. If there are two incoming and two outgoing lines at a lattice site, then we have two mesons. Finally, for $\mathcal{O}(\kappa^6)$ there is the case where a point possesses three incoming and three outgoing lines, indicating two possibilities of having three mesons or one baryon and one anti-baryon. Back to fig. 3.3, here we simply have three mesons exchange at $\vec{n}$, its nearest-neighbor and next-to-nearest-neighbor, as well as at different time slices. Later in Appendix D, one can see many combinations of particle exchanges that have to be considered, since we also have the trace with respect to color indices in the kinetic determinant.

3.5 Corrections

Until now, we have separated the pure gauge contributions from the fermion contributions, and there is no mix between the two. This is only possible in the limit of strong coupling. Outside this region, one needs to take into account mixed contributions that arise when we carry out the character and hopping parameter expansion simultaneously. A detailed computation of the corrections was also done in [29, 81], since this work does not expand on these results, so only the results which will be used in our simulations later, are listed.

3.5.1 Gauge corrections

The first corrections to consider are modifications to the static determinant, which are associated with the coupling h_1. They are constructed by attaching plaquettes to the Wilson line and then exponentiated by summing over multiple attached, disconnected plaquettes at different locations. The corrections of h_1 have been calculated to higher orders in the expansion

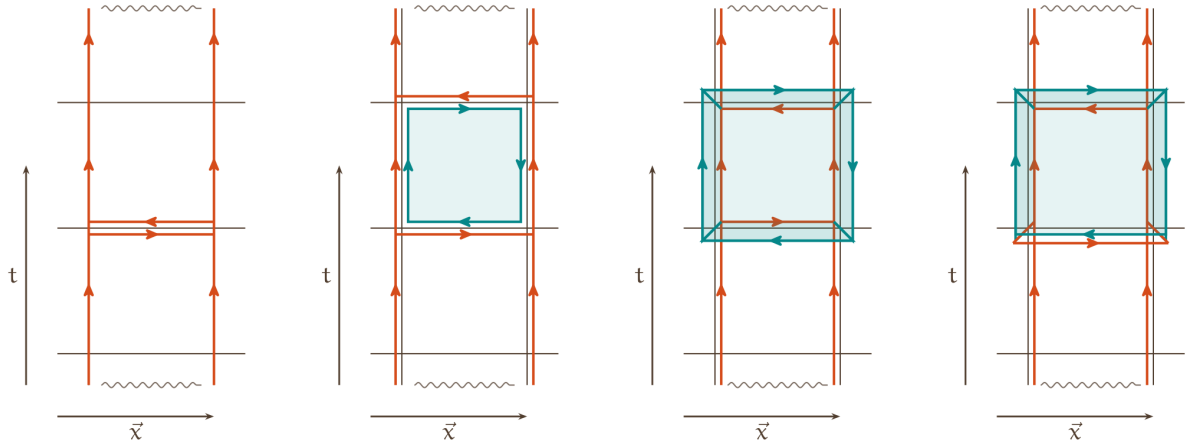

Figure 3.4: Diagrams associated with corrections to the effective coupling. Figure taken from [30].

parameters, κ, u [28, 85]

$$h_1(u,\kappa,N_t) = (2\kappa e^{a\mu})^{N_t} \exp\Bigg[6N_t\kappa^2 u\Bigg(\frac{1-u^{N_t-1}}{1-u} + 4u^4 - 12\kappa^2 + 9\kappa^2 u + 4\kappa^2 u^2 - 4\kappa^4\Bigg)\Bigg]. \tag{3.61}$$

Analogously, the nearest-neighbor coupling strength has a similar correction scheme where we shift spatial hoops and fill them with plaquettes. The diagrams are shown in fig. 3.4 and they give the following corrections to the effective coupling h_2 of the nearest neighbor interactions $S_{2,\text{eff}}$ [29]

$$h_2(u,\kappa,N_t) = \frac{\kappa^2 N_t}{N_c}\left(1 + 2\frac{u-u^{N_t}}{1-u} + 8u^5 + 16\kappa^2 u^4 + \mathcal{O}(\kappa^4 u^3)\right). \tag{3.62}$$

For the κ^4-contributions, the effective couplings including corrections for $N_t \geqslant 4$ are

$$h_3^1(u,\kappa,N_t) = \frac{N_t(N_t-1)\kappa^4}{N_c^2}\left[1 + \frac{8}{3}(u + u^2 + 4u^5 + 8\kappa^3 u^4)\right], \quad \text{for} \quad N_t = 4, \tag{3.63}$$

$$h_3^2(u,\kappa,N_t) = \frac{\kappa^4 N_t}{N_c^2}\left[1 + 4\frac{u-u^{N_t}}{1-u} + 16u^5 + 32\kappa^3 u^4\right], \tag{3.64}$$

$$h_3^3(u,\kappa,N_t) = \frac{\kappa^4 N_t^2}{N_c^2}\left[1 + 4\frac{(1-u^{N_t})(u-u^{N_t})}{(1-u)^2} + 16u^5 + 32\kappa^3 u^4\right], \tag{3.65}$$

$$h_3^4(u,\kappa,N_t) = \frac{\kappa^4 u N_t}{2N_c^3}\left[1 + 4u^4 + 16\kappa^3 u^4\right], \tag{3.66}$$

where $h_3^1, \cdots, h_3^4$ are effective couplings of S_4 coupled to κ^4-graphs with different gauge corrections. For more detail of how these couplings with corrections couple to their corresponding terms in S_4 as well as the study of their convergence, we refer the reader to [81].

3.5.2 Fermionic corrections

A different type of correction is fermion correction. The simplest fermion correction is one that comes from the possibility to replace any gauge plaquette with four quark hoppings. This can be done for every plaquette and results in a contribution that is then absorbed into a shift in the coupling β

$$\beta \to \beta + 48 N_f \kappa_f^4. \tag{3.67}$$

The next order contribution comes from replacing a pair of adjacent plaquettes by six fermion hops, we then obtain

$$\lambda(u, \kappa) = u^{N_t} + \frac{16 N_f N_t \kappa^6}{9u^2}. \tag{3.68}$$

Only adjacent plaquettes are considered, therefore this contribution cannot be absorbed into β. Higher-order corrections can be constructed analogously. It was shown in [81] that for $N_t = 4, N_f = 3$ the fermionic corrections to λ is suppressed at $\kappa < 0.1$ which is compatible to the region of our interest. Thus, the fermionic corrections can be neglected safely in our study.

3.6 Resummation and multiple flavors

Deriving the effective action requires an expansion on the exponential of the spatial hopping operator as in (3.46). However, it is advantageous for numerical and analytical studies to work with the exponential form, and the convergence of the effective action is also improved. To obtain the exponential form we perform a process of re-summing an infinite series of terms into a closed analytic expression. The resummation of the effective theory has been discussed quite often in previous works, for example see [29, 81, 83]. Here we present only the final resummed expression for the $\mathcal{O}(\kappa^2)$ effective theory, while the effective theory of higher orders are treated similarly,

$$S_{2,\text{eff}} = \frac{\kappa^2 N_t}{N_c} \sum_{\langle \vec{n}_1, \vec{n}_2 \rangle} \left(W_{11}(\vec{n}_1) - \bar{W}_{11}(\vec{n}_1) \right) \left(W_{11}(\vec{n}_2) - \bar{W}_{11}(\vec{n}_2) \right). \tag{3.69}$$

If we consider more than one fermion flavor, then changing the partition function is straightforward, since the different flavors decouple from each other due to the fact that there is no flavor changing process. The effective theory for N_f fermion flavors is

$$Z = \int \mathscr{D}U_\mu \prod_{f=1}^{N_f} \det[D_{f,\text{stat}}] \exp\left(- \sum_{f=1}^{N_f} \sum_{n=1}^{\infty} \frac{1}{n} \operatorname{tr}(P_f + M_f)^n \right). \tag{3.70}$$

The distinction between different flavors depends on their masses, and chemical potentials, i.e the flavor dependence enters through the parameter κ_f and μ_f. For degenerate flavors N_f is just a simple number

$$Z = \int \mathscr{D}U_\mu [\det[D_{\text{stat}}]]^{N_f} \exp\left(-N_f \sum_{f=1}^{N_f} \sum_{n=1}^{\infty} \frac{1}{n} \operatorname{tr}(P + M)^n \right). \tag{3.71}$$

It is easy to see that the N_f factor does not increase the complexity in our computation, and the correct pre-factors are determined simply by the number of fermion traces from which the term originates.

Chapter 4

Series expansion methods

> Most important part of doing physics is the knowledge of approximation.
>
> *by Lev Landau*

Series expansion methods have a long history and have passed many tests from experiments as well as soluble systems. These are sophisticated tools used to provide quantitative calculations in statistical mechanics. We devote this section to describing an analytic method called the high-temperature expansion which is then applied to evaluate the effective lattice theory of heavy quarks. The development of the high-temperature expansion for our effective theory is motivated by the fact that analytic calculations do not suffer from a fermion sign problem if we include finite baryon densities.

Classifying the contributions of higher-order terms is normally led to a description in terms of linear graphs. Thus, the starting point is to give a short introduction to graph theory. We shall then explain the high-temperature expansion and their characters in great detail[1]. This expansion itself and its realization on the computer with the usage of a powerful enumeration algorithm called the 'Pegs in Holes' is described. An important part of the analytic treatment is series analysis tools. They are needed to extract criticality for the asymptotic series obtained from expansion methods. In this work, two approximants used to estimate the critical endpoint on the phase boundary in the parameter space are Padé and Canterbury approximant.

4.1 Graph terminology

In this section, we discuss briefly the notion of graphs relevant for the high-temperature expansion and present examples and some results to reinforce the meaning of these concepts. A full and detailed introduction can be found in e.g. [35, 86, 87].

A linear graph G is a collection of p *vertices* which constitute the vertex set V together with edge set E of l *edges* between certain pairs of vertices. The graph is the abstract concept represented by two sets V and E. The *degree* of a vertex is the number of edges having a given vertex as an endpoint. For example, the graph in (4.1) is an undirected linear graph that has seven vertices, five edges, and three connected *components*. In this graph, there are four

[1]The definition of an alternative method called the linked cluster expansion and how it was successfully applied to the SU(3) spin model at real and imaginary chemical potential can be found in [31].

vertices of degree two, two of degree one, and one of degree zero.

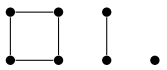

(4.1)

Two graphs G and G' which can be put into $1-1$ correspondence so that the points and connections correspond are termed *isomorphic* [35]. For example, see (4.2).

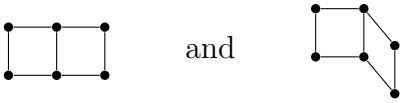

(4.2)

Graphs formed with p vertices and l edges can be classified into groups. The first two important groups are

1. *Separated graphs* which consist of graphs which have more than one component.
2. *Connected graphs* which consist of at least one edge between any two vertices and can be sub-divided further into
   - Stars S - multiply-connected graphs which are graphs with no *articulation point* or *cut-point* - a point where the graph could be cut into two or more separated graphs by cutting all lines going to this point, see (4.3).
   - Trees - graphs which are not multiply-connected, see (4.4).

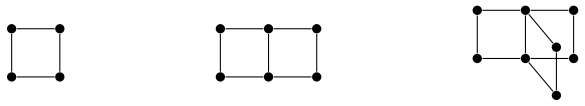

(4.3)

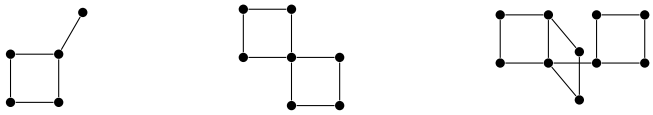

(4.4)

The tree graphs may be further sub-classified into

- Cayley trees - which are connected graphs of p vertices and $l = p-1$ edges with no closed circuits, see (4.5).
- Husimi trees - which are built up out of simple polygons attached by articulation points, see (4.6) left. It is *pure* if only one type of polygon occurs see (4.6) right.
- Star trees - which are the remaining graphs constructed of stars attached by articulation point, see (4.7).

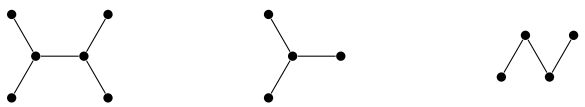

(4.5)

(4.6)

(4.7)

Given a graph G and A a vertex of degree 2, then the *suppression* of the vertex A is defined as

the deletion of A from the vertex set V of G and the identification of two edges incident on A. Reservedly, replacing an edge BC by two edges AB and AC by the creating of a new vertex A is called the *insertion* of a second-order vertex incident on the edge BC.

Two graphs G and G' are said to be *homeomorphic* if G' is a graph derived from G by the insertion or suppression of any number of vertices of degree 2. For example, see (4.8).

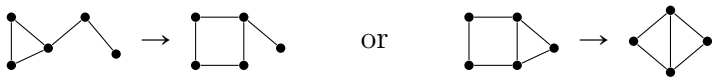

(4.8)

Homeomorphs have the same basic topology and the concept of homeomorphism plays an important role in many physical applications. For example, the number of self-avoiding walks on a lattice may be expressed in terms of all the homeomorphs of the four topological types [88].

It is important to point out that the notion of a graph defined above refers only to a topological concept, and not to a particular geometric lattice. However, it is normally possible to embed a given graph G in a d-dimensional hypercubic lattice, and for $d = 3$ it is called a simple cubic lattice. This will be discuss in section 4.2.

Our goal is to compute the expectation value of the Polyakov loop or its susceptibility with respect to the effective action, but in general, the evaluation is very difficult if one goes beyond the order three or four of the effective coupling λ. With help of the so-called high-temperature configurations, the complicated integral can be replaced by a sum of smaller terms dictated by certain configurations. The basic problem is then to count the number of ways in which one can embed particular types of configuration on a given lattice (simple cubic lattice in our case). This means that we replace the evaluation of complicated integrals with a combinatorial problem. However, this combinatorial problem can be solved systematically by computer.

4.2 Lattice constants or embeddings

4.2.1 Notation and terminology

In this section, we give a set of definitions related to those in the last section. It is convenient to assign reference symbols to the various types of linear graphs to arrange them systematically. We use g_i to denote a graph and order the subscripts i as follows. The number of vertices and lines in g_i are denoted by v_i, l_i[2], respectively. Furthermore, if $v_i < v_j$, then the subscripts are ordered so that g_i occurs before g_j; in case $v_i = v_j$ then if $l_i < l_j$. The resulting sequence reads

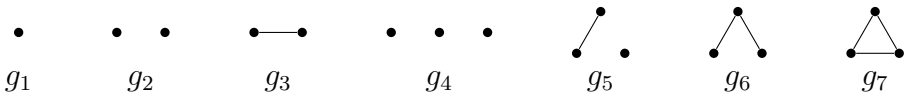

(4.9)

There exists a case of $v_i = v_j$ and $l_i = l_j$, and the first pair we obtain is

(4.10)

suppose that the suffixes have been arbitrarily assigned.

Furthermore, the symbols c_i, s_i to the various types of connected and star graphs respectively can be abbreviated from $v(c_i), l(c_i), v(s_i), l(s_i)$ as long as the meaning of which graph dictionary is being used is clear. Similarly, for a general arbitrary graph G we abbreviate

[2]These are an abbreviation of $v(g_i)$ and $l(g_i)$.

$v(G), l(G)$ to v_G, l_G.

The number of connected components in g_i are denoted by $n(g_i)$ or n_i. We have already defined the *connected component number* $c(g_i)$ by

$$c_i = l_i - v_i + n_i, \tag{4.11}$$

which is invariant under the suppression or insertion of vertices of degree 2. We have also defined homeopmorphic graphs which turn out to have the same connected component number.

If g_r and g_s are any two graphs of (4.9), then $g_r \cup g_s$ (union of g_r and g_s) denotes the disconnected graph made up of g_r and g_s. For example, $g_5 = g_1 \cup g_3$ and $g_4 = g_1 \cup g_2 = g_1 \cup g_1 \cup g_1$.

When all vertices and edges of a graph H are vertices and edges of G, then H is called a *subgraph* of G. If A is a subset of the vertices of G, the *section-graph* $G(A)$ is defined as the subgraph of G consisting of the vertices A and all the adges in G which connect two vertices of A. A *partial* graph P of G is a subgraph of G having the same vertices as G [89].

Two subgraphs have no vertices and no edges in common, then they are called *vertex-disjoint* and *edge-disjoint*, respectively. If H_1 and H_2 are two subgraphs of G we define their *sum graph* $H = H_1 + H_2$ to be the subgraph formed from all the vertices and edges of H_1 and H_2 or both.

Any subgraph G' of a graph G which is isomorphic with a graph g is said to represent an *embedding* of g in G in the weak sense (*weak embedding*). Any section graph G^* of G which is isomorphic with g is said to represent an embedding of g in the strong sense (*strong embedding*). Evidently, a strong embedding is always a weak embedding but the converse statement is not necessarily true. Any weak embedding of g in G defines a subset V' of the vertices of G. We call the section graph with vertices V' the *associated section graph* of the embedding [86].

The *lattice constant* of a graph g on a graph G is defined as follows:

- Weak (or high temperature) $(g; G)$ = Number of subgraphs of G isomorphic with g.
- Strong (or low temperature) $(g; G)$ = Nuber of section graphs of G isomorphic with g.

The graph G can be a lattice L of N sites with a periodic boundary condition. All lattice constant which does not loop the torus contains a factor N due to the symmetry. It is therefore convenient to consider the lattice constants *per site* so as to eliminate the factor N. It is sometimes convenient for conciseness to revert to the older defined terminology [35], and we then have

$$(g; L) = p_{lx}, \qquad [g; L] = P_{lx}, \tag{4.12}$$

where l is the number of lines of g.

For any graph G with v vertices and l lines we have two sets of lattice constants:

- The weak set $(g_i; G)$ for all g_i with $v_i \leqslant v$ and $l_i \leqslant l$.
- The strong set $[g_i; G]$ for all g_i with $v_i \leqslant v$ and $l_i \leqslant l$.

The set of lattice constants is thus a finite set. For example, the lattice constants of the triangle

g_7 are

$$\begin{aligned}
(g_1;g_7) &= 3, \qquad [g_1;g_7] = 3,\\
(g_2;g_7) &= 3, \qquad [g_2;g_7] = 0,\\
(g_3;g_7) &= 3, \qquad [g_3;g_7] = 3,\\
(g_4;g_7) &= 1, \qquad [g_4;g_7] = 0,\\
(g_5;g_7) &= 3, \qquad [g_5;g_7] = 0,\\
(g_6;g_7) &= 3, \qquad [g_6;g_7] = 0,\\
(g_7;g_7) &= 1, \qquad [g_7;g_7] = 1.
\end{aligned} \tag{4.13}$$

It will be noted that many more of the strong lattice constants are zero than of the weak lattice constants, and this is found to be an important characteristic difference.

4.2.2 Reduction of lattice constants

Following [86], we consider the reduction of disconnected lattice constants to connected lattice constants, and of articulated lattice constants to star lattice constants. Given a graph G which consists of two or more of its subgraphs, for example of the three subgraphs H_1, H_2, H_3 isomorphic with some g_i, g_j, g_k of the high temperature series expansion. Then

$$G = H_1 + H_2 + H_3. \tag{4.14}$$

Now H_1, H_2, H_3 are weak embeddings of g_i, g_j, g_k in G, and (4.14) is called an *overlap partition* of G into g_i, g_j, g_k. In general there will be more than one possible choice of embeddings of g_i, g_j, g_k in G having G as its sum graph, and we define the total number of such choices as the number of overlap partitions of G into g_i, g_j, g_k and write this number

$$\{g_i + g_j + g_k = G\}. \tag{4.15}$$

For example, there are three overlap partitions of the triangle g_7 into g_3 and g_6, and three into g_6 and g_6

$$\begin{aligned}
\{g_3 + g_6 = g_7\} &= 3,\\
\{g_6 + g_6 = g_7\} &= 3.
\end{aligned} \tag{4.16}$$

Overlap partitions represent the overlapping of the component graphs and have their edges and vertices in common.

Let us write down a theorem that shows that the lattice constant of any disconnected graph on a graph G can be calculated from the connected lattice constants on G. The proof of this theorem can be found in [86].

Theorem 1 *If g_i and g_j are two graphs $g_i \neq g_j$ and G any graph, then*

$$(g_i \cup g_j; G) = (g_i; G)(g_j; G) - \sum_k \{g_i + g_j = g_k^{(v)}\}(g_k^{(v)}; G)$$

where the summation is taken over all $g_k^{(v)}$ with $v < v_i + v_j$.

The usage of this theorem will be illustrated by an example, where we calculate the lattice

constant in the simple cubic lattice corresponding to two separated graphs: a square and a line.

Although the above reduction procedure is straightforward in principle, it rapidly becomes tedious for higher-order terms. Thus, nowadays lattice constants of articulated graphs are usually evaluated directly on a computer by using sophisticated counting programs. Such programs were developed initially by J. L. Martin in Chapter 2 of [35]. However, in this thesis, we will follow a more modern approach given in [36][3].

4.2.3 Graph generation and computation of lattice constants

After introducing the graph terminology relevant for the high-temperature expansion, in this section, we describe briefly the procedure of how graphs and lattice constants can be generated and computed directly on a computer, respectively. The reader is invited to read [36], where this procedure is explained very clearly.

As mentioned above, the computation of lattice constants and the generation of graphs become tedious and cumbersome for higher-order terms, indicating a combinatorial problem in our computation. This led us to the point where these procedures are needed to be automated efficiently. We start with the first issue of how to identify or label a graph such that a designed algorithm can perform a count meaning an enumeration of all possible ways in which a given class of graphs may be embedded in the lattice. This can be done using a so-called *adjacency matrix* defined as follows

$$m_{ij} = \begin{cases} 1 & \text{if vertices } i,j \text{ are connected by a bond} \\ 0 & \text{otherwise} \end{cases} \tag{4.17}$$

For convenience, the diagonal elements can be set to zero or the order of each vertex. Let us, for example, consider the following graph and its corresponding adjacency matrix

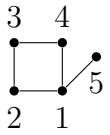

$$m = \begin{pmatrix} 3 & 1 & 0 & 1 & 1 \\ 1 & 2 & 1 & 0 & 0 \\ 0 & 1 & 2 & 1 & 0 \\ 1 & 0 & 1 & 2 & 0 \\ 1 & 0 & 0 & 0 & 1 \end{pmatrix} \tag{4.18}$$

One can generate a complete set of graphs with up to n vertices and l edges in an efficient way by picking up n isolated points first, then replacing edges on all possible pairs of points in all possible ways. This powerful enumeration algorithm is called the 'Pegs in Holes' (PIH) algorithm, and many combinatorial computer programs related to the enumeration of graphs are based on this algorithm. Here the 'pegs' are the l bonds and the 'holes' are the $n(n-1)/2$ possible links between pairs of vertices. For more detail, see Appendix 2 of [36].

It is important to avoid duplicates (same bare graphs) at as soon as possible in the generating program. This can be achieved using the concept of a *canonical labelling* and the associated *graph key*. For example, see fig. 4.1, for the bare graph 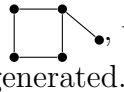 , without the concept of the canonical labelling four labellings shown in fig. 4.1 are generated. Each of these has its own unique adjacency matrix. If we take the off-diagonal elements (0 or 1) in the order

[3]To increase the efficiency of the computing process, a new and parallelized code in C++ was developed by our group.

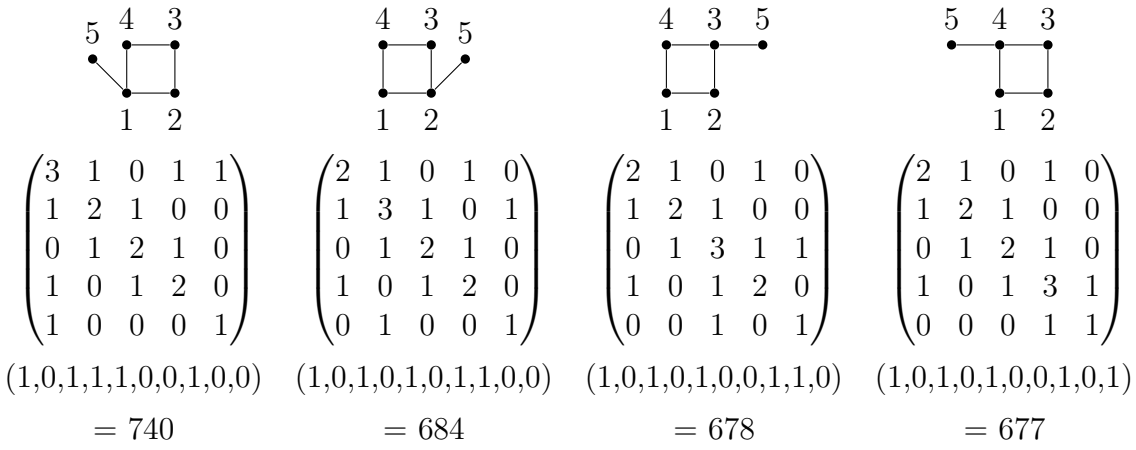

Figure 4.1: Four equivalents of a bare graph with their corresponding adjacency matrices and keys.

$m_{12}, m_{13}, m_{23}, \cdots, m_{n_1,n}$ as the binary bits of an integer, which plays a role as a unique identifier or key for each labelled graph. The labelling which maximizes the key is considered as canonical, and the corresponding key is then a unique identifier for the bare graph.

The second step of computing series expansions for lattice models is the determination of lattice constants. We describe a systematic way to compute the lattice constants for connected and disconnected graphs. As an example, we will use again the bare graph 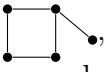 , and embed it into a square lattice. The counting algorithm uses again the PIH procedure, where the pegs are vertices of the graph and holes represent the sites of the lattice. First, the lattice sites could be specified by a pair or triple of coordinates but it is more convenient to map these onto a line, see fig. 4.2.

It is convenient to fix the graph vertices 1 and 2 at lattice sites 0 and 1 while the other vertices yield two constraints:

- no lattice site can be occupied by more than one graph vertex
- all graph edges must correspond to nearest-neighbor links on the lattice.

According to these constraints, the example graph satisfies the embeddings shown in fig. 4.3. There are 4 successful counts for this graph, which is then multiplied by the coordinate number $q = 4$ that is represented by the number of ways to replace the fixed bond $(1, 2)$ in any of the q positions and divided by the symmetry number of the graph which is 2 in this case, to gives a lattice constant $4 \times 4/2 = 8$. There are some remarks on the performance of the used codes. The method described above is essentially 'brute force'. The CPU time needed is proportional to the lattice constant which limits the length of the series which can be computed. The chain and polygon are most expensive to count.

However, there is a very fast algebraic procedure for all tree graphs as described next. The idea of this procedure is to compute the lattice constants of tree graphs, including chains, in terms of computed lattice constants of graphs with fewer vertices. For example, consider the following chain with the root vertex ●,

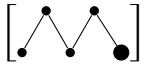 (4.19)

then there are $(q - 1)$ possible ways to add a bond to this root vertex (in general, there are

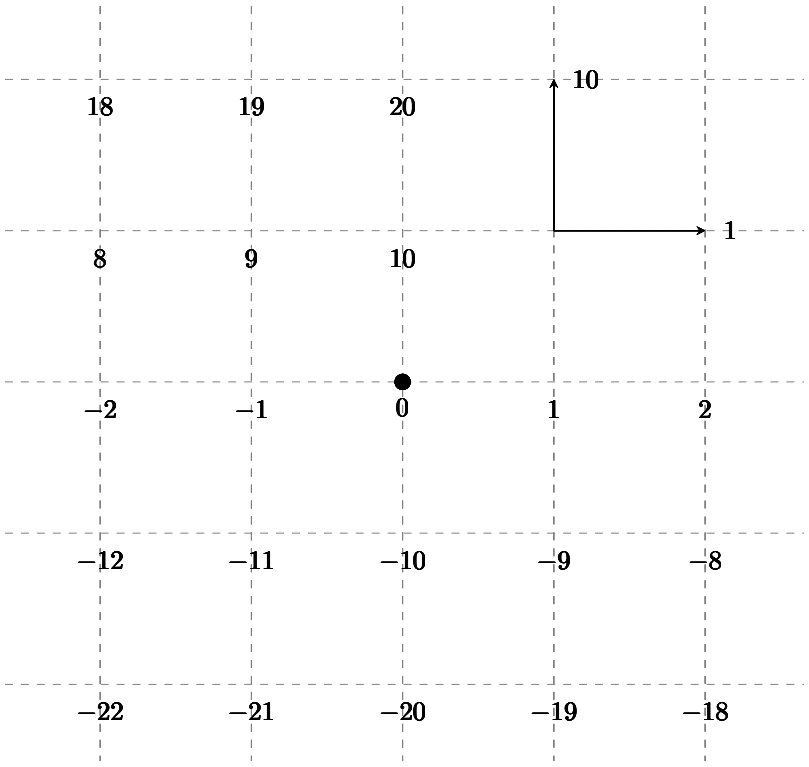

Figure 4.2: The vertices are mapped onto a segment of a line on the square lattice. Two basic vectors $(\vec{e}_1, \vec{e}_2)$ are represented by $(1, N)$. Every lattice site has a unique index referenced to an origin 0. N must be large enough to prevent wrap-around effects, here $N = 10$.

$(q - o)$ possibilities where o is the order of the root vertex). And the result is illustrated as follows

$$(q-1)\left[\;\right] = \left[\;\right] + \left[\;\right] \tag{4.20}$$

We finally rearrange eqn. (4.20) with consideration of the additional symmetry factors which arise when rooted graphs are replaced by bare graphs.

$$2\left[\;\right] = 2(q-1)\left[\;\right] - 2\left[\;\right] \tag{4.21}$$

We can check this for the simple square lattice, and the result is

$$\left[\;\right] = \frac{1}{2}\left(6 \cdot 50N - 2 \cdot 8N\right) = 142N,$$

which coincides with the result of the direct computation. Here N denotes the number of lattice sites.

While the Ising model and the pure gauge effective theory can be computed using only connected and closed graphs, to employ high-temperature expansion for the effective theory including fermions, disconnected graphs must also be taken into account. Generation of disconnected graphs is done from a starting list of connected graphs. Computing the lattice constants of disconnected graphs can be cumbersome, however, a similar procedure to that for

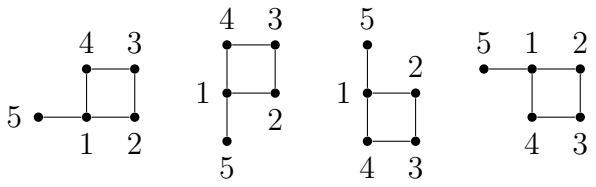

Figure 4.3: Embedding of the example graph on the simple square lattice.

tree graphs can be employed. For example, we want to compute the lattice constant for two disconnected squares

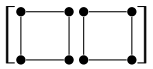 (4.22)

First, we multiply two sets of all embeddings of a single square to generate the list of sets as follows

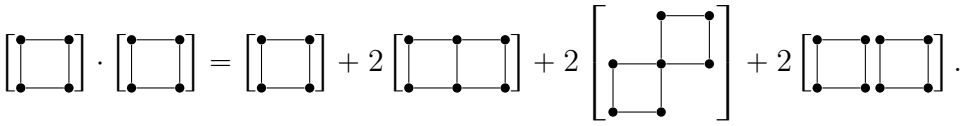 (4.23)

Then it is straightforward to obtain a symbolic equation for the lattice constant of two disconnected squares

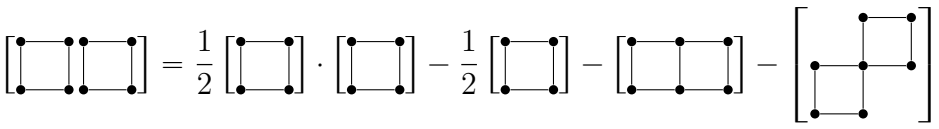 (4.24)

Suppose that we already know the lattice constants of the set of the connected graphs on the simple square lattice, in this case

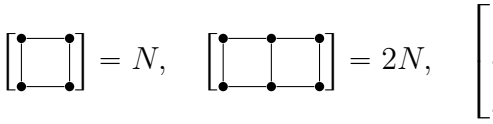 (4.25)

Substituting (4.25) into (4.24), we obtain the final result for the lattice constant of two disconnected square

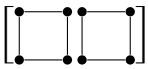 (4.26)

In general, lattice constants of disconnected graphs can be computed recursively from graphs with fewer vertices and fewer components, by isolating one component and enumerating all possible overlaps with the graph formed from the remaining components [36].

4.3 High-temperature susceptibility

Based on the method of computing the lattice constants described previously, we are now able to compute a 13th power series for the susceptibility of the pure gauge effective theory including

static quarks on the simple cubic lattice. The pure effective theory can be easily obtained by sending the coupling $h_1 \to 0$. The expansion scheme employed is called high-temperature expansion, which would have been near state-of-the-art 40 years ago before the Monte-Carlo method, and is still a reasonable long series, far longer than could be achieved by hand.

We emphasize again that the advantage of the high-temperature expansion is an analytic method and does not suffer from the fermion sign problem. General concepts of the high-temperature expansion applied to Ising models can be found, for instance, in [35, 36]. This method is particularly simple for Ising models without an external field because their spins can only take two values $+1$ or -1 and the set of graphs involved is sufficiently small, however, on the other hand for the effective theory it gets much more complicated since our "spins" are Polyakov loops and the presence of fermions in the effective theory enlarges the set of graphs significantly.

Throughout this chapter, the main action evaluated by the high-temperature expansion contains the pure gauge effective action with the static quark determinant given in eqn. (3.15) and (3.27), respectively. Instead of λ_1, in the following it is convenient to drop the index and use (λ, h_1) as our expansion parameters. To illustrate the calculation more comprehensively, let us write down again the desired $N_f = 1$ three-dimensional effective action

$$Z = \int \mathscr{D}U_0 e^{-S_{\text{eff}}} = \int \mathscr{D}U_0 \det[D_{\text{stat}}] \prod_{\langle \vec{n}_1, \vec{n}_2 \rangle} [1 + \lambda(L_{\vec{n}_1} L^*_{\vec{n}_2} + L^*_{\vec{n}_1} L_{\vec{n}_2})], \tag{4.27}$$

$$\det[D_{\text{stat}}] = \prod_{\vec{n}} [1 + h_1 L_{\vec{n}} + h_1^2 L^*_{\vec{n}} + h_1^3]^2 [1 + \bar{h}_1 L^*_{\vec{n}} + \bar{h}_1^2 L_{\vec{n}} + \bar{h}_1^3]^2. \tag{4.28}$$

Our main goal is to extract information about phase transitions from the series, which can be achieved by using the Polyakov loop susceptibility χ_L which peaks at the phase transition and is defined to be

$$\chi_L = \frac{1}{V} \frac{\partial^2}{\partial J^2} \log Z[J] \bigg|_{J=0} = V \left(\langle L^2 \rangle - \langle L \rangle^2 \right), \tag{4.29}$$

where $Z[J]$ is the partition function coupled to an external source J as follows

$$Z[J] = \int \mathscr{D}U_0 \exp \left[-S_{\text{eff}} + J \sum_{\vec{n}} (L_{\vec{n}} + L^*_{\vec{n}}) \right]. \tag{4.30}$$

Before we show an example of how to perform the series expansion on the partition function, it is advantageous to combine the measure $\mathscr{D}U_0$, the static quark determinant $\det[D_{\text{stat}}]$ and the external source part together since they are just product over the spatial space. The combined measure is of the form

$$\mathrm{d}\mathcal{M}_{\vec{n}}[J] \equiv \mathrm{d}W_{\vec{n}} [1 + h_1 L_{\vec{n}} + h_1^2 L^*_{\vec{n}} + h_1^3]^2 [1 + \bar{h}_1 L^*_{\vec{n}} + \bar{h}_1^2 L_{\vec{n}} + \bar{h}_1^3]^2 e^{J(L_{\vec{n}} + L^*_{\vec{n}})}. \tag{4.31}$$

Then the partition function is simplified into

$$Z[J] = \int \prod_{\vec{n}} \mathrm{d}\mathcal{M}_{\vec{n}}[J] \prod_{\langle \vec{n}_1, \vec{n}_2 \rangle} \left[1 + \lambda(L_{\vec{n}_1} L^*_{\vec{n}_2} + L^*_{\vec{n}_1} L_{\vec{n}_2}) \right]. \tag{4.32}$$

Then we can expand the partition function in a power series in λ as

$$\begin{aligned} Z[J] = &\int \prod_{\vec{n}} \mathrm{d}\mathcal{M}_{\vec{n}}[J] + \lambda \int \prod_{\vec{n}} \mathrm{d}\mathcal{M}_{\vec{n}}[J] \sum_{\langle \vec{n}_1, \vec{n}_2 \rangle} 2\,\mathrm{Re}(L_{\vec{n}_1} L^*_{\vec{n}_2}) \\ &+ \lambda^2 \int \prod_{\vec{n}} \mathrm{d}\mathcal{M}_{\vec{n}}[J] \sum_{\langle \vec{n}_1, \vec{n}_2 \rangle} \sum_{\langle \vec{n}_3, \vec{n}_4 \rangle} 4\,\mathrm{Re}(L_{\vec{n}_1} L^*_{\vec{n}_2})\,\mathrm{Re}(L_{\vec{n}_3} L^*_{\vec{n}_4}) \\ &+ \lambda^3 \int \prod_{\vec{n}} \mathrm{d}\mathcal{M}_{\vec{n}}[J] \sum_{\langle \vec{n}_1, \vec{n}_2 \rangle} \sum_{\langle \vec{n}_3, \vec{n}_4 \rangle} \sum_{\langle \vec{n}_5, \vec{n}_6 \rangle} 8\,\mathrm{Re}(L_{\vec{n}_1} L^*_{\vec{n}_2})\,\mathrm{Re}(L_{\vec{n}_3} L^*_{\vec{n}_4})\,\mathrm{Re}(L_{\vec{n}_5} L^*_{\vec{n}_6}) + \mathcal{O}(\lambda^4). \end{aligned} \tag{4.33}$$

It is straightforward to see that this series becomes very messy for higher orders of λ. However, we can rearrange the partition function through a graph representation which has been described previously. The graph representation of eqn. (4.33) takes the form

$Z[J] =$ 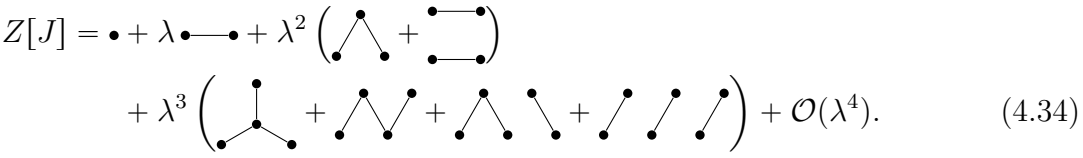 $+ \mathcal{O}(\lambda^4).$ (4.34)

Here the transformation rules are quite simple: for each graph, the order of λ corresponds to the number of edges, and the number of edges coupled to a vertex gives a count for the number of Polyakov loops at this vertex. To calculate eqn. (4.34) systematically, there are two main steps:

- *Graph counting.* This means computing the lattice constant of each graph, which gives the number of ways a graph can be embedded on the lattice. This step is discussed in the previous section, and a table of up to four bond graphs and their lattice constants on a simple cubic lattice can be found in Tab. 4.1, where $N = N_s^3$ is the number of lattice sites. Since the series expansion method allows a lattice of arbitrary large volumes, meaning that our calculations can be approximately considered as in the thermodynamic limit, and no infinite volume extrapolation is needed.
- *Graph evaluation.* This step can be illustrated by the following example of explicit calculation for the first order graph in $Z[J]$,

 $= \int \prod_{\vec{n}} \mathrm{d}\mathcal{M}_{\vec{n}}[J] \sum_{\langle \vec{n}_1, \vec{n}_2 \rangle} \left(L_{\vec{n}_1} L^*_{\vec{n}_2} + L^*_{\vec{n}_1} L_{\vec{n}_2} \right)$

$$\begin{aligned} &= 3N \left(\int \mathrm{d}\mathcal{M}_{\vec{n}}[J] \right)^{N-2} 2 \left(\int \mathrm{d}\mathcal{M}_{\vec{n}}[J] L_{\vec{n}} \right) \left(\int \mathrm{d}\mathcal{M}_{\vec{n}}[J] L^*_{\vec{n}} \right) \\ &= 6N z_0^{N-2} z_1 z_1^*. \end{aligned} \tag{4.35}$$

Here the nearest neighbor sum gives $3N$ integrals of the same kind, i.e. our computations are reduced to single site integrals as shown in eqn. (4.36). The single site group integrals

$$I(n,m) = \int_{SU(3)} \mathrm{d}W L^n L^{*m}, \tag{4.36}$$

can be evaluated using an explicit formula derived by using the technique of generating functions [90]. We should point out the triality constraint of (4.36) that for $I(n,m)$ to be non-vanishing $(n-m) \mod 3 = 0$ must be satisfied. This constraint will make a big impact

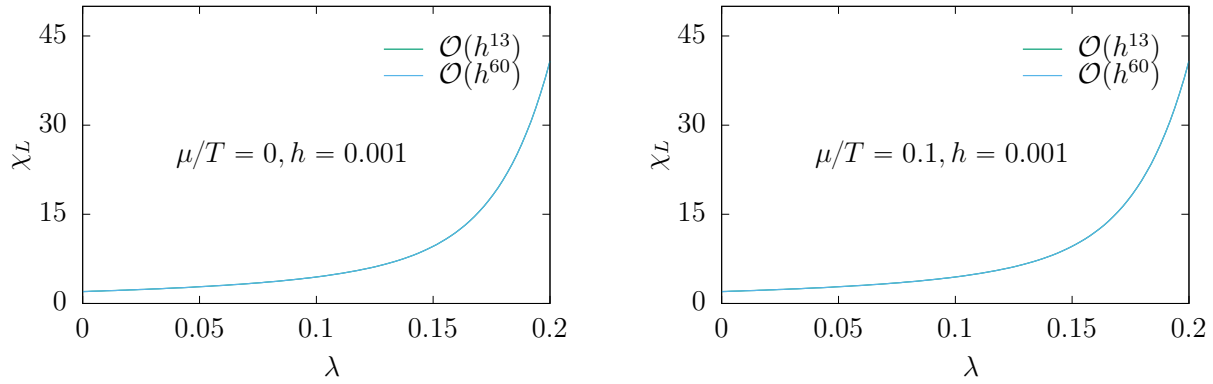

Figure 4.4: Comparison of the Polyakov loop susceptibility between order 13 and 60 in the hopping parameter. Here $h_1 = (2\kappa)^{N_t} e^{\mu/T} \equiv h e^{\mu/T}$. Left: $\mu/T = 0$. Right: $\mu/T = 0.1$.

on the selection of non-vanishing graphs. To proceed with our computation we have to expand down $\exp[J(L_{\vec{n}} + L^*_{\vec{n}})]$ to the wanted order. Our code is capable to calculate up to $\mathcal{O}(h_1^{60}, \bar{h}_1^{60})$, but a truncation to the order $\mathcal{O}(h_1^{13}, \bar{h}_1^{13})$ is checked to be good enough as one can see in fig. 4.4. Finally, the Polyakov loop susceptibility χ_L is obtained by taking the derivative of $\log Z[J]$ two times with respect to the external source J as in eqn. (4.29) and sending $J \to 0$ afterward. At $\mathcal{O}(\lambda^1)$, the complete calculation of $Z[J]$ is already too long to be printed, however, for simplicity, we can just show the first order of the partition function without an external source[4] by letting $J \to 0$. Three single site integrals in (4.36) simply become

$$\begin{aligned} z_0 =& (1 + 4h_1^3 + h_1^6) + (4h_1 + 6h_1^4)\bar{h}_1 + (10h^2 + 6h^5)\bar{h}_1^2 + (4 + 20h_1^3 + 4h_1^6)\bar{h}_1^3 \\ &+ (6h_1 + 10h_1^4)\bar{h}_1^4 + (6h_1^2 + 4h_1^5)\bar{h}_1^5 + (1 + 4h_1^3 + h_1^6)\bar{h}_1^6, \qquad (4.37) \\ z_1 =& (3h_1^2 + 2h_1^5) + 2(1 + 6h_1^3 + h_1^6)\bar{h}_1 + (8h_1 + 15h_1^4)\bar{h}_1^2 + 4(5h_1^2 + 3h_1^5)\bar{h}_1^3 \\ &+ (3 + 20h_1^3 + 3h_1^6)\bar{h}_1^4 + (4h_1 + 8h_1^4)\bar{h}_1^5 + (3h_1^2 + h_1^5)\bar{h}_1^6. \qquad (4.38) \\ z_1^* =& (2h_1 + 3h_1^4) + (8h_1^2 + 4h_1^5)\bar{h}_1 + (3 + 20h_1^3 + 3h_1^6)\bar{h}_1^2 + (12h_1 + 20h_1^4)\bar{h}_1^3 \\ &+ (15h_1^2 + 8h_1^5)\bar{h}_1^4 + (2 + 12h_1^3 + 2h_1^6)\bar{h}_1^5 + (2h_1 + 3h_1^4)\bar{h}_1^6. \qquad (4.39) \end{aligned}$$

It is obvious that beyond the first few orders each computation step of the Polyakov loop susceptibility such as graph generations, lattice constant calculations, and single-site SU(3) group integral calculations become cumbersome. Fortunately, these can be automatized on a computer with the use of the state-of-the-art algorithm described above.

4.4 Series analysis methods

After the discussion of how the high-temperature expansion is used to compute the Polyakov loop susceptibility which is a series in the power of $(\lambda, h_1, \bar{h}_1)$, we now turn to another problem of how this series is analyzed, such that the information about criticality for our theory can be revealed. In this section, we will describe the two main methods: Padé approximant

[4] An external source is not needed per se, if one just wants to obtain results at leading orders, however, it becomes a crucial technique for higher-order calculations.

Label	Graphs	Embeddings	Label	Graphs	Embeddings
1.1		$3N$	2.2		$-33N$
2.1		$15N$	3.3		$-1440N$
3.1		$20N$	3.4		$876N$
3.2		$75N$	4.5	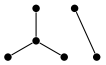	$-10080N$
4.1		$15N$	4.6		$-37512N$
4.2	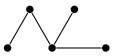	$300N$	4.7		$90072N$
4.3		$363N$	4.8		$-38286N$
4.4		$3N$	4.9		$-20556N$

Table 4.1: Connected and separated graphs with up to four bonds with labels and embeddings on a simple cubic lattice.

and Canterbury approximant, whose combination can determine the critical endpoint from a multivariate series. We refer the reader to [91, 92] for an extensive introduction to series analysis.

4.4.1 Padé approximant

Suppose that we are given a power series associated to a function $f(x)$

$$f(x) = \sum_{i=0}^{\infty} c_i x^i. \tag{4.40}$$

For any analysis using Padé approximant, this power series is the fundamental starting point. In practice, we can only obtain a finite power N for the series. A $[L/M]$ Padé approximant (PA) is a rational fraction of two polynomials P_L and Q_M of degree L and M respectively,

$$[L/M] = \frac{P_L(x)}{Q_M(x)} = \frac{p_0 + p_1 x + \cdots + p_L x^L}{q_0 + q_1 x + \cdots + q_M x^M}, \quad L + M \leqslant N, \tag{4.41}$$

where its Maclaurin expansion agrees with $L + M + 1$ series coefficients of (4.40) as far as possible, and without loss of generality, we take $q_0 = 1$. The $L + M + 1$ coefficients $p_0, p_1, \ldots, p_L, q_1, \ldots, q_M$ are determined by equating like powers of x, i.e. one solves two systems of linear equations. The eqn. (4.41) indicates that Padé approximants of sufficiently high order will exactly represent rational functions with which one can analyze critical points and non-analyticities of the series. Two important properties of the Padé approximant are that the diagonal $[N/N]$ PAs are invariant under homographic transformation, $y = (ax + b)/(cx + d)$

which is useful for analytic continuation, and also under Euler transformation $x = Aw/(1+By)$ which explains the acceleration of convergence using the sequence of diagonal PAs [92].

A Padé approximant is able to present functions with simple poles - poles of order one, exactly. Thus, in the study of critical phenomena it is advantageous to take the logarithmic derivative of the series, which converts an algebraic singularity into a simple pole. For example, given a function $f(x)$ of the form

$$f(x) = \frac{A}{(x - x_c)^\alpha}, \quad \text{then} \quad \mathrm{d}\log f(x) = \frac{f'(x)}{f(x)} = \frac{\alpha}{x - x_c}. \tag{4.42}$$

One can now use the denominator polynomial $Q_M(z)$ to estimate the location of the singular points, while the exponents are obtained from the corresponding residues.

4.4.2 Canterbury approximant

In the field of critical phenomena, many significant physical systems have more than one coupling. For example, the Ising model in an external magnetic field, the $O(n)$ symmetric lattice ϕ^4 theory in four dimensions, or the theory of our interest - QCD at finite temperature and finite chemical potential. Thus, a novel method for approximating functions of two or more variables that exhibits singular behavior of a relevant theory is needed. It is natural to consider a generalization of the Padé approximant to more than one variable. It turns out that we can just focus on the case of two-variable problems because the more-variable cases can be treated similarly. In this section, we consider the simplest scheme for a direct formulation of two-variable rational approximants, i.e. without a reduction to a single variable. This approach was developed by Chisholm and his coworkers [93–95]. Consider the following two-variable series

$$f(x, y) = \sum_{i=0}^{\infty} \sum_{j=0}^{\infty} c_{ij} x^i y^j. \tag{4.43}$$

Our focus is to construct the defining lattice spaces $\mathcal{L}$ and $\mathcal{M}$ and polynomials of two variables

$$A(x, y) = \sum_{i,j \in \mathcal{L}} a_{ij} x^i y^j, \tag{4.44}$$

and

$$B(x, y) = \sum_{i,j \in \mathcal{M}} b_{ij} x^i y^j, \tag{4.45}$$

so that

$$f(x, y) = \frac{A(x, y)}{B(x, y)} + \sum_{i=0}^{\infty} \sum_{j=0}^{\infty} e_{ij} x^i y^j, \tag{4.46}$$

where most of the coefficients e_{ij} are zero. The basic idea is similar to the Padé approximant that we approximate the function $f(x, y)$ by a ratio of two polynomials of two variables, where the coefficients are chosen to reproduce the original coefficients to as high an order as possible. The numerator and denominator coefficients have been taken to lie in lattice spaces $\mathcal{L}$ and $\mathcal{M}$, and there exists a requirement that e_{ij} for $i, j \in \mathcal{E}$, the equality lattice space.

Similarly to the Padé approximant one can choose $b_{00} = 1$ without loss of generality, then

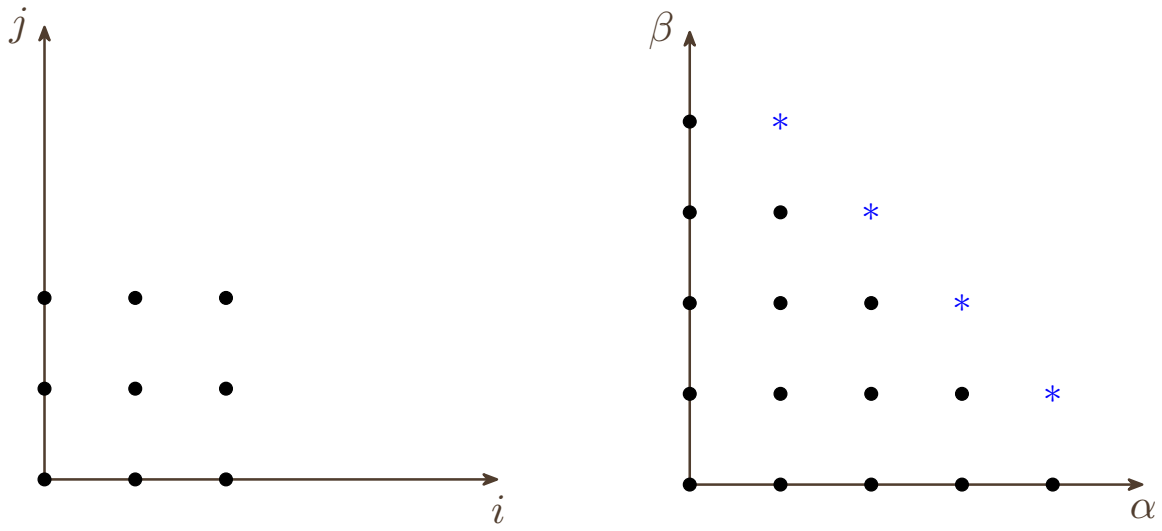

(a) The lattice space $\mathcal{L}$ (b) The lattice space $\mathcal{E}$

Figure 4.5: The lattice spaces $\mathcal{L}$ and $\mathcal{E}$ for the [2/2] Canterbury approximant.

this scheme is determined by

$$\dim(\mathcal{E}) = \dim(\mathcal{L}) + \dim(\mathcal{M}) - 1. \tag{4.47}$$

This is the foundation for a variety of approximation schemes. The most systematic developments are known as the Canterbury approximants. The Canterbury scheme is known to inherit many of the interesting invariance properties of ordinary, in particular diagonal Padé approximants, see [92]. Furthermore, it satisfies accuracy-through-order conditions and reduces to Padé approximants if either x or y is zero. Typically, this scheme is defined by writing $A(x, y)$ and $B(x, y)$ as

$$A^{[L/L]}(x, y) = \sum_{i=0}^{L} \sum_{j=0}^{L} a_{ij} x^i y^j, \tag{4.48}$$

$$B^{[L/L]}(x, y) = \sum_{i=0}^{L} \sum_{j=0}^{L} b_{ij} x^i y^j, \qquad b_{00} = 1. \tag{4.49}$$

An example of the lattice space $\mathcal{L}$ and $\mathcal{M}$ for the [2/2] Canterbury approximant corresponding to (4.48) and (4.49) are presented in fig. 4.5 (a), where the lattice spaces $\mathcal{L}$ and $\mathcal{M}$ are identical. Then at order (α, β) we obtain the following equality equations

$$\sum_{i=0}^{\alpha} \sum_{j=0}^{\beta} b_{ij} c_{\alpha-i,\beta-j} = a_{\alpha,\beta}, \qquad (\alpha, \beta) \in \mathcal{L}, \tag{4.50}$$

and

$$\sum_{i=0}^{\min(\alpha,L)} \sum_{j=0}^{\min(\beta,L)} b_{ij} c_{\alpha-i,\beta-j} = 0, \qquad (\alpha, \beta) \in \mathcal{E}, \quad (\alpha, \beta) \notin \mathcal{L}. \tag{4.51}$$

Then the numerator coefficients are determined by (4.50) once the denominator coefficients are

determined. The coefficients b_{ij} are determined by (4.51), and the determination of the lattice space $\mathcal{E}$ is illustrated by an explicit example. In fig. 4.5 (b), we present the lattice space $\mathcal{E}$ for the [2/2] Canterbury approximant[5].

For $y = 0$, we need an exact accuracy to order x^3 and x^4 to be able to determine the coefficients b_{10} and b_{20}, and to obtain the [2/2] Padé approximant. An accuracy through order x^3, x^4, x^3y, y^3, y^4, and y^3x is required to obtain six of the eight equations, which are then solved for the coefficients b_{ij}, as indicated by $*$ in fig. 4.5 (b). The other two equations are obtained by adding the equations (4.51) for order x^3y^2 and x^2y^3, and those for order x^4y and xy^4. These two equations are called symmetrized equations. Thus Canterbury approximants always satisfy accuracy-through-order conditions for orders up to $x^{2L-\alpha}y^{\alpha}$, $\alpha = 0, 1, ..., 2L$. For symmetric functions, the symmetrising process becomes a formality, and the approximants are accurate through orders x^{2L}, y^{2L}, and $x^{2L+1-\alpha}y^{\alpha}$, $\alpha = 1, 2, ..., 2L$. Suppose that the necessary approximants exist, the scheme has the following properties: Canterbury approximants reduce to diagonal Padé approximants if either variable is zero; they also satisfy restricted homographic invariance, duality, unitarity, and the factorization rule. For more detail and proof of these properties, see for instance [93, 95].

[5]Unlike Padé approximants, there is no available library in `Mathematica` for computing Canterbury approximants of higher orders. For this purpose, we have written a program in `Mathematica` to automatize the process of computing Canterbury approximants

Chapter 5

Numerical treatment for the effective theory

> The first real applications of the statistical sampling method to research problems in physics seem to have been those of Enrico Fermi, who was working on neutron diffusion in Rome in the early 1930s. Fermi never published his numerical methods ... .
>
> *M. E. J. Newman, G. T. Barkema in [96]*

In the last chapter, we discussed the analytic treatment of the pure gauge effective theory including static quarks. Although we have come a long way towards finding a suitable expansion scheme for the effective theory with static quarks, it is realized that analytic methods are usually applicable to physical systems whose action is sufficiently simple only, for example the pure gauge effective theory, with static quarks or potentially with the κ^2-correction. On the other hand, these methods are not suitable for the effective theory with the κ^4- or higher corrections due to the complexity of its action. The deconfinement endpoint of the effective theory is improved with higher corrections and approaches the value of full QCD. For this reason, the higher correction effective theory is treated by Monte-Carlo methods. Although only the case of zero chemical potential is considered, we should note that at finite chemical potentials the fermion sign problem of the effective theory is mild enough for simulations to be possible, since many degrees of freedom associated with spacial links have been integrated out.

5.1 Monte Carlo algorithms

The standard numerical method used to calculate the partition function of QCD is Monte-Carlo simulation. The Monte-Carlo simulations are based on Markov chains in combination with the concepts of ergodicity and importance sampling. This is currently still the most efficient method for computing functional integrals of lattice QCD where the dimensionality of the integrals is way too high for usual numerical integration techniques. In this section, the fundamentals of this method are briefly introduced; see for example [3, 48, 50] for more details.

Because of the Grassmann nature of the quark fields in the QCD functional integral, standard Monte-Carlo methods do not allow such fields to be simulated directly. Thus, it is required

to simulate the theory after integrating out the quark fields. As described in section 2.5.2, one can extract the physics described by QCD by calculating expectation values

$$\langle \mathcal{O} \rangle = \frac{1}{Z} \int \mathscr{D}U \det[D] e^{-S_G[U]} \mathcal{O}. \tag{5.1}$$

Here, we can re-express this formula to obtain a normalized probability density on the space of all gauge fields

$$p[U] = \frac{1}{Z} \det[D] e^{-S_G[U]}. \tag{5.2}$$

We note that this density only works if it is real, which is normally the case if a chemical potential is not present. One then selects configurations of U's according to this density, and this step is the central idea of the importance sampling. Assume that a set of configurations $U^{(n)}$ with $n = 1, \ldots, N$ is generated, then the expectation value of the observable $\mathcal{O}$ is given by

$$\langle \mathcal{O} \rangle = \lim_{N \to \infty} \frac{1}{N} \sum_{n=1}^{N} \mathcal{O}[U^{(n)}]. \tag{5.3}$$

In practice, actual calculations are carried out only at a finite number N, and the uncertainty of the mean is of order $1/\sqrt{N}$ [48].

We note that most large-scale simulations used today are based on the so-called Hybrid Monte Carlo algorithm [97]. However, since the effective theory is a function of temporal gauge links or Polyakov loops only, the link-update algorithms used for the pure SU(3) gauge theory can still be applied for reasons of efficiency, i.e. the complicated step of calculating the fermion determinant is not involved.

5.1.1 The Metropolis algorithm

Configurations according to desired distributions are generated through some iterative procedure called the Markov process, i.e. the field configurations are obtained one after another via some stochastic algorithm. A Markov process is characterized by two important properties: ergodicity (or in practice, relaxed ergodicity), i.e. a Markov chain must be able to cover the whole space of configurations with a finite number of steps; and detailed balance where for a probability p and a transition probability P_{trans} we have

$$P_{\text{trans}}(U \to U') p[U] = P_{\text{trans}}(U' \to U) p[U']. \tag{5.4}$$

The Metropolis algorithm is the simplest stochastic algorithm that can be used to construct a Markov chain. This algorithm consists of two steps: The proposal and the accept/reject step. Let us explain this in more details. First a new candidate configuration U' is proposed by employing a selection probability $H(U \to U')$, and then the configuration U' is accepted with probability

$$P_{\text{acc}}(U \to U') = \min \left[1, e^{-(S_G[U] - S_G[U'])} \frac{H(U' \to U) \det D[U']}{H(U \to U') \det D[U]} \right], \tag{5.5}$$

as the next configuration in the Markov chain, and if U' has not been accepted, we set $U' = U$. Note that the inclusion of $\det[D]$ in (5.5) is not relevant for our case, because the effective theory is simulated without the calculation of the fermion determinant. Furthermore, it is convenient to implement it with a symmetric proposal probability, i.e. the transition probability $H(U \to U')$ of a state U to another state U' equals the transition probability $H(U' \to U)$ of the state U' to the state U. Then the accept/reject step takes the simple form

$$P_{\text{acc}}(U \to U') = \min\left[1, e^{-(S_G[U]-S_G[U'])}\frac{\det D[U']}{\det D[U]}\right]. \tag{5.6}$$

The expectation value of an gauge-invariant operator $\mathcal{O}$ can be approximated by

$$\langle \mathcal{O} \rangle = \lim_{N\to\infty} \frac{1}{N}\sum_{n=1}^{N} \mathcal{O}[U_n], \tag{5.7}$$

where we have used N configurations U_n of link variables which are distributed according to the equilibrium probability $p[U]$ in equation (5.2).

Link proposal

We briefly describe how the link proposal works, for more details see [3, 48, 59]. The link proposal is a crucial step of the Metropolis algorithm. This step helps find a suitable proposal for the new configurations of links. It is advantageous to apply the local update procedure and to change the link such that the new link is close to the old link. This will give a large acceptance rate, and consequently a symmetric proposal probability. For gauge group $\mathrm{SU}(N_c)$ we have the additional constraint that the new link is again an element of the group. This means that a naive generalized proposal of the form[1] $U \to U + \delta \cdot \varepsilon \mathbb{1}$, similar to the one used for the harmonic oscillator will not work, since the new matrix U' would not belong to the group $\mathrm{SU}(N_c)$ anymore. To find a suitable proposal, we can use the property that the multiplication of two elements of $\mathrm{SU}(N_c)$ leads to another element of $\mathrm{SU}(N_c)$, so that we can implement the proposal following

$$U' = \Theta U \in \mathrm{SU}(N_c) \qquad \text{with} \qquad \Theta \in \mathrm{SU}(N_c). \tag{5.8}$$

Here Θ should be an element of $\mathrm{SU}(N_c)$ and close to the unit matrix.

The construction of the matrix Θ can be done by making use of the fact that elements of $\mathrm{SU}(N_c)$ can be represented in terms of the fields θ that are elements in the corresponding algebra $\mathfrak{su}(N_c)$. We can thus express Θ as

$$\Theta = e^{\theta} \quad \text{with} \quad \theta = \sum_{a=1}^{N_c^2-1} \theta^a (iT^a), \tag{5.9}$$

where θ is an element of the anti-hermitian representation of the Lie algebra $\mathfrak{su}(N_c)$. For Θ close to the unit matrix, then the matrix θ must contain small coefficients θ^a. The coefficients

[1] Note that for simplicity we write U instead of the link $U_\mu(x)$ that we want to update. U does not indicate an entire field configuration anymore.

can be generated as follows

$$\theta^a = \delta \cdot \epsilon. \tag{5.10}$$

Here $\delta \in [-1, 1]$ is a random variable and ϵ a fixed small number. This procedure has a big advantage because it leads to a symmetric proposal probability since θ and $-\theta$ are equivalently likely and $\exp(-\theta) = \Theta^{-1}$. The last step for the implementation of the proposal is to find a suitable implementation of the exponential function from $\mathfrak{su}(N_c)$ to $\mathrm{SU}(N_c)$.

$\mathrm{SU}(N_c)$ exponential function

The exponential function is either implemented fully by using the Cayley-Hamilton theorem [98] or implemented with a suitable approximation including certain properties that are required by the desired algorithm [99]. On one hand, the first option can be correct up to machine precision, however, it normally requires a high numerical demand in comparison to the approximation option. For the Metropolis algorithm, an approximation to the exponential function is good enough.

In the case of the SU(2) gauge group, it is possible to use both the exact representation

$$\exp(i\phi(\vec{n} \cdot \vec{r})) = \cos(\phi)\mathbb{1} + i\sin(\phi)(\vec{n} \cdot \vec{r}), \tag{5.11}$$

where $\vec{n}$ is a unit vector and $\vec{r}$ is the vector of Pauli matrices, or the approximation via the Cayley map

$$e^{iX} = \frac{1 + iX/2}{1 - iX/2}, \tag{5.12}$$

where $X \in \mathfrak{su}(N_c)$. It is straightforward to see that the exact representation demands three matrix multiplications for each proposal step since one needs to repeat the computation for each of the coefficients. The latter is more efficient since the only complicated computation is to inverse the 2×2 matrices which can be carried out explicitly. Furthermore, the approximated implementation can be easily applied with the anti-hermitian form of the Lie algebra. For the gauge group SU(3), a suitable approximation can be constructed from SU(2) matrices embedded in 3×3 matrices, for more details see [99].

The local effective action

The efficiency of the Metropolis algorithm can be improved significantly if we use the local action in the accept/reject step. To demonstrate the idea of the Metropolis algorithm more transparently, let us discuss how to apply this algorithm to the SU(3) pure gauge effective theory. The Metropolis algorithm can be easily generalized to be used for a more complicated effective theory involving heavy quarks. Let us write down again the action of the pure gauge effective theory here

$$S_{G,\mathrm{eff}} = -\sum_{\langle \vec{n}_1, \vec{n}_2 \rangle} \log\left(1 + 2\lambda \mathrm{Re}(L_{\vec{n}_1} L^*_{\vec{n}_2})\right). \tag{5.13}$$

The procedure called maximal tree allows transforming a set of link variables to the identity $\mathbb{1}$ until a link U^* which connects to another link that already has been transformed to $\mathbb{1}$ before. Thus, here $L_{\vec{n}} = \mathrm{tr} \prod_t U_0(t, \vec{n}) = \mathrm{tr}\, U(\vec{n})$. If we want to update the link $U(\vec{n})$ or the Wilson

line, i.e. we make a random change $U(\vec{n}) \to U'(\vec{n})$ or $L_{\vec{n}} \to L'_{\vec{n}}$. For the effective theory, it is straightforward to see that a random change of U only affects its corresponding Polyakov loop while its six nearest-neighbor Polyakov loops are unaffected. The local contribution to the three-dimensional effective Yang-Mills action is

$$S^{\text{loc}}_{G,\text{eff}}[U'] = -\sum_{\vec{n}_2} \log\left(1 + 2\lambda \text{Re}(L'_{\vec{n}_1} L^*_{\vec{n}_2})\right), \tag{5.14}$$

where $\vec{n}_2$ represents six nearest-neighbor points of $\vec{n}_1$. Due to the nature of the logarithm in the action, instead of computing the change in the local action in the accept/reject step it is convenient to consider a direct change of the acceptance probability, i.e.

$$\Delta p = \frac{\prod_{\vec{n}_2}(1 + 2\lambda \text{Re}(L_{\vec{n}_1} L^*_{\vec{n}_2})}{\prod_{\vec{n}_2}(1 + 2\lambda \text{Re}(L'_{\vec{n}_1} L^*_{\vec{n}_2})}. \tag{5.15}$$

Let us remark that the computer time required per link update is quite small for the effective theory up to $\mathcal{O}(\kappa^2)$. For the effective theory at $\mathcal{O}(\kappa^4)$ or higher, the computer time per link update increases significantly due to the complexity of the action. As we have already mentioned earlier, for the implementation of the effective theory at high orders to be feasible, the approach described in section 3.4 should be developed.

5.2 The sign problem

The progress of investigating lattice QCD at finite chemical potential is far from being settled due to the violation of γ_5-hermiticity of the Dirac operator when a chemical potential is introduced. As a consequence, this violation makes the determinant $\det[D]$ complex, and the QCD path integral at finite chemical potential cannot be evaluated by standard Monte-Carlo methods. One can easily see it by the following equation

$$\gamma_5 D(\mu) \gamma_5 = D^\dagger(-\mu^*). \tag{5.16}$$

Taking the determinant on both sides of the equation and using some simple properties of linear algebra, we obtain

$$[\det D(\mu)]^* = \det D(-\mu^*). \tag{5.17}$$

At $\mu = 0$ or when μ is a purely imaginary chemical potential, this gives back the positive-definite determinant, which allows us to simulate the lattice QCD path integral with standard Monte-Carlo methods. However, for a real chemical potential, the complex determinant cannot be used as a probability weight. This is called the *sign problem*. Recently, some attempts based on extrapolation methods and stochastic quantization were proposed to circumvent the sign problem:

- *Reweighting method* [100]: measurements are performed at $\mu = 0$ and extrapolated to finite μ with help of reweighting or power series in μ/T.
- *Imaginary chemical potential* [26, 101]: the calculations are performed for imaginary μ and then analytically continued to real values.
- *Taylor expansion in* μ [102]: the quark determinant is expanded in power of μ/T and the resulting expressions are calculated term by term.

- *Complex Langevin*: this method is based on a stochastic quantization, which was introduced in [103–105], and recently some progress has been made for lattice gauge theory [22, 106].

If the numerical study of the effective theory at finite chemical potential will be carried out in the future, then the sign problem can be dealt with by using the reweighting method. In this method, configurations are generated at $\mu = 0$ with $\det[D(0)]$, i.e. a real probability weight, then these configurations are used to derive new weights describing a finite μ ensemble. See [48] for much more details on this subject in a more general context.

In this thesis we are not going to deal with the sign problem of the effective theory in terms of numerical methods, we focus instead on investigating the deconfinement critical point of the effective theory at zero μ.

5.3 Statistical error analysis

The estimation of statistical errors will be summarized briefly in this section. For more details see the extensive review in [3, 71, 96]. The estimation of the statistical errors in numerical lattice QCD seems to be a straightforward task. However, in practice, complicated fits and extrapolations might be involved in the procedure of evaluating physical quantities from the simulation data. Jackknife and bootstrap methods [107] are resampling techniques that simplify the error estimation of the calculated physical quantities significantly. The correctness of the resampling techniques can be established for most cases of interest including physical quantities considered in this thesis. However, we note that in some special cases, resampling techniques are incorrect. For example, generally, the jackknife method gives wrong results for the statistical error of the median of an observable [3].

Given a sample of measurements $\{A_n\}$ for $n = 1, \ldots, N$, traditionally the corresponding statistical error will be the standard deviation of the mean, which only works if the N measurements are independent. In this case, the statistical error would decrease as $1/\sqrt{N}$. However, measurements are extracted from successive configurations of a Markov chain, i.e. there exists a correlation between those measurements. Then, the reliability of the error estimation depends strongly on the inclusion of the autocorrelations. The autocorrelations are characterized by a quantity called the autocorrelation function

$$\Gamma_A(t) = \Gamma_A(-t) = \langle (A_n - \langle A \rangle)(A_{n+t} - \langle A \rangle) \rangle. \tag{5.18}$$

The uncertainty for an estimator for the variance of our data can be computed using correlated measurements as

$$\sigma_A = \sqrt{\frac{2\tau_{\mathrm{int}A}}{N(N-1)} \sum_{n=1}^{N} [A_n - \langle A \rangle]^2}. \tag{5.19}$$

Here $\tau_{\mathrm{int},A}$ is called the integrated autocorrelation time which has the approximated form [99]

$$\tau_{\mathrm{int},A} = \frac{1}{2} + \sum_{t=1}^{N} \frac{\Gamma_A(t)}{\Gamma_A(0)}. \tag{5.20}$$

We can see that our statistics is decreased by a factor $2\tau_{\mathrm{int},A}$, and we end up with only $N/2\tau_{\mathrm{int},A}$ uncorrelated measurements. The integrated autocorrelation can be computed as described in

for example [99], but in practice, the error estimation is made via resampling techniques such as the jackknife or the bootstrap method. The reason for this is that there are some cases where it is either inaccessible or too complicated to estimate the error using the direct method, for example, the cases of composite observables which will be discussed in more detail in chapter 6.2. Note that only the jackknife method will be discussed here, because it is used heavily for error estimations in this thesis, and we refer the readers to [71] for the discussion of the bootstrap method.

Jackknife error estimation

The jackknife method is a resampling method, i.e. for this method it is required to choose N_B independent sub-samples or bins out of the main sample $\{A_n\}$. Each bin contains $K = N/N_B$ individual measurements. With those bins, we can start with the computation of the block average

$$\bar{A}_{B,n} = \frac{1}{K}\sum_{i=1}^{K} A_{K(n-1)+i}, \quad \text{with} \quad n = 1, \ldots, N_B. \tag{5.21}$$

Next, the n-th jackknife estimate $\bar{A}_n^J$ is the average over all data in the sample except the point n and this step combines multiple bins into a larger sample, namely jackknife bins.

$$\bar{A}_n^J = \frac{1}{N_B - 1}\sum_{i\neq n}^{N_B} \hat{A}_{B,i}. \tag{5.22}$$

After averaging these jackknife bins, i.e. taking

$$\bar{A}^J = \frac{1}{N_B}\sum_{n=1}^{N_B} \bar{A}_n^J, \tag{5.23}$$

the covariance of the observable then reads

$$\sigma^2_{\bar{A}^J} = \frac{N_B - 1}{N_B}\sum_{n=1}^{N_B} (\bar{A}_n^J - \bar{A}^J)^2. \tag{5.24}$$

The relations in (5.23) and (5.24) can be generalized to the cases of composite observables like the susceptibility, skewness, or kurtosis of the Polyakov loop. For more details about how composite observables are treated see [108].

The choice of the binsize K will decide whether the jackknife error is reliable or not. A suitable check of the reliability is to plot the relative error of the quantity of interest against K, then at some value of K a plateau in dependence of the relative error appears. The presence of such a plateau indicates that the standard deviation starts to signal the correct behavior of uncorrelated samples.

Chapter 6

Critical phenomena of the effective theory

> ... for many physical quantities the perturbation series are sufficiently slowly convergent that one needs to calculate more than two terms in order to achieve accuracies of the order of 1 per cent.
>
> *by H. Eugene Standley in [109]*

The effective theory has been proved to be useful and can be applied to investigate full lattice QCD with heavy quarks, in particular at finite chemical potential. Recently, approaches have been developed to treat the effective theory analytically, which can serve as a cross-check for numerical methods, as well as provide insights into the mathematical and physical structure of the effective theory [29–32]. A method called linked cluster expansion gives a systematic treatment for certain limits of the effective theory such as the cold and dense regime or the SU(3) spin model [30,32], however, this expansion scheme can no longer be used to evaluate the improved effective theory with the logarithmic gauge action. Thus, we will apply another, more suitable expansion scheme called the high-temperature expansion to the improved effective theory. Furthermore, from a historical point of view, it should be pointed out that the high-temperature expansion has been a powerful tool for quantitative studies of statistical mechanics long before Monte-Carlo methods. In this work, the partition function and the susceptibility are computed up to the 13th power series in the power of the effective gauge coupling λ. While the 13th order is certainly not a very high order compared to series of spin systems like Ising or Heisenberg model, it is sufficiently large for a quantitative investigation. A series analysis method that combines the Padé and the Canterbury approximant, is used to analyze the resulting Polyakov loop susceptibility $\chi_L(\lambda, h_1, \bar{h}_1)$. A comparison to results obtained from recent simulations using flux representation [28] is carried out.

In the second part, we show results obtained in the $N_f \in \{1, 2\}$ effective theory with zero chemical potential at $N_t \in \{4, 6\}$ up to order $\mathcal{O}(\kappa^4)$ by using the standard Monte-Carlo simulation. This is a continuation of previous studies of the effective theory at $\mu = 0$ and an extension to our preliminary results [110]. After presenting the analysis of statistical sufficiency for our simulations, we give some comments on how to split simulation data into the appropriate number of bins, such that the statistical errors can be estimated correctly by the jackknife method. The critical endpoint, by which the first-order line of our effective theory terminates, is determined. Finally, a comparison to results obtained with full QCD using hopping expansion

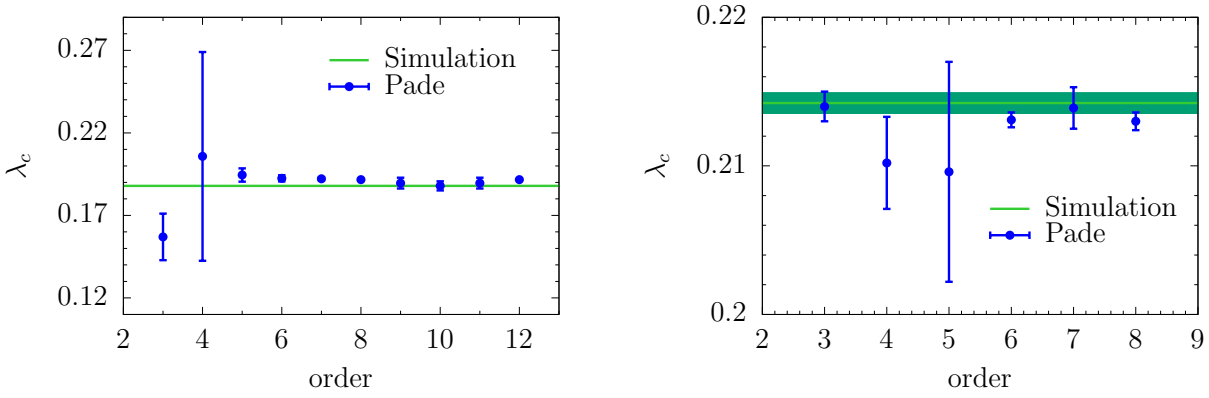

(a) SU(3) (b) SU(2)

Figure 6.1: Respective critical coupling λ_c for SU(3) and SU(2) to different orders of its corresponding susceptibility series.

for $N_t \in \{4, 6\}$, and with full QCD for $N_t = 6$ is considered.

6.1 Analytic results from series expansions

In chapter 4, we have shown a description of how the high-temperature expansion scheme adopted from statistical mechanics is applied to the effective theory. Because a large number of graphs and a large number of group integrals are involved in our computations, a fully computerized approach was implemented. The general multivariate power series of the Polyakov loop susceptibility χ_L is of the form

$$\chi_L = \sum_{i=0}^{L} \sum_{j=0}^{L} \sum_{k=0}^{L} c_{ijk} \lambda^i h_1^j \bar{h}_1^k. \tag{6.1}$$

We have obtained all terms contributing to the coefficients c_{ijk} for $L \leqslant 13$. In this section, we are going to explore the phase transitions of the heavy quark effective theory in $(\lambda, h_1, \bar{h}_1)$ parameter space. We start with the pure gauge effective theory, then the system with the presence of static quarks at zero, real and imaginary chemical potential are studied one after the other.

6.1.1 Yang-Mills theory

In the limit $\kappa \to 0$, we work with the nearest-neighbor pure gauge effective theory for $N_c = 2, 3$ which includes a logarithmic resummation given in eqn. (3.15)[1]. As mentioned in section 4.4, a standard method to extract information about criticality of single-variable functions from their available coefficients is the method of Padé approximants (PAs), in particular, the dlog

[1]The gauge group SU(2) has no anti-fundamental representation and consequently there is no complex conjugate Polyakov loop L^* in the SU(2) effective action.

Padé method:

$$\frac{\mathrm{d}}{\mathrm{d}\lambda}\log\chi_L \simeq [L/M] = \frac{P_L(\lambda)}{Q_M(\lambda)}, \tag{6.2}$$

where Padé approximants to the logarithmic derivative of χ_L then allows the critical parameter λ_c to be estimated as poles of the PA. In the case of SU(3), the resulting logarithmic derivative of the Polyakov loop susceptibility up to $\mathcal{O}(\lambda^{12})$ is

$$\begin{aligned}\mathrm{d}(\log\chi_L)/\mathrm{d}\lambda = 6 &+ 24\lambda + 126\lambda^2 + 768\lambda^3 + 3126\lambda^4 + 20736\lambda^5 \\ &+ 87198\lambda^6 + 552384\lambda^7 + 2440782\lambda^8 + 14984064\lambda^9 \\ &+ 68368086\lambda^{10} + 526709064\lambda^{11} + 2575039434\lambda^{12} + \mathcal{O}(\lambda^{13}).\end{aligned} \tag{6.3}$$

Because of the invariance properties of diagonal Padé approximants mentioned earlier, it is common practice to use the tridiagonal band of PAs $[N-1/N+1]$, $[N/N]$ and $[N+1/N-1]$. This is explained as follows: at order λ^M in eqn. (6.3) we take either three or two approximants depending on whether M is even or odd, for example, two PAs $([1/2],[2/1])$ are computed at order $M=3$ and three PAs $([1/3],[2/2],[3,1])$ at order $M=4$. For each of these approximants, we determine the poles λ_c and their residues γ_c. We then compute the mean value and quote as systematic error the maximum deviation between pairings $|\lambda_j - \lambda_i|$, where i,j label the approximants. We remark that this procedure is useful to observe the convergence of our power series, however, the best results are usually obtained from the diagonal Padé approximants $[N/N]$ of sufficiently high orders. Moreover, Padé approximants of a power series always produce poles, even in the case of the SU(3) effective pure gauge theory, where the transition is of first-order. In this case, they signal the end of the metastability region and thus are an upper bound on the true critical coupling. The same behavior has been observed in the q-state Potts model [111].

In fig. 6.1 (a) we show the critical coupling λ_c for $N_c = 3$ to each order of eqn. (6.3). The best estimate of λ_c is within 2% of the simulation result for the same model [27]. Even though the results have stabilized as the order increases, they slightly overshoot the true value, indicating that the series probes the end of the metastability region. The same computation for $N_c = 2$ is shown in fig. 6.1 (b). Here the estimate for $N_c = 2$ at order $\mathcal{O}(\lambda^8)$ already reaches the range of 1% from simulation data. It is easy to invert eqn. (3.18) to obtain the critical couplings β_c and compare with results of the four-dimensional Yang-Mills theory [112]. Fig. 6.2 (a) presents this for the SU(3) case, and a satisfactory convergence behavior of strong coupling series to the four-dimensional Yang-Mills result is observed.

In fig. 6.2 (b), the resulting critical exponents γ_c for $N_c = 2, 3$ associated with four different Padé approximants [4/4], [4/3], [3/3] and [3/5] are shown, respectively. The estimates for SU(2) accurately reproduce the values for the universality class of the three-dimensional Ising model, while the SU(3) case give values different from all known universality classes. This is consistent with the known behavior of the first-order phase transition, as well as with the Svetitsky-Yaffe conjecture [79].

6.1.2 Zero chemical potential

The effective theory aims to investigate the deconfinement transition of QCD with heavy quarks as a function of quark mass and chemical potential. First, we consider only the case of zero chemical potential, whose schematic phase structure is shown in the Columbia plot, see fig.

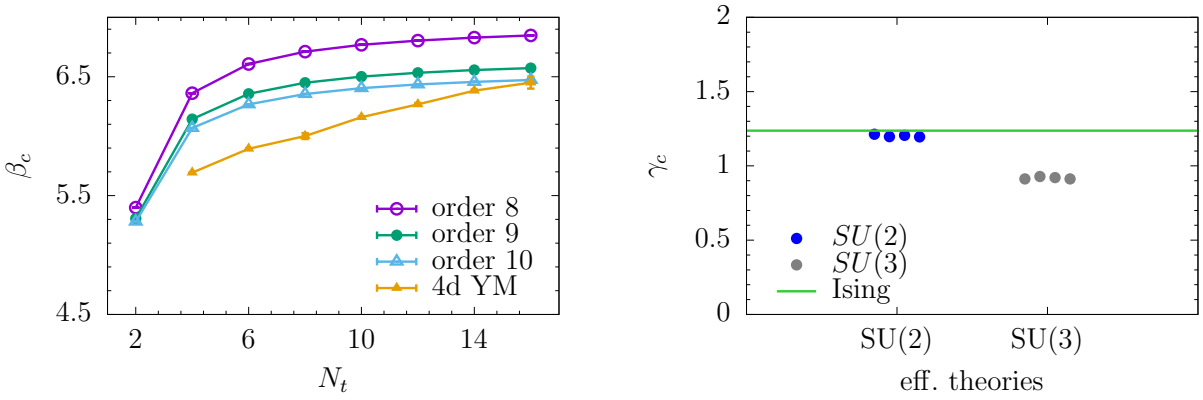

(a) Converted coupling β_c (b) Estimated residues for $N_c = 2, 3$

Figure 6.2: Left: Critical coupling β_c converted by (3.18). Right: Exponent γ for the SU(2) and SU(3) effective theory.

1.2. The phase diagram of full QCD in the heavy quark regime is described as follows. In the pure gauge limit, i.e. the upper right corner, the deconfinement transition is of first order. Dynamical quarks break the global Z_3 center symmetry of the QCD action for any N_f explicitly. As a consequence, as the quark masses decrease the phase transition becomes weaker until it terminates at a critical point. For still lighter quark masses the deconfinement transition is an analytic crossover. The effective theory also inherits this behavior, as is sketched in fig. 6.3 (b).

For one flavor case[2] $N_f = 1$ and $\mu = 0$, we have $h \equiv h_1 = \bar{h}_1$, and the effective theory then reduces to a system of two couplings (λ, h). This system possesses a first-order line with a weakening transition as h increases, and this line eventually terminates at a critical point. These expectations are based on the known results captured by the three-dimensional 3-state Potts model coupled to an external field [113, 114], which has the same symmetry breaking pattern. Similar to the argument for the SU(3) spin model given in [32], we note that for $h \neq 0$ the center symmetry of the effective theory is explicitly broken, and the (λ, h)-axes are misaligned with the temperature and magnetic field scaling axes of the effective Ising Hamiltonian governing the vicinity of the critical point. This situation of a first-order transition terminating in a critical point is the generic one of a liquid-gas transition. While the behavior of the system in the vicinity of the critical point is dictated by the universality class, the location of the transition in parameter space is not. Thus, our investigation will provide valuable insights into QCD. Localization of the critical heavy quark mass with full QCD has been studied numerically in [115], and with the effective theory in [28].

Before we proceed with the analytic attempt to study the phase transition of the effective theory, it should be pointed out that, unlike the SU(3) spin model where the specific heat observable is a well-defined quantity and can be used together with the susceptibility to locate the critical point of the system [32], the log-action of the improved effective theory prevents the specific heat observable to have a simple form, which does not signal the information of a phase transition. For this reason, we propose a more suitable approach described below.

[2]For simplicity we only consider the $N_f = 1$ case, however, it is quite straightforward to perform the same calculations for $N_f \geqslant 2$, since one only needs to change the power of the static quark determinant, while the expansion scheme to the log action remains unchanged.

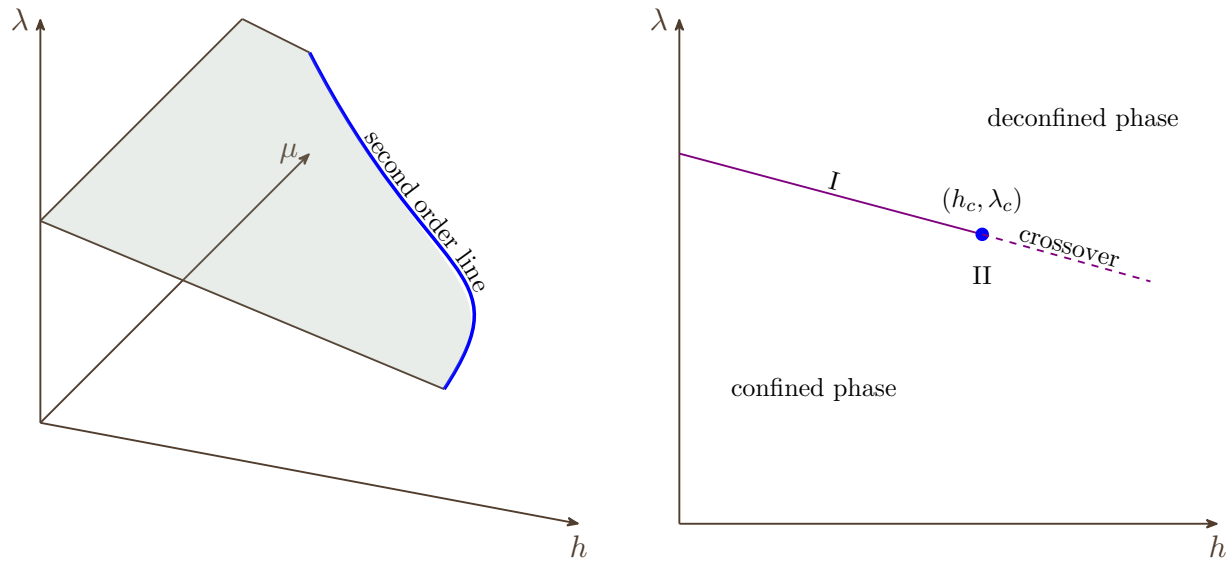

(a) Schematic 3d phase diagram

(b) Schematic phase diagram $\mu = 0$

Figure 6.3: Left: Schematic phase diagram of the effective theory in (λ, h, μ) parameter space. A surface of first-order transitions is bounded by a Z_2-second-order line beyond which the transitions are analytic crossover. Right: A schematic phase diagram for the effective theory corresponding to $\mu = 0$.

Before we proceed to a localization procedure of the critical endpoint with help of the new approach, a few points need to be clarified. First of all, both non-dlog Padé and dlog Padé approximants can be employed to determine the location of the phase transition, because they model the singular behavior of the full observables best at a second-order point. Second, to employ the Padé analysis for singular functions of two or more variables one must reduce the power series to a single variable, i.e. scanning over a variable and performing the Padé analysis on the other. For example, by fixing $h = 0.00073$, a value close to the endpoint, the singular of two series χ_L and $\mathrm{d}\log\chi_L$ can be found by solving their denominator $Q_6(\lambda)$ of the correspondent Padé approximant [6/6] for λ, respectively. Thus, we obtain

$$\lambda_c^{\chi_L} = 0.189282, \quad \lambda_c^{\mathrm{d}\log(\chi_L)} = 0.189456, \tag{6.4}$$

which agree within 0.09%. The result indicates that both series χ_L and $\mathrm{d}\log(\chi_L)$ are capable of determining the critical point. Fig. 6.4 shows the convergence of our results, and the [6/6] approximant to the $\mathcal{O}(\lambda^{12})$ series of χ_L and $\mathrm{d}\log\chi_L$, respectively. The phase transition is then accounted by a singularity in the approximant.

If we plot the phase transition estimated by the Padé and the Canterbury approximant in the (λ, h) parameter space separately, then it is easy to recognize that they can probe the phase boundary of the theory as well as the convergence of the series, not the critical endpoint. Similar behavior has also been observed in the SU(3) spin model. Analogous to the method used in [32], where the intersection points of poles in approximants to different observables can be taken as estimates for the location of the critical point, we realize that the critical endpoint can be determined by a combination of the Padé and Canterbury approximant. Here we argue that these methods construct different approximants, but those approximants are most sensitive to the second-order point and only there. Thus, we expect that they possess

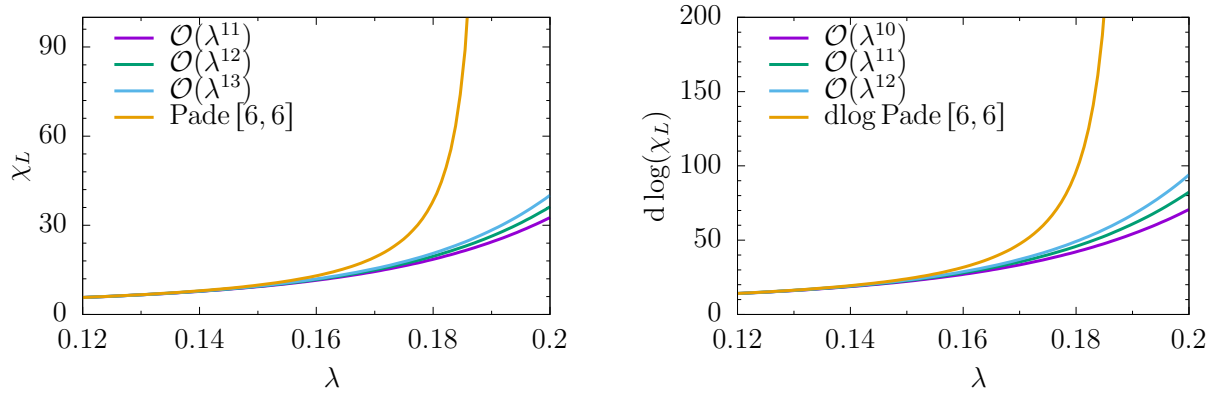

(a) Convergence of the susceptibility

(b) Convergence of the d log(χ_L) series

Figure 6.4: Left: Convergence of the susceptibility χ_L. Right: The convergence of the d log(χ_L) series in the parameter space (h, λ), both at $h = 0.00073$.

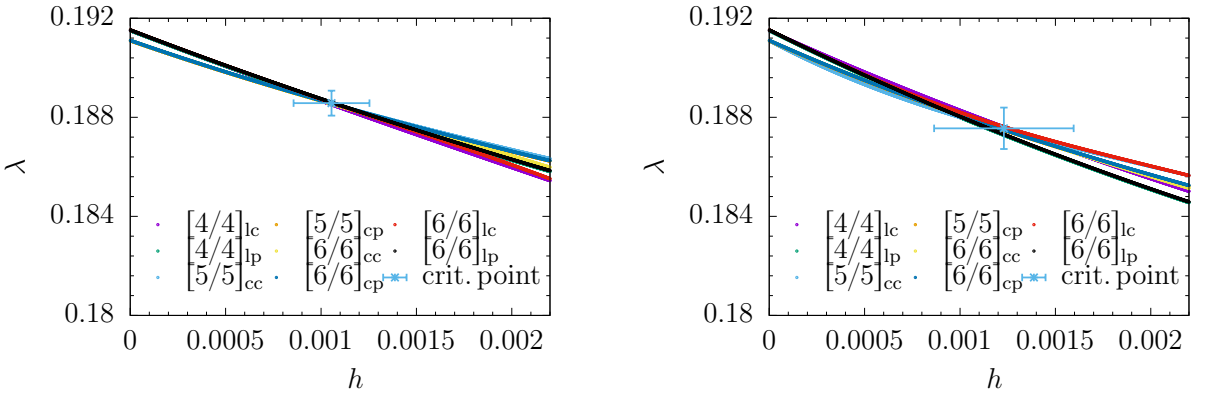

(a) $\mu = 0$

(b) $\mu = 0.75$

Figure 6.5: Critical points estimated from the high-temperature expansion at zero and finite chemical potential.

the same diverging behavior at this point.

At this stage, it is convenient to clarify our notations first before going into details of the series analysis. As one can see in tab. 6.1, there are several types of approximants coming from the Padé and Canterbury method for the χ_L and d log χ_L series. To keep track of those approximants, we use the following index notations: cp - Padé approximants for χ_L series, lp - Padé approximants for d log χ_L series, cc - Canterbury approximants for χ_L series, and lc - Canterbury approximants for d log χ_L series. While Padé approximants work astonishingly well for one-variable problems with a second-order transition as shown previously, the two-variable situation of the SU(3) effective theory with various types of transitions is more complicated. For instance, if we isolate the Padé approximants $[4/4]_{lp}$ and $[6/6]_{lp}$, they tend to pick up the rise of the d log χ_L series near the phase boundary, where the full series is known to be analytic, and are unable to clearly distinguish between orders of the phase transition or crossover behavior.

Fig. 6.5 (a) shows the estimates of the critical point at $\mu = 0$. The critical point is reproduced within 2% accuracy in λ and 40% in h. According to the arguments given above,

		$\mu = 0$		$\mu = 0.75$	
PA/CA	PA/CA	h_c	λ_c	h_c	λ_c
$[5/5]_{\mathrm{cp}}$	$[4/4]_{\mathrm{lp}}$	0.001118	0.188453	0.000868	0.188478
$[5/5]_{\mathrm{cp}}$	$[6/6]_{\mathrm{lp}}$	0.001220	0.188192	0.000908	0.188340
$[6/6]_{\mathrm{cp}}$	$[4/4]_{\mathrm{lp}}$	-	-	0.000806	0.188582
$[6/6]_{\mathrm{cp}}$	$[6/6]_{\mathrm{lp}}$	0.001170	0.188316	0.000868	0.188384
$[4/4]_{\mathrm{lc}}$	$[5/5]_{\mathrm{cp}}$	0.000998	0.188669	0.001596	0.186599
$[4/4]_{\mathrm{lc}}$	$[6/6]_{\mathrm{cp}}$	0.000969	0.188761	0.001548	0.186780
$[5/5]_{\mathrm{cc}}$	$[5/5]_{\mathrm{cp}}$	-	-	0.001229	0.187532
$[4/4]_{\mathrm{lc}}$	$[4/4]_{\mathrm{lp}}$	0.000396	0.190356	-	-
$[5/5]_{\mathrm{cc}}$	$[6/6]_{\mathrm{cp}}$	0.000936	0.188820	0.001239	0.187505
$[5/5]_{\mathrm{cc}}$	$[4/4]_{\mathrm{lp}}$	0.001077	0.188519	0.001019	0.187941
$[5/5]_{\mathrm{cc}}$	$[6/6]_{\mathrm{lp}}$	0.001160	0.188341	0.001037	0.187909
$[6/6]_{\mathrm{cc}}$	$[5/5]_{\mathrm{cp}}$	0.001025	0.188608	0.001559	0.186676
$[6/6]_{\mathrm{cc}}$	$[6/6]_{\mathrm{cp}}$	-	-	0.001370	0.187148
$[6/6]_{\mathrm{cc}}$	$[4/4]_{\mathrm{lp}}$	0.001156	0.188326	0.000786	0.188684
$[6/6]_{\mathrm{cc}}$	$[6/6]_{\mathrm{lp}}$	0.001254	0.188098	0.000873	0.188448
$[6/6]_{\mathrm{lc}}$	$[5/5]_{\mathrm{cp}}$	0.001149	0.188340	-	-
$[6/6]_{\mathrm{lc}}$	$[6/6]_{\mathrm{cp}}$	0.001130	0.188405	-	-
$[6/6]_{\mathrm{lc}}$	$[4/4]_{\mathrm{lp}}$	0.001311	0.187919	-	-
$[5/5]_{\mathrm{cc}}$	$[6/6]_{\mathrm{cc}}$	0.000790	0.189144	0.001254	0.187448
$[5/5]_{\mathrm{cc}}$	$[4/4]_{\mathrm{lc}}$	0.000958	0.188779	0.001393	0.187206
$[5/5]_{\mathrm{cc}}$	$[6/6]_{\mathrm{lc}}$	0.001119	0.188428	0.002197	0.185686
$[6/6]_{\mathrm{cc}}$	$[4/4]_{\mathrm{lc}}$	0.000991	0.188690	0.001603	0.186560
$[6/6]_{\mathrm{cc}}$	$[6/6]_{\mathrm{lc}}$	0.001180	0.188274	-	-
$[6/6]_{\mathrm{lc}}$	$[4/4]_{\mathrm{lp}}$	-	-	0.001218	0.187665

Table 6.1: Intersection points of the poles in the Padé and Cantebury approximants to χ_L and $\mathrm{d}\log\chi_L$.

		ET (analytic)		ET (simulation) [28]		hopp. exp.-QCD [115]
N_f	N_t	M_c/T	κ_c	M_c/T	κ_c	κ_c
1	4	6.85(19)	0.088(4)	7.22(5)	0.0822(11)	0.0783(12)
1	6	-	0.148(4)	-	0.1404(11)	0.1525(34)

Table 6.2: Location of the critical point for $\mu = 0$ and $N_f = 1, N_t = 4, 6$. The first two columns report our results from series expansion, the next four columns compare with those from simulation and hopping expanded QCD.

these need to agree at a second-order transition and only there, so we take their intersections as estimates for the location of the critical point. To obtain an error estimate, we compute the standard deviation of all intersections of diagonal Padé and Canterbury approximants listed in tab. 6.1. On average, i.e. including results at $\mu \neq 0$, the predictions from the series approach have an averaged relative error of about 1% in λ_c and about 30% in h_c. Presumably, the larger error on the latter variables is due to the flatness of the critical line in the phase diagram, so it takes more accuracy meaning higher orders to resolve changes in those directions. Within error bars, the predicted critical points agree with the numerical determined ones, so the estimate of the systematic error is realistic.

Our estimated critical point at $\mu = 0$ is

$$(\lambda_c = 0.188572(50), h_c = 0.00106(20)), \tag{6.5}$$

which can be easily converted into those of the couplings (β_c, κ_c) using (3.18) and (3.61). In order to compare with previous work, we approximate M_c/T with the relation that is valid for heavy quarks to leading order in the hopping expansion [82],

$$\exp\left(-\frac{M}{T}\right) \simeq \frac{h}{N_f}. \tag{6.6}$$

The results are listed in tab. 6.2 and are in reasonable agreement with the corresponding ones from simulations of the four-dimensional QCD with Wilson fermions at $N_f = 1, N_t = 4$ [115]. In the case of pure gauge theory, the critical effective couplings can be mapped to those of QCD for any N_t, thus providing predictions for larger N_t which have not yet been simulated in four-dimensional full QCD. However, it was checked in [28], that $N_t = 6$ is the finest thermal lattice for which κ_c is consistent meaning that it is still significantly smaller than the chiral critical hopping parameter κ_{ch} evaluated at the same gauge coupling since we are expanding around infinite quark masses.

6.1.3 Real and imaginary chemical potential

Let us turn now to the investigation of the deconfinement transition at finite baryon density. For $\mu \neq 0$, we get $h_1 \neq \bar{h}_1$, then the full parameter space of the effective theory $(\lambda, h_1, \bar{h}_1)$ must be considered. That means the diagram in fig. 6.3 (b) turns into a three-dimensional diagram with a surface of first-order phase transitions terminating in a critical line as illustrated in fig. 6.3 (a). Since the change of the critical quark mass with chemical potential is in our main focus, it is convenient to map out the critical line by fixing different chemical potentials and

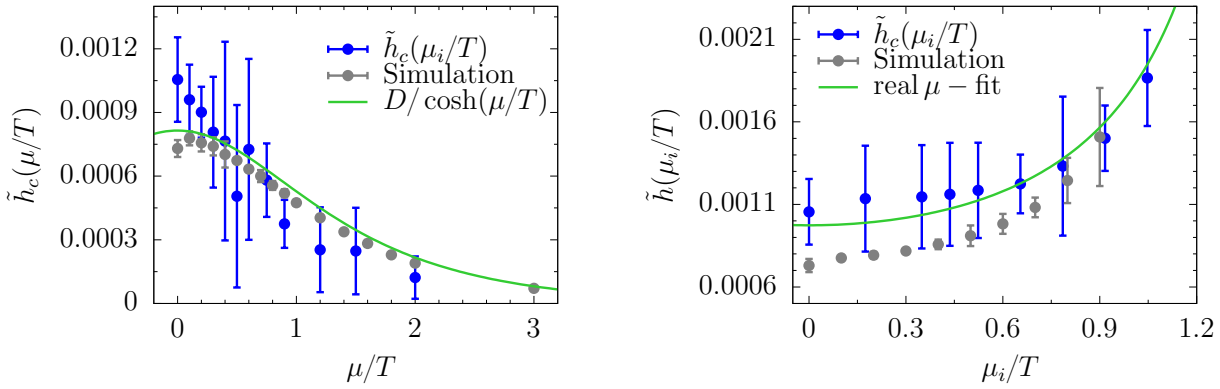

(a) Real chemical potential

(b) Imaginary chemical potential

Figure 6.6: Critical coupling $\tilde{h}_c$ for real and imaginary chemical potential.

then scan for the critical hopping parameter κ. A new parameter defined as

$$\tilde{h} = he^{-\mu/T} \left(\simeq (2\kappa)^{N_t} \text{ to leading order in } \kappa\right) \tag{6.7}$$

is more appropriate for that purpose. With the new parameter $\tilde{h}$, the parameter space of the effective theory at finite chemical potential becomes $(\lambda, \tilde{h}, \mu/T)$. We perform similar calculations to the case $\mu = 0$ using the chemical potential range $\mu/T \in \{0.1, \ldots, 2.0\}$ to determine the corresponding (h_c, λ_c). For example, for $\mu/T = 0.75$ the critical point $(h_c, \lambda_c) = (0.00123(37), 0.18756(84))$ is obtained from averaging intersection points of different approximants, see fig. 6.5 (b). It is then straightforward to convert h_c with the corresponding values of μ/T into $\tilde{h}_c$ and plot it against μ/T. The analytic and the simulation data taken from [28] are shown in fig. 6.7 (a). Our analytic results are in reasonable agreement with those from simulations, and it is clear that the important trend of the critical line is captured by the series expansion method. As one can see that the error bars of the analytic results are quite large, which can possibly be explained using the fact that our 13th power series is not very high compared to the series of Ising model, for example in [116], and as mentioned earlier the flatness of the critical line in the phase diagram might affect the error estimates. To fit our data we use the fitting function

$$\tilde{h}_c(\mu/T) = \frac{D}{\cosh(\mu/T)}, \tag{6.8}$$

which has been used in [28]. This function was derived by expanding the critical lambda around the pure gauge limit $(\lambda, \tilde{h}, \mu/T) = (\lambda, 0, 0)$ and using the fact that the critical line of the effective theory depends only weakly on μ/T. Our fit of all $\mu > 0$ data with one parameter D performs well, yielding $D = 0.00081(6)$ with $\chi^2/\text{d.o.f} = 0.76$. The corresponding critical $h_c(\mu = 0) = D$ is improved when all $\mu > 0$ data is used, and a compatible agreement with the fit result of $D = 0.00075(1)$ with $\mu = 0$ from simulation.

Let us conclude this section with the study of the effective theory at imaginary chemical potential and its relations to the Robert-Weiss symmetry. For imaginary chemical potential $\mu = i\mu_i, \mu_i \in \mathbb{R}$, the Dirac operator is γ_5-hermitian and the determinant is real, which allows application of importance sampling techniques. The QCD phase transitions and its critical sur-

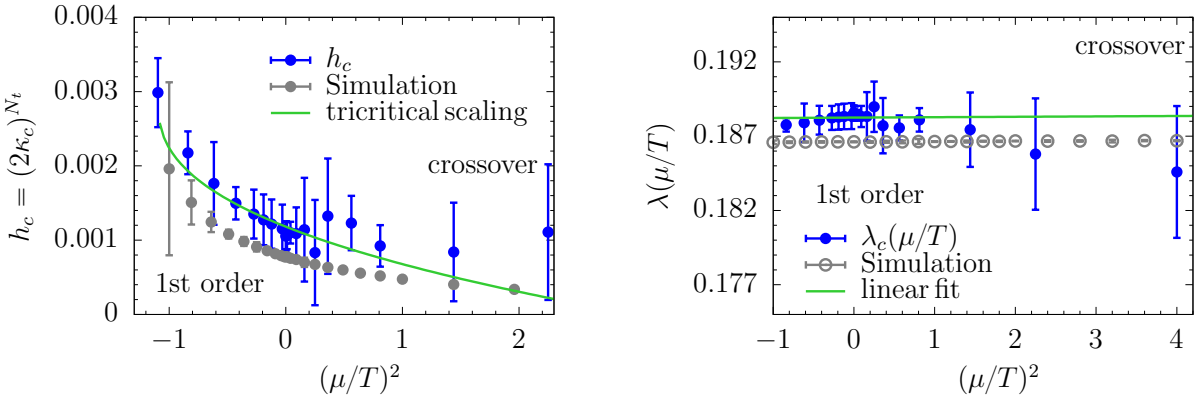

(a) $h - (\mu/T)^2$ analytic continuation

(b) $\lambda - (\mu/T)^2$ analytic continuation

Figure 6.7: Critical couplings h_c and λ_c for real and imaginary chemical potential.

faces possess an analytic continuation between real and imaginary chemical potentials, where measurements are carried out at various values of the purely imaginary chemical potential and then analytically continue to a real chemical potential with the use of some ansatz function [16, 101, 117, 118]. The continued results are affected significantly by the choice of this ansatz function, therefore one needs to choose it carefully. It has been found that for heavy quark masses the form of the deconfinement critical surface is determined by tricritical scaling and terminates in a tricritical line at $\mu_i/T = \pi/3$ [119] which sets the boundary to an adjacent Z_3 center-sector of the partition function [120].

The center symmetry and its breaking in QCD are correctly reflected by the effective theory. Indeed, for purely imaginary chemical potential the effective action (4.27) is also real and thus does not suffer from a sign problem. In addition, the effective partition function is symmetric by reflection in μ, which allows an expansion for the free energy density or the pressure in powers of μ^2, and it is periodic in μ_i/T with a period of $2\pi/N_c$, implying the Roberge-Weiss symmetry shared by QCD [119],

$$Z(\lambda, h, i\mu_i) = Z(\lambda, h, i\mu_i + i2\pi n/3), \quad N_c = 3, \quad n = 0, 1, 2, \ldots, \tag{6.9}$$

i.e., center transformations are equivalent to shifts in imaginary chemical potential. Next, we are interested in the continuation of the critical quark masses, i.e. the deconfinement critical surface, from $\mu = 0$ to $\mu/T = i\pi/3$. We follow the same approach as for real chemical potential with the imaginal chemical potential range $\mu_i/T = 0.1 - \pi/3$, followed by determinations of the pseudo-critical and critical couplings. Unlike the situation of simulation results where numerical difficulties increase as μ_i approaches the boundary to the next center symmetry sector [28], our controlled errors are valid up to $\mu_i/T = \pi/3$. This is because the analytic results are directly obtained from the thermodynamic limit, where one does not have to construct a better finite size analysis and to demand large volumes for dealing with a crossover between three-dimensional Ising and tricritical scaling as moving along the critical line towards the Roberge-Weiss tricritical point, see fig. 6.8 (a).

As the values of μ_i increased, we get a shift towards higher values in $\tilde{h}_c(\mu_i/T)$ by the endpoint of the corresponding first-order line. The resulting critical line is shown in fig. 6.6 (b), where an analytic continuation of the real-μ fit eqn. (6.8) to imaginary chemical potential has been performed, and the data has been well described. For this fit, we obtain $D = 0.00097(2)$,

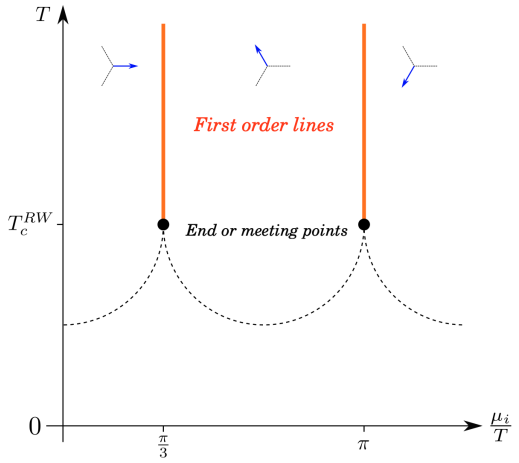

(a) Robert-Weiss transition

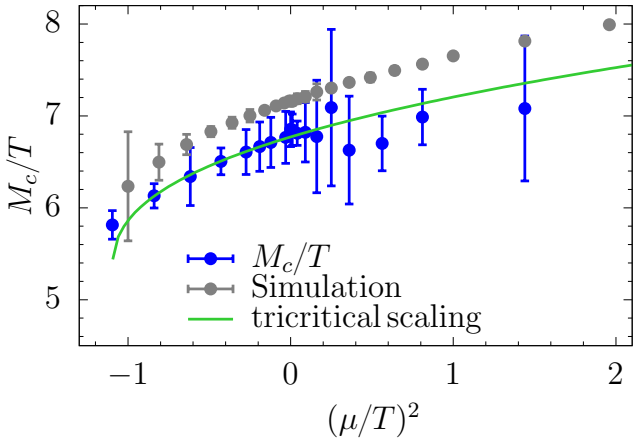

(b) $M_c/T - (\mu/T)^2$ analytic continuation

Figure 6.8: Left: QCD phase diagram in the $T - \mu_i$ plane. The dashed line depicts the chiral/deconfinement transition whose nature depends on the quark mass. The orange lines represent the Robert-Weiss (RW) transitions. The black dots, where the first-order lines terminate, can be first-order triple points, tricritical points or second-order endpoints [121]. Right: Critical M_c/T for $N_f = 1$ at both real and imaginary chemical potential.

χ^2/d.o.f = 0.96. Furthermore, we may present real and imaginary chemical potential data together and plot h_c and λ_c against μ^2/T^2 as shown in fig. 6.7. For $\mu = 0$, the critical points $\lambda_c(\tilde{h}_c(\mu/T), \mu/T)$ can be found again by evaluating our series. It is also easy to see from fig. 6.7 (b), the resulting transition line $\lambda_c(\tilde{h}_c(\mu/T), \mu/T)$ shows only weak dependence on μ/T. A linear fit with χ^2/d.o.f = 0.26 yields that the critical points vary around $\lambda_c = 0.18825(9)$ which is $< 1\%$ in comparison with simulation results. Interestingly, the weak dependence was also observed in the three-dimensional Potts model, where the spin coupling as a function of the external fields is nearly constant along the critical line [114]. A possible explanation for this weak dependence is that the center symmetric couplings are suppressed since they always couple to pairs of L and L^*.

It was demonstrated in [119] for the Potts model and strong coupling QCD that the critical quark mass at imaginary chemical potential is governed by tricritical scaling, with a scaling region extending all the way to real μ. We thus attempt the corresponding two-parameter fit to tricritical scaling of both h_c and M_c/T with

$$h_c\left(\frac{\mu^2}{T^2}\right) = h_{\text{tric}} + K_1\left[\left(\frac{\pi}{3}\right)^2 + \left(\frac{\mu}{T}\right)^2\right]^{2/5}, \tag{6.10}$$

$$\frac{M_c}{T}\left(\frac{\mu^2}{T^2}\right) = \frac{M_{\text{tric}}}{T} + K_2\left[\left(\frac{\pi}{3}\right)^2 + \left(\frac{\mu}{T}\right)^2\right]^{2/5}, \tag{6.11}$$

which are plotted in fig. 6.7 (a) and 6.8 (b), respectively. While the h_c data can be fitted for the full range of μ, we are allowed only to fit the region $\mu^2 < 0$ for M_c/T because of the eqn.

(6.6). We then obtain

$$h_{\text{tric}} = 0.00288(17), \qquad K_1 = -0.0016(2), \qquad \chi^2/\text{d.o.f} = 0.270, \tag{6.12}$$

$$M_{\text{tric}}/T = 5.31(2), \qquad K_2 = 1.41(2), \qquad \chi^2/\text{d.o.f} = 0.002. \tag{6.13}$$

Remarkably, for M_c/T the scaling function correctly describes the data up to large real chemical potentials $\mu < 2$, and in a reasonable agreement with the simulation data, where $M_{\text{tric}}/T = 5.56(3)$ and $K_2 = 1.55(3)$ [28].

Our analysis described for real chemical potential has been repeated for a range of parameter values and how the location of the critical endpoint changes as a function of h and μ has been also mapped out. Thus the complete phase diagram of the theory is determined, as shown in fig. 6.7 and 6.8 (b). For every choice of $(\tilde{h}, \mu)$ there is a $\lambda_c(\tilde{h}, \mu)$ marking the phase boundary for center symmetry transition. The figure shows the second-order line separating the parameter region with first-order transitions from that of smooth crossovers, i.e., it is a projection into the transition surface of fig. 6.3 (a). The expected analyticity of the critical line around $\mu = 0$ is observed, and at this moderate accuracy, the entire range of chemical potentials is well described by fitting a next-to-leading-order Taylor expansion in μ^2 about zero. Note that at $-\mu^2 = (\pi/3)^2 = (1.05)^2$ the boundary to the neighboring center sector is crossed, beyond which the phase diagram is dictated by the Roberge-Weiss symmetry. This point is marked by a cusp, where two critical lines from neighboring center sectors meet, and which thus is tricritical in all theories featuring this center symmetry, such as the Z_3 Potts model or QCD [119]. As a consequence, the critical line is leaving this point with a known tricritical exponent, and a fit to this functional form also described our results over the whole range.

Lastly, we note that the parameter range $0.001 < h < 0.004$ corresponds to a situation, where there is a crossover for $\mu = 0$ but a critical point followed by a first-order transition beyond some imaginary μ_c, as is often expected for QCD and read μ. We conclude that the computational technique and analysis examined here are in principle able to handle such a situation.

6.2 Numerical results

In this section, we present results updating previous studies of three-dimensional effective theories at zero chemical potential in the heavy quark regime using standard Monte Carlo simulations. We calculate the deconfinement phase transition and its critical endpoint with $N_f \in \{1, 2\}$, $N_t \in \{4, 6\}$ for different truncations of the three-dimensional effective theory up to order $\mathcal{O}(\kappa^4)$ in the hopping parameter. The measurement of the Polyakov loop, the Polyakov loop susceptibility, the kurtosis, and the skewness are shown as a function of the corresponding effective couplings, i.e. h_1, κ, u, and λ. We follow closely the strategy used to locate the critical endpoint presented in [16, 28, 122]. Finally, a comparison to results obtained from simulations of four-dimensional QCD after hopping expansion, as well as with full QCD simulations for $N_t = 6$ is carried out.

6.2.1 Observables and finite size scalings

As described before in subsection 2.5.2, for any finite volume the expectation of the Polyakov loop $\langle L \rangle$ vanishes for adequately long simulations, therefore one often performs an analysis on $\langle |L| \rangle$ instead, which also agrees with $|\langle L \rangle|$ in the thermodynamics limit. Let us define the

primary observable that is used throughout the study of the deconfinement phase transition of the effective theory[3]

$$\mathcal{O} = \frac{1}{N_s^3} \sum_{\vec{n}} |L_{\vec{n}}|. \tag{6.14}$$

A true non-analytic phase transition can only exist in the infinite volume limit. In order to extract this transition from simulations performed at finite volumes, an extrapolation with a finite size scaling is needed. One uses two quantities called skewness and kurtosis [124] which can be constructed from our primary observable $\mathcal{O}$ as follows

$$B_3(\mathcal{O}) = \frac{\langle (\mathcal{O} - \langle \mathcal{O} \rangle)^3 \rangle}{\langle (\mathcal{O} - \langle \mathcal{O} \rangle)^2 \rangle^{3/2}}, \quad B_4(\mathcal{O}) = \frac{\langle (\mathcal{O} - \langle \mathcal{O} \rangle)^4 \rangle}{\langle (\mathcal{O} - \langle \mathcal{O} \rangle)^2 \rangle^2}. \tag{6.15}$$

The critical value of B_4 in the thermodynamic limit for different orders of the phase transition is given in tab. 6.3. The leading finite size corrections are obtained by performing Taylor expansion on the kurtosis

$$B_4(\mathcal{O}, \kappa, N_s) = B_4(\mathcal{O}, \kappa_c, \infty) + a_1(\kappa - \kappa_c) N_s^{1/\nu} + \dots . \tag{6.16}$$

The formula (6.16) is used to fit the data on different volumes. Here we consider only the linear term of the Taylor expansion which is sufficient for the analysis of the effective theory due to the reasonable range of simulated points around the critical point. The quality of the fit is reliable meaning B_4 and ν take their universal value if the simulated volumes are not too small and if the errors on the kurtosis are not too large [108]. In addition, the skewness B_3 is a measure for an asymmetry of the probability distribution of our observable. As our couplings approach the phase transition, the shape of the distribution becomes asymmetric left or asymmetric right, depending on the side of the phase transition. This indicates that the skewness will take a positive value on one side and a negative on the other, and it has to cross zero at the phase transition where the probability distribution is symmetric around its mean value. We note that one can also extract information on the location of the phase transition from the peak of the susceptibility with the following scaling behavior [125]

$$\chi(\mathcal{O}) = N_s^{\gamma/\nu} f(k N_s^{1/\nu}). \tag{6.17}$$

Here f is a universal scaling function, $k = \kappa - \kappa_c$ denotes the reduced coupling and γ, ν are critical exponents given in tab. 6.3. The description of this method is as follows: we fix the critical exponents γ, ν to the correct universal values, then measure $\chi / N_s^{\gamma/\nu}$ with multiple spatial volumes. The curves should then collapse when plotted against $kN^{1/\nu}$ (collapse plot), and finally, the values for ν determined from the kurtosis can be checked. The main disadvantage of this method is that sometimes it is difficult to estimate by eye the nature of the phase transition due to the similarity of the collapse plots [125]. Fortunately, a quantitative measure for the quality of finite size scaling plots is developed, which significantly reduces the subjective judgment required for fitting [108, 126].

[3] There is another way to define $\langle |L| \rangle$ by taking the absolute value after summing over the spatial lattice, which also gives compatible results to our convention [123].

	Crossover	first-order triple	Tricritical	3D Ising
B_4	3	1.5	2	1.604
ν	-	1/3	1/2	0.6301(4)
γ	-	1	1	1.2372(5)

Table 6.3: Critical values for ν, γ and B_4 for different phase transitions [127].

6.2.2 The analysis of the data

Let us briefly discuss the sufficiency of statistics in Monte-Carlo simulations. It is not straightforward to see whether simulations have enough statistics or not. Of course, the higher statistics they have the better, and the smaller will be the errors in the quantities measured. There are several methods for checking this, the readers are referred to [108] for more detail. First, the standard way is to measure the integrated autocorrelation τ_{int} which is related directly to the number of independent events collected. However, the data analysis with this method might become a nontrivial task if some non-linear procedure involves, where complicated fits and extrapolations are required. In this work, we decide the statistics sufficiency of a simulation by running several Monte Carlo simulations until the value of the considered observable is statistically the same on the different Markov chains. In fig. 6.9 we present the result for four simulations with the same physical setup, but different seeds of the pseudo-random number generator. The 100% of our statistics for this run corresponds to 1.5 million measurements. An overview of the statistics accumulated in all the simulations can be found in tab. 6.5 and 6.6. Followed [108], when all of the values of the kurtosis $B_4(|L|)$ of different seeds are compatible within three standard deviations, we can estimate the range of statistics for a simulation[4].

In section 5.3 we have discussed how to use the jackknife method for estimating the error of a composite observable. However, one important remaining question is how to choose the number of bins that the initial time series is split into. As stated in 5.3, the choice of bins is determined by a plot of relative errors of the quantity of interest against the binsize $K = N/N_B$, by which at some value of K a plateau in dependence of the relative error appears, indicating the chosen bins are practically uncorrelated. We present two examples of this behavior for the $N_f = 2$ $\mathcal{O}(\kappa^2)$ effective theory at $N_t = 6$ and $N_s = 24$ in fig. 6.10, one for a simulation far away from the phase transition and one for a simulation near the phase transition, respectively. Here the statistics for both runs is again 1.5 million measurements. From these two plots, one can easily observe that for the simulation far away from the phase transition a small binsize of $\sim$2000 already gives a reliable error estimation. On the other hand, near the phase transition, a significantly larger binsize of $\sim$20000 is required in order to obtain a reliable error. This is also expected since near the phase transition the correlation length tends to go to infinity in the thermodynamic limit. We emphasize that with the jackknife method each quantity (the mean, susceptibility, skewness, and kurtosis) has in principle a different binsize, which has to be chosen accordingly.

[4]There is an exception for the effective theory at order $\mathcal{O}(\kappa^4)$ where the statistics of the simulation in the volume $N_s = 20$ is quite small because the running time for $\mathcal{O}(\kappa^4)$ increases significantly. We will come back to this point later.

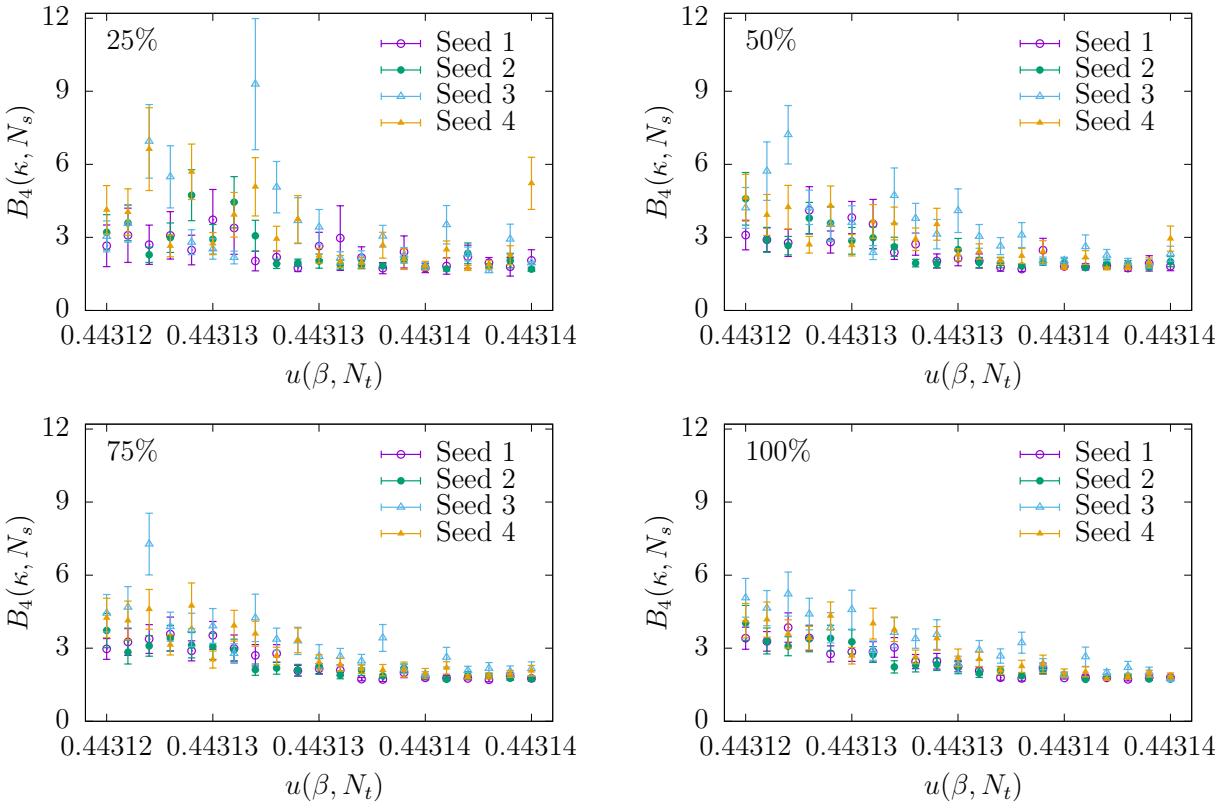

Figure 6.9: Successive analysis of the kurtosis measurements at $\kappa = 0.140$ on $N_t = 6, N_s = 20$ of the $N_f = 1$ $\mathcal{O}(\kappa^2)$ effective theory.

6.2.3 Discussion of the results

As was mentioned in the introduction, a numerical investigation of the effective theory at zero chemical potential with different orders in the hopping parameter is our main focus. The absence of the chemical potential leads to a real effective action to which standard Monte Carlo methods can be employed. According to (3.16), (3.29), (3.69) and (3.56), the effective action associated with different orders of κ are summarized as follows

$$S_{\mathrm{LO}} = S_{G,\mathrm{eff}} + S_0, \tag{6.18}$$

$$S_{\mathrm{NLO}} = S_{G,\mathrm{eff}} + S_0 + S_2, \tag{6.19}$$

$$S_{\mathrm{NNLO}} = S_{G,\mathrm{eff}} + S_0 + S_2 + S_4. \tag{6.20}$$

Here $S_{G,\mathrm{eff}}$, S_0, S_2 and S_4 are the effective pure gauge, the static quark, the $\mathcal{O}(\kappa^2)$ and the $\mathcal{O}(\kappa^4)$ effective action, respectively. The list of chosen values for the running parameters in our simulations for $N_f = 1, 2$ are reported in tab. 6.5 and 6.6, respectively. We present the results of the critical endpoint determined by our numerical simulations. First, as a cross-check the validity of our results in the leading order effective theory S_{LO} is presented. This effective theory has been studied numerically in [28], and analytically by means of the series expansion method shown in section 6.1. We note that the steps in determining the critical endpoint will be used for all possible orders of the effective theory.

To find the location of the critical deconfinement endpoint where the first-order transition

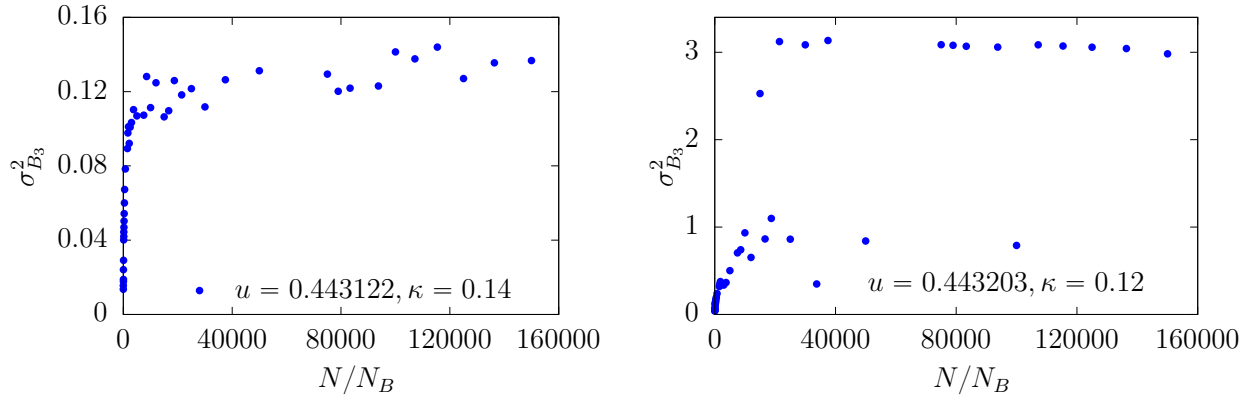

Figure 6.10: The respective estimates for variance from jackknife sampling for increasing binsize far (left) and near (right) the phase transition.

line terminates, a finite size scaling analysis as described above must be performed. In the vicinity of the critical point, the behavior of the system is dictated by its universality class which is characterized by the mechanism of symmetry breaking. The symmetry group that involves is the Z_3 symmetry. For the pure gauge theory, the deconfinement transition is of first-order, and the phase transition was found to occur at $\lambda_c = 0.187885(30)$ [27]. For $\lambda > \lambda_c$, the Z_3 symmetry is spontaneously broken, i.e. three distinct deconfined phases coexist. The presence of dynamical quarks then breaks the global Z_3 symmetry of the effective action explicitly. It leads to a vanishing of the first-order deconfinement transition at a critical endpoint for sufficient small quark masses. For still lighter quarks the transition becomes an analytic crossover.

To determine the phase diagram fig. 6.3 (b), we follow a two-step procedure. First, we determine the phase boundary, i.e. the pseudo-critical line $\lambda_{pc}(h_1)$ in the two-coupling space of the effective theory. In the second step, using dedicated finite size scaling analyses, we determine the order of the transition along that line, and in particular the location (λ_c, h_{1c}) of the critical point. To accomplish the first task, one needs to fix the external field variable to the values $h_1 \in \{0.0004, \ldots, 0.0012\}$ on lattice sizes $N_s = 16, 24, 32$, and then scan for the corresponding pseudo-critical coupling λ_{pc}. As indicators for the phase boundary, we use zeros of skewness B_3 and minimums of Binder cumulants or kurtosis B_4 constructed from the measurements of the Polyakov loop. For example, the behavior near a phase transition of the Polyakov loop and its composite observables associated with the S_{NLO} action are shown in fig. 6.11. One can extrapolate these to infinite volume using

$$\lambda_{pc}(h_1, N_s) = \lambda_{pc}(h) + c_1(h_1)/N_s^{\alpha}. \tag{6.21}$$

From the minima of the kurtosis $B_4(\mathcal{O})$ and the extrapolation of these along with those of other observables. This results in the pseudo-critical line shown in fig. 6.12 (a) which is well described by a linear fit due to a small magnitude of h_1 and the argument given in [113] that the line of first order phase transitions $\lambda(h_1)$ is determined by the condition that the free energy densities of the disordered (confined) phase and ordered (deconfined) phase are equal, i.e., $f_c(\lambda, h_1) = f_d(\lambda, h)$. Expanding both sides about the pure gauge transition, $(\lambda_0, h = 0)$,

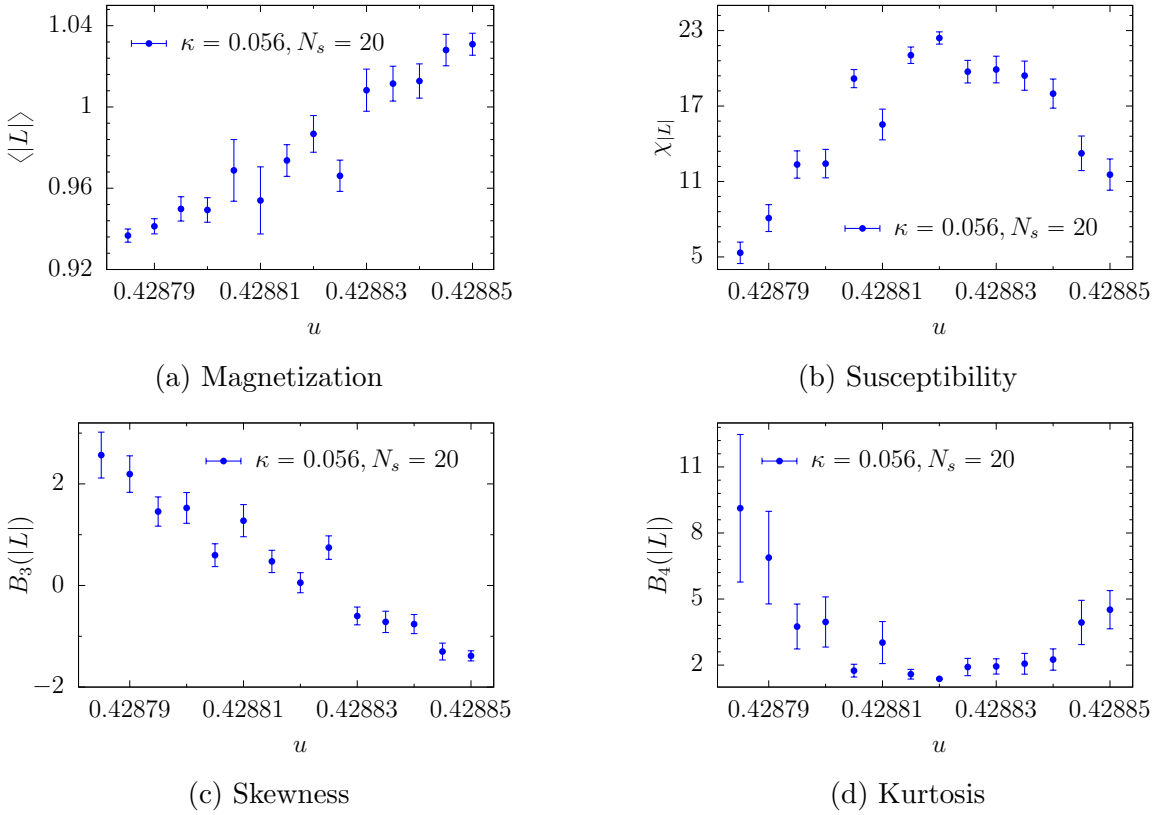

(a) Magnetization

(b) Susceptibility

(c) Skewness

(d) Kurtosis

Figure 6.11: Magnetization, susceptibility, skewness and kurtosis for the $\mathcal{O}(\kappa^2)$ effective theory at $\kappa = 0.56, N_f = 2,\ N_t = 6, N_s = 20$.

and noting that $\partial_h f_c = \langle |L| \rangle = 0$ in zero external field, we obtain

$$\lambda_{pc}(h_1) = \lambda_0 - a_1 h_1, \qquad a_1 = \left. \frac{\partial_h f_d}{\partial_\lambda (f_c - f_d)} \right|_{(\lambda_0, 0)} . \tag{6.22}$$

The χ^2/d.o.f value of the fit to the data given in fig. 6.12 (a) is 0.54, indicating a good fit quality. This fit yields

$$\lambda_0 = 0.188010(28), \qquad a_1 = 1.71(3), \tag{6.23}$$

which is in excellent agreement with the results obtained in [28].

In general, the investigation procedure is the same for the higher-order effective theory. However, because of the inclusion of the gauge corrections in the effective couplings, where the temporal extent involves, see eqn. (3.61)-(3.66), for practical reasons, the running parameters are now chosen to be u and κ. By employing the same analysis to the effective theory with higher corrections, the pseudo-critical line $u_{pc}(\kappa)$ can be mapped out, and subsequently, its critical point (u_c, κ_c) is also located by using the same finite size scaling analysis. The pseudo-critical line is found by fixing values of κ and performing a u-scan at $N_s = 16, 20, 24$, identifying the maximum of the susceptibility $\chi_{|L|}$ and the minimum of the kurtosis B_4. Result of $N_s = 24$ and $N_f = 1$ is shown in fig. 6.12 (b). Due to the smallness of κ at $N_t = 4$, as shown in [113]

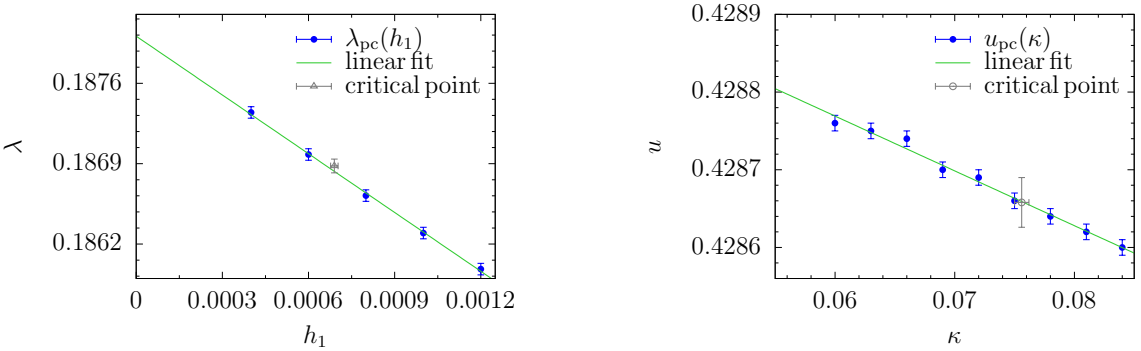

(a) $S_G^{\text{eff}} + S_0, N_f = 1$

(b) $S_G^{\text{eff}} + S_0 + S_2, N_f = 1, N_t = 4$

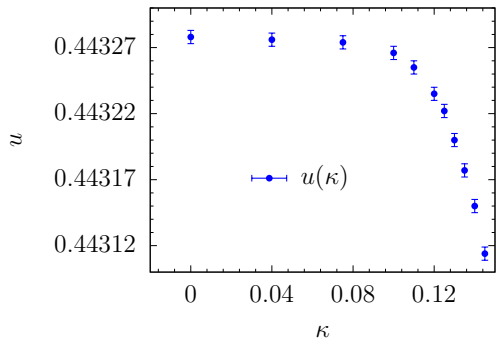

(c) $S_G^{\text{eff}} + S_0 + S_2, N_f = 1, N_t = 6$

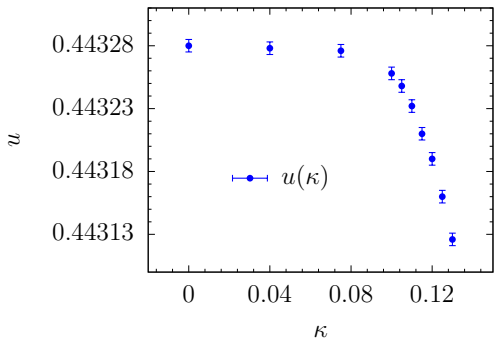

(d) $S_G^{\text{eff}} + S_0 + S_2, N_f = 2, N_t = 6$

Figure 6.12: The pseudo-critical line for the next-to-leading order effective theory with $N_f \in \{1, 2\}$, $N_t \in \{4, 6\}$ and $N_s = 24$. A linear fit was performed for $N_t = 4$ according to equation (6.24).

the entire line can be parameterized by the following linear equation

$$u_{pc}(\kappa) = u_0 - a_1\kappa, \tag{6.24}$$

with the following respective fit results,

$$a_1 = 0.0071(3), \quad u_0 = 0.429192(22), \quad \chi^2/\text{d.o.f} = 0.49, \quad \text{for} \quad N_f = 1, \tag{6.25}$$
$$a_1 = 0.0109(8), \quad u_0 = 0.429448(52), \quad \chi^2/\text{d.o.f} = 1.74, \quad \text{for} \quad N_f = 2. \tag{6.26}$$

On the other hand, for $N_t = 6$ the hopping parameter range is expanded, by which the linearity of the fit does not hold as shown in fig. 6.12 (c) and 6.12 (d) for $N_f = 1, 2$, respectively. Thus, for $N_t = 6$ we are only able to determine the critical hopping parameter κ_c by using eqn. (6.16).

After we have determined the tangent to the first-order transition line close to the endpoint, we still need to find the exact location of the critical endpoint on the phase boundary. We plot the minimum values of B_4 against the couplings h_1, κ for several volumes, see fig. 6.13, and perform a linear fit to equation (6.24). The χ^2/d.o.f values of the four fits are between $0.99 - 1.49$, showing good fit qualities. With the same analysis, we also estimate the critical values κ_c for the $\mathcal{O}(\kappa^2)$ effective action at $N_t = 6$, and for the $\mathcal{O}(\kappa^4)$ effective action at $N_t = 4$. All results are summarized in tab. 6.4. One observes that the value of κ_c for $N_f = 2$ of the

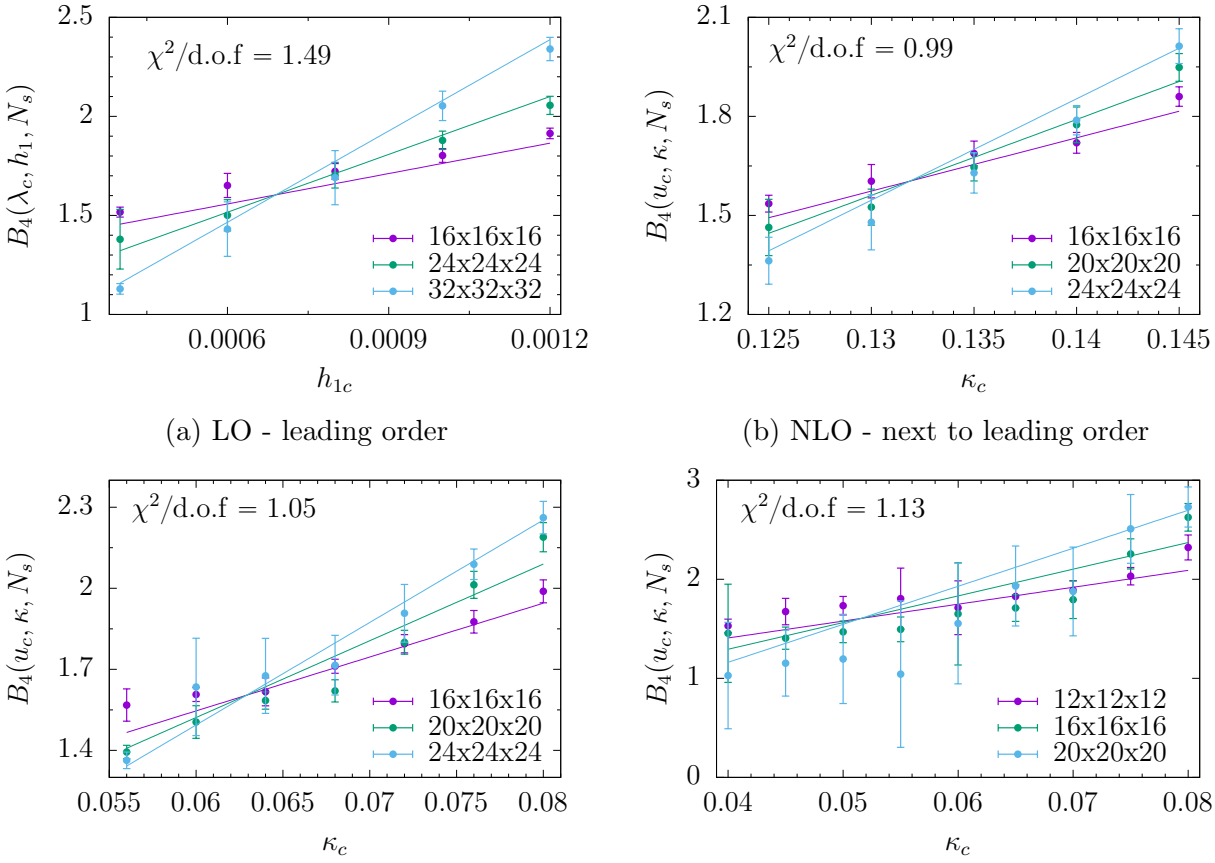

(a) LO - leading order

(b) NLO - next to leading order

(c) NLO - next to leading order

(d) NNLO - next to next to leading order

Figure 6.13: Example of multi-branch fits for the kurtosis at different orders of the effective theory

same order effective theory is smaller than those of $N_f = 1$. This can be easily seen from the shift to the left of the curve in fig. 6.12 (d) in comparison with the one in fig. 6.12 (c). We argue that this is because the explicit center symmetry breaking becomes stronger as there are more fermion fields involved. With the same argument, as it is expected, the critical value of the hopping parameter κ_c is shifted towards lower values for the higher-order effective theory.

In tab. 6.4, a comparison of our results with those obtained from 4-dimensional QCD simulations in heavy quark region is carried out, in one case with a hopping expanded fermion determinant, in the other case with no approximations. We see that the phase structure of the 4-dimensional full QCD is reproduced by the effective theories on a semi-quantitative level so that their application to the cold and dense regime can be trusted. Regarding quantitative accuracy, the comparison with either hopping expanded or full QCD allows for detailed conclusions regarding the strong coupling and hopping expansions: the three-dimensional effective theory agrees almost quantitatively with the hopping expanded four-dimensional QCD, while both exhibit larger differences with full QCD as N_t grows. This means that the character expansion shows good convergence behavior and is sufficient for these applications, while higher-order corrections are necessary in the hopping expansion already at $N_t = 6$.

Let us now determine the critical endpoint in the parameter space (u, κ) in S_{LO} and S_{NLO} for $N_t = 4$, where this point is computable due the linearity of the phase boundary. It is

		3d eff. theories		hopping expanded-QCD [115]		Full QCD [128]
N_t	action	$N_f = 1$	$N_f = 2$	$N_f = 1$	$N_f = 2$	$N_f = 2$
	S_{LO}	0.0810(4)	-	0.0783(12)	0.0658(10)	-
4	S_{NLO}	0.0756(6)	0.0629(4)	0.0753(11)	0.0640(10)	-
	S_{NNLO}	0.0515(16)	0.0443(34)	-	-	-
6	S_{NLO}	0.1319(6)	0.1210(5)	0.1326(21)	0.1202(19)	0.0877(9)

Table 6.4: Comparison of the κ_c-values for the deconfinement critical point obtained by different approximations to lattice QCD with Wilson quarks.

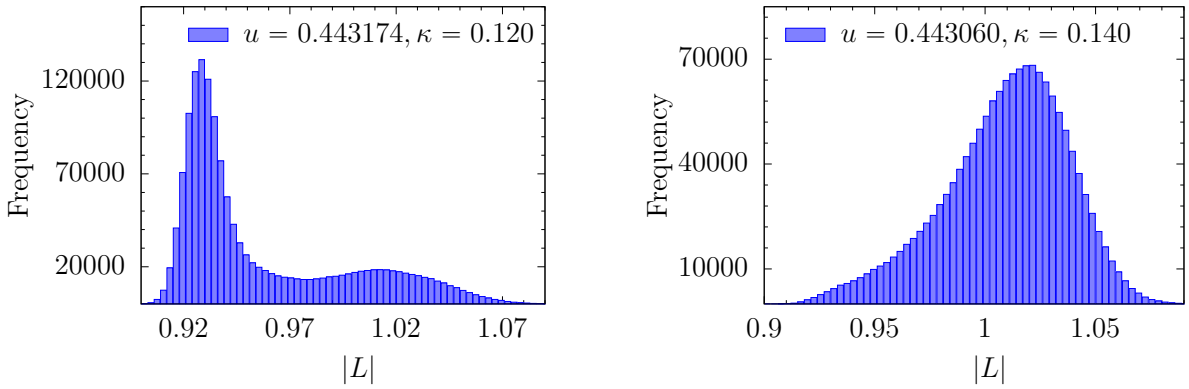

(a) First-order (b) Crossover

Figure 6.14: Histograms of $|L|$ for two different simulations with $N_f = 2, N_t = 6$ before and after the critical value.

straightforward to obtain the critical endpoint by inserting (6.23) into eqn. (6.22), and (6.25), (6.26) into eqn. (6.24), respectively, and then solve for λ_c and u_c. The resulting critical endpoint for the respective effective theory are

$$(\lambda_c, h_{1c}) = (0.18688(6), 0.000690(13)) \quad \text{for } S_{\mathrm{LO}}, \tag{6.27}$$

$$(u_c, \kappa_c) = (0.428658(32), 0.0756(6)) \quad \text{for } S_{\mathrm{NLO}} \text{ with } N_f = 1, \tag{6.28}$$

$$(u_c, \kappa_c) = (0.428762(60), 0.0629(4)) \quad \text{for } S_{\mathrm{NLO}} \text{ with } N_f = 2, \tag{6.29}$$

which have been partly shown in fig. 6.12 (a) and 6.12 (b). We cross-check the different behavior of first-order versus crossover at two points $p_1 = (u_1, \kappa_1) = (0.443174, 0.120)$ and $p_2 = (u_2, \kappa_2) = (0.443060, 0.140)$ by investigation of histograms for the distribution of the magnetization. From our previous analysis, the point p_1 is in the first-order region, while p_2 is in the crossover region. As one can see in fig. 6.14, the familiar metastable two-state signal - the coexistence of two phases that characterizes first-order transitions, is clearly established for the point p_1, while at p_2 - the point after the critical point, we have a crossover, where no region with coexisting phases is present and the magnetization does not scale with the volume.

As a last remark, it is important to point out that although we have good fits and consistent results for the $\mathcal{O}(\kappa^4)$ effective theory, its statistics for $N_f \in \{1, 2\}$ should be improved in order to obtain more accurate results for the critical endpoints. As we mentioned, a complicated action

such as the $\mathcal{O}(\kappa^4)$ effective action with a large number of terms can significantly slow down the simulation. Indeed, its updating time indeed increases $\sim$100 times that of the $\mathcal{O}(\kappa^2)$ effective theory with the same volume. There exists a powerful method called the multiple histogram method which combines all estimates of given simulations to give the best possible outcome for the expectation value of an observable, the reader is referred to [96, 129, 130] for a detailed discussion. Currently, this method applied to the $\mathcal{O}(\kappa^4)$ effective theory is being developed within our group, aiming to resolve the low statistics problem, i.e. the critical endpoint can be estimated with high accuracy, and an extension of our study for higher N_t and N_s at $\mathcal{O}(\kappa^4)$ is expected.

		$N_f = 1$		N_s				
action	N_t	κ/h	λ/u range	12	16	20	24	32
		0.00040	0.187250-0.187450	-	1.50M	-	1.50M	1.50M
		0.00060	0.186900-0.187100	-	1.50M	-	1.50M	1.50M
S_{LO}		0.00080	0.186550-0.186750	-	1.50M	-	1.50M	1.50M
		0.00100	0.186200-0.186400	-	1.50M	-	1.50M	1.50M
		0.00120	0.185850-0.186050	-	1.50M	-	1.50M	1.50M
	4	0.06000	0.428800-0.429000	-	1.00M	1.00M	1.00M	-
	4	0.06300	0.428800-0.429000	-	1.00M	1.00M	1.00M	-
	4	0.06600	0.428750-0.428950	-	1.00M	1.00M	1.00M	-
	4	0.06900	0.428750-0.428950	-	1.00M	1.00M	1.00M	-
	4	0.07200	0.428700-0.428900	-	1.00M	1.00M	1.00M	-
	4	0.07500	0.428700-0.428900	-	1.00M	1.00M	1.00M	-
S_{NLO}	4	0.07800	0.428700-0.428900	-	1.00M	1.00M	1.00M	-
	4	0.08100	0.428650-0.428850	-	1.00M	1.00M	1.00M	-
	6	0.12500	0.443200-0.443250	-	1.50M	1.50M	1.50M	-
	6	0.13000	0.443180-0.443230	-	1.50M	1.50M	1.50M	-
	6	0.13500	0.443155-0.443205	-	1.50M	1.50M	1.50M	-
	6	0.14000	0.443130-0.443180	-	1.50M	1.50M	1.50M	-
	6	0.14500	0.443095-0.428850	-	1.50M	1.50M	1.50M	-
	4	0.04000	0.428700-0.429000	0.20M	0.12M	0.06M	-	-
	4	0.04500	0.428650-0.428950	0.20M	0.12M	0.06M	-	-
	4	0.05000	0.428600-0.428900	0.20M	0.12M	0.06M	-	-
	4	0.05500	0.428550-0.428850	0.20M	0.12M	0.06M	-	-
S_{NNLO}	4	0.06000	0.428500-0.428800	0.20M	0.12M	0.06M	-	-
	4	0.06500	0.428450-0.428750	0.20M	0.12M	0.06M	-	-
	4	0.07000	0.428400-0.428700	0.20M	0.12M	0.06M	-	-
	4	0.07500	0.428200-0.428500	0.20M	0.12M	0.06M	-	-
	4	0.08000	0.428000-0.428300	0.20M	0.12M	0.06M	-	-

Table 6.5: Overview of the statistics accumulated in our simulations of the $N_f = 1$ effective theory at different κ-contributions.

		$N_f = 2$		N_s				
action	N_t	κ/h	λ/u range	12	16	20	24	32
	4	0.04000	0.428840-0.429040	-	1.50M	1.50M	1.50M	-
	4	0.04400	0.428840-0.429040	-	1.50M	1.50M	1.50M	-
	4	0.04800	0.428840-0.429040	-	1.50M	1.50M	1.50M	-
	4	0.05200	0.428800-0.429000	-	1.50M	1.50M	1.50M	-
	4	0.05600	0.428780-0.428880	-	1.50M	1.50M	1.50M	-
	4	0.06000	0.428750-0.428850	-	1.50M	1.50M	1.50M	-
	4	0.06400	0.428700-0.428800	-	1.50M	1.50M	1.50M	-
S_{NLO}	4	0.06800	0.428650-0.42850	-	1.50M	1.50M	1.50M	-
	4	0.07200	0.428630-0.428730	-	1.50M	1.50M	1.50M	-
	4	0.07600	0.428560-0.428660	-	1.50M	1.50M	1.50M	-
	4	0.08000	0.428500-0.428600	-	1.50M	1.50M	1.50M	-
	6	0.12500	0.443130-0.443180	-	1.50M	1.50M	1.50M	-
	6	0.13000	0.443100-0.443150	-	1.50M	1.50M	1.50M	-
	6	0.13500	0.443060-0.443110	-	1.50M	1.50M	1.50M	-
	6	0.14000	0.443010-0.443060	-	1.50M	1.50M	1.50M	-
	6	0.14500	0.442960-0.423010	-	1.50M	1.50M	1.50M	-
	4	0.04000	0.428650-0.428950	0.20M	0.12M	0.06M	-	-
	4	0.05000	0.428650-0.428950	0.20M	0.12M	0.06M	-	-
S_{NNLO}	4	0.06000	0.428550-0.428850	0.20M	0.12M	0.06M	-	-
	4	0.07000	0.428150-0.428450	0.20M	0.12M	0.06M	-	-
	4	0.08000	0.427500-0.427800	0.20M	0.12M	0.06M	-	-

Table 6.6: Overview of the statistics accumulated in our simulations of the $N_f = 2$ effective theory at different κ-contributions

Chapter 7

Conclusions and outlooks

In this work, we have investigated aspects of the deconfinement transition and its critical endpoint associated with the three-dimensional Polyakov loop effective theory with zero and nonzero chemical potential in the heavy quark regime. This theory is derived from thermal lattice QCD with heavy Wilson quarks by using combined strong coupling and hopping parameter expansions. It possesses the global center symmetry in the pure gauge sector, which is broken explicitly by dynamical fermions. With nonzero chemical potential, the effective theory has a fermion sign problem, but this sign problem is mild enough to be carried out by standard Monte-Carlo simulations. On the other hand, the effective theory is analogous to spin systems such as the three-dimensional Ising model, where interacting spins are replaced by interacting Polyakov loops. Thus, the effective theory allows an analytic evaluation by means of the high-temperature expansion. This method has many important properties such as it is not affected by the sign problem, is highly systematic, and serves as sophisticated tools for quantitative calculations in many areas of theoretical physics.

In this thesis, we have attempted to systematically improve the effective theory to higher orders in κ. We found that the kinetic quark determinant can be represented in terms of closed graphs which might be generated and evaluated by computer. We have successfully evaluated the effective pure gauge theory including static quarks with all chemical potentials by using the high-temperature expansion. The corresponding partition function and Polyakov loop susceptibility were computed to the 13th order. We have proposed a new series analysis tool - a combination of the Padé and the Canterbury approximant, which can signal the location of the critical endpoint on the phase boundary of the effective theory, while the Padé or the Canterbury approximant alone is only able to show the phase boundary. The entire deconfinement critical surface has been then determined, and our results are in good agreement with those obtained from simulations whose sign problem is solved by a flux representation. Furthermore, we have determined the critical endpoint associated with the effective theory with zero chemical potential up to $\mathcal{O}(\kappa^4)$ by using the Metropolis algorithm. Our results for the $\mathcal{O}(\kappa^2)$ effective theory agree excellently with those obtained from simulations of four-dimensional QCD after hopping expansion. There are differences between our results and the full QCD at $N_t = 6$, which indicates that higher corrections are necessary in the hopping expansion already at this temporal extent.

After introducing lattice gauge theory and its important features such as the symmetries of the system, how to get to the continuum limit, the construction of the theory at finite temperature and finite chemical potential or the QCD thermodynamics, in chapter 3 we have focused on the derivation of the effective theory up to $\mathcal{O}(\kappa^6)$. We have employed two expansion schemes: the character expansion and the hopping parameter expansion, and discussed their

effects on the effective theory. The exponential resummation scheme has been introduced in order to improve thermodynamics studies. In addition, we have attempted to improve the effective theory to $\mathcal{O}(\kappa^6)$. A graph representation method inspired by series expansions has been suggested, which might provide a systematic way to derive the effective theory on computer. Furthermore, we realized that in combination with the link-update method described in chapter 5 one can control the combinatorial problem arising from the re-expression of all terms of the effective action into a function of Polyakov loops. This indicates a boosting for the updating process since we have found in our simulations that due to the complexity of the $\mathcal{O}(\kappa^4)$ effective theory its updating time increases drastically compared to the order $\mathcal{O}(\kappa^2)$.

In chapter 4 we have discussed one of the main objectives of the present work, in particular, the analytical treatment for the pure gauge and static quarks. We have introduced first the graph terminology which plays a major role in the evaluation of the effective theory, where the high-temperature expansion was employed. We have then described the procedure of how one can generate graphs and compute their lattice constants on the computer using the 'Pegs in Holes' (PIH) algorithm. With the high-temperature expansion, we have computed successfully the partition function and the Polyakov susceptibility of the corresponding effective theory up to the 13th order in the effective gauge coupling λ. The analytic expression of the partition function allows us to derive and study the equation of state quite easily. However, since we are more interested in the study of the critical points, attention has been paid to the Polyakov loop susceptibility. We also discussed two series analysis methods which are combined to extract information about the criticality from the series.

In chapter 5 we gave a brief introduction to the Monte-Carlo method, in particular, the Metropolis algorithm which can be applied to the effective theory with zero chemical potential. The standard link proposal and the accept/reject step have been described in considerable detail. We have also described how the sign problem occurs in the study of lattice gauge theory at finite chemical potential, and the current status of this study. The end of this chapter was devoted to describing the jackknife method which was used to deal with the statistical errors from simulations.

Finally, we presented our analytic and numerical results in chapter 6. The Polyakov susceptibility of the effective pure gauge theory can be reproduced easily by taking $\kappa \to 0$. By means of a Padé analysis for a one-variable case, we have extracted critical couplings β_c for the phase transition. The results agree to better than 10% with simulations of the full four-dimensional Yang-Mills theory for $N_t = 2 - 16$. For the SU(2) case which possesses a second-order phase transition, the critical exponent γ_c was accurately reproduced, while the Padé analysis generally cannot identify a first-order transition like the case of SU(3). We have extended the effective theory by including static fermion fields at finite density. With a multivariate series at hand, we combine two different series analysis methods: Padé and Canterbury approximants to estimate the second-order endpoint for zero, finite and imaginary chemical potential. Our results agree well with those from simulations whose sign problem was resolved by the flux representation.

In tab. 6.4, we also compared our results with those obtained from four-dimensional QCD simulations in the heavy quark region, one case with a hopping expanded fermion determinant and the other case with no approximation. We observed that the phase structure of the four-dimensional full QCD is reproduced by the effective theories on a semi-quantitative level so that their application to the cold and dense regime can be trusted. Regarding quantitative accuracy, the comparison with either hopping expanded or full QCD allows for detailed conclusions regarding the strong coupling and hopping expansions separately: the three-dimensional effec-

tive theory agrees almost quantitatively with the hopping expanded four-dimensional QCD, while both exhibit larger differences with full QCD as N_t grows. This means that the character expansion shows good convergence behavior and is sufficient for thermodynamical applications up to $N_t = 6$, while higher-order corrections are necessary in the hopping expansion already at $N_t = 6$.

There are several promising directions for future research perspectives. First, the graph representation allows a systematic improvement of the effective theory, i.e., similar to series expansion methods an algorithm, which can generate all graphs according to a set of constraints, should be developed. One then applies directly the SU(3) link update in order to prevent the number of terms in the effective action from increasing exponentially, indicating the updating procedure is still efficient. This provides a possibility to aim for simulating the effective theory at higher orders in the hopping parameter, where we expect that its deconfinement transition occurs at a critical value compatible with the full QCD. Furthermore, the original attempt of the effective theory is to deal with the sign problem of the lattice QCD at finite chemical potential, with the excellent agreements of the effective theory with hopping-expanded full QCD the next interesting study is to explore the effective theory of higher orders in the hopping parameter at finite chemical potential. Currently, a method called the finite-cluster method has been developing for the effective theory, which attempts to simplify the effective theory by reorganizing and summing higher orders of the hopping parameter κ into an effective coupling analogous to $u(\beta)$ obtained by the character expansion. If this program is established, then series expansion methods might also be applied further to this improved effective theory. Last but not least, we should point out that applications of deep learning have been found recently in many areas of physics, from particle, condensed matter physics to cosmology. There are many quite promising results obtained using machine learning techniques for the study of phase transitions, for example, the study of two-dimensional complex scalar field theory at nonzero temperature and chemical potential with a nontrivial phase diagram using Generative Adversarial Networks (GAN) [131] or via the path optimization method [132]. Although the three-dimensional Polyakov loop effective theory at first sight seems to be only an approximation to the full QCD, we have shown that it still shares many important features with QCD, thus applying machine learning techniques to the effective theory at finite chemical potential might be a good probe to attack the sign problem of QCD.

Appendix A

Group integration

Based on a graphical method of computing integrals over matrix representations of the SU(N_c) group elements, which was developed in [133], we evaluate the following integrals explicitly that occur often in the derivation of the effective theory. In low-order strong coupling expansions, we have a useful integral

$$I^{c_1 d_1}_{a_1 b_1} = \int \mathrm{d}U U_{a_1 b_1} U^\dagger_{c_1 d_1} = \frac{1}{N_c} \delta_{a_1 d_1} \delta_{b_1 c_1}, \tag{A.1}$$

which reproduces the familiar single site integral of the form

$$I^{c_1 c_1}_{a_1 a_1} = \int \mathrm{d}U \,\mathrm{tr}\, U \,\mathrm{tr}\, U^\dagger = \int \mathrm{d}U L L^* = \frac{1}{N_c} \delta_{a_1 c_1} \delta_{a_1 c_1} = \frac{N_c}{N_c} = 1. \tag{A.2}$$

Moreover, to derive the $\mathcal{O}(\kappa^4)$ effective theory, there are steps involving integrals of four SU(N_c) elements

$$\begin{aligned} I^{c_1 d_1 c_2 d_2}_{a_1 b_1 a_2 b_2} =& \int \mathrm{d}U U_{a_1 b_1} U^\dagger_{c_1 d_1} U_{a_2 b_2} U^\dagger_{c_2 d_2}, \\ =& \frac{1}{N_c^2 - 1} (\delta_{a_1 d_1} \delta_{a_2 d_2} \delta_{b_1 c_1} \delta_{b_2 c_2} + \delta_{a_1 d_2} \delta_{a_2 d_1} \delta_{b_1 c_2} \delta_{b_2 c_1}) \\ & - \frac{1}{N_c (N_c^2 - 1)} (\delta_{a_1 d_1} \delta_{a_2 d_2} \delta_{b_1 c_2} \delta_{b_2 c_1} + \delta_{a_1 d_2} \delta_{a_2 d_1} \delta_{b_1 c_1} \delta_{b_2 c_2}), \end{aligned} \tag{A.3}$$

which similarly to (A.2) gives us

$$\begin{aligned} I^{c_1 c_2}_{a_1 a_2} =& \int \mathrm{d}U \,\mathrm{tr}\, U \,\mathrm{tr}\, U^\dagger \,\mathrm{tr}\, U \,\mathrm{tr}\, U^\dagger = \int \mathrm{d}U L^2 L^{*2} \\ =& \frac{1}{N_c^2 - 1} 2 N_c^2 - \frac{1}{N_c (N_c^2 - 1)} 2 N_c = 2 \frac{N_c^2 - 1}{N_c^2 - 1} = 2. \end{aligned} \tag{A.4}$$

The detailed calculation of the integrals (A.1) and (A.3) can be found in [133]. We follow the graphical method introduced in [133] to evaluate the integral of six SU(N_c) matrix elements

$$I^{c_1 d_1 c_2 d_2 c_3 d_3}_{a_1 b_1 a_2 b_2 a_3 b_3} = \int \mathrm{d}U U_{a_1 b_1} U^\dagger_{c_1 d_1} U_{a_2 b_2} U^\dagger_{c_2 d_2} U_{a_3 b_3} U^\dagger_{c_3 d_3}, \tag{A.5}$$

which is an important step for deriving the effective theory up to the 6th order in κ, where there is a case that all six spatial hops occupy the same spatial link at the same time slice. It is evaluated as follows: First, a group element U_{ab}, its inverse $U^\dagger_{ab}$ which is also the conjugate of this element in SU(N_c) and the Kronecker symbol can be illustrated as upward directed, downward directed and undirected lines, respectively

U_{ab} = , $U^\dagger_{ab}$ = , δ_{ab} =

Here the labels of the ends of these line segments are the matrix indices of the respective group elements. Running from the first to the second index can be represented by the line direction. After introducing these conventions, it is straightforward to see that the graphic representation of the integral I is

$I^{c_1 d_1 c_2 d_2 c_3 d_3}_{a_1 b_1 a_2 b_2 a_3 b_3}$ = 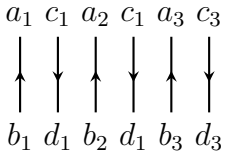 (A.6)

We replace $U^\dagger$ with the cofactor of U to make all lines direct upwards, where the cofactor of U is defined as follows

$$\begin{aligned} U^\dagger_{ab} &= (\mathrm{cof}U)_{ba} \\ &= \frac{1}{(N_c-1)} \varepsilon_{b,a_1,\ldots,a_{N_c-1}} \varepsilon_{a,b_1,\ldots,b_{N_c-1}} U_{a_1 b_1} \ldots U_{a_{N_c-1} b_{N_c-1}}. \end{aligned} \tag{A.7}$$

By substituting (A.7) into (A.6) we obtain an expression with $(2N_c)!/(2!N_c!^2)$ terms. However, there is a trick to simplify this evaluation for general N_c. All resulting terms will all have six, an even number, of ε vertices both at the top and at the bottom of the diagram. These can be eliminated using the following identities

$$\begin{aligned} &\varepsilon_{a_1,\ldots,a_{N_c}} \varepsilon_{a_1,\ldots,a_{N_c}} = N_c!, \\ &\varepsilon_{a,a_1,\ldots,a_{N_c}} \varepsilon_{b,a_1,\ldots,a_{N_c}} = (N_c-1)! \delta_{ab}, \\ &\varepsilon_{a,b,a_1,\ldots,a_{N_c}} \varepsilon_{c,d,a_1,\ldots,a_{N_c}} = (N_c-2)! (\delta_{ac}\delta_{bd} - \delta_{ad}\delta_{bc}). \end{aligned} \tag{A.8}$$

The terms are then reduced to sets of Kronecker δ symbols connecting separately indices at the top and the bottom of the diagram. Moreover, a Kronecker δ cannot connect the indices a_i and c_i or b_i and d_i according to our choice of notations, because they can be initially coupled only through an odd number of ϵ vertices. According to the symmetry of the integrand under $c_1 d_1 \leftrightarrow c_2 d_2 \leftrightarrow c_3 d_3$ we obtain $3! = 6$ independent sets of graphs and 6 independent coefficients k_i for $i = 1, \ldots, 6$ as below. This results I to be in terms of sets of Kronecker δ symbols connecting separately indices at the top and bottom of the diagram.

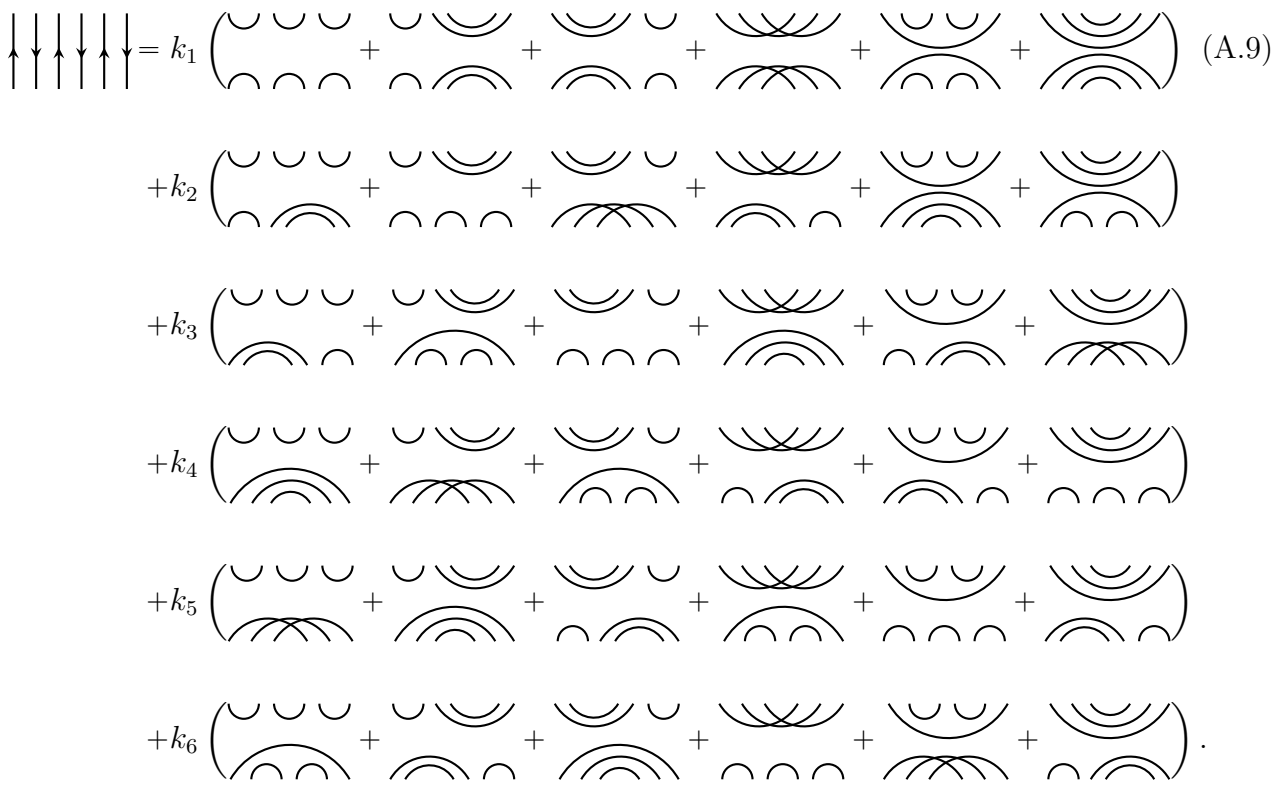

(A.9)

The coefficients k_i for $i = 1, ..., 6$ can be determined by multiplying by $\delta_{a_1c_1}$ to I and using the result in (A.3) to reduce the integral

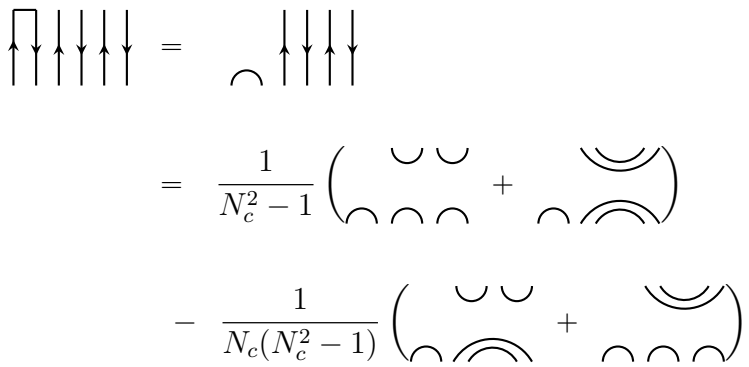

(A.10)

Next we can multiply $\delta_{a_1c_1}$ to the general expression of I in (A.9), equalize it with (A.10) to give six equations with k_i as variables. We then solve these equations for the coefficients $k_1, ..., k_6$, and obtain

$$
\begin{aligned}
k_1 &= \frac{N_c^2 - 2}{N_c(N_c^4 - 5N_c^2 + 4)}, \\
k_2 &= -\frac{1}{N_c^2 - 5N_c^2 + 4}, \\
k_3 = k_4 &= -\frac{1}{(N_c^2 - 1)(N_c^2 - 4)}, \\
k_5 = k_6 &= \frac{2}{N_c(N_c^2 - 1)(N_c^2 - 4)}.
\end{aligned}
$$

Finally, inserting the coefficients k_i in $I^{c_1d_1c_2d_2c_3d_3}_{a_1b_1a_2b_2a_3b_3}$ and converting its graph representation in terms of the Kronecker δ symbols give the desired integral

$$
\begin{aligned}
I = \frac{N_c^2-2}{N_c(N_c^4-5N_c^2+4)} \cdot \Big(& \delta_{a_1c_1}\delta_{a_2c_2}\delta_{a_3c_3}\delta_{b_1d_1}\delta_{b_2d_2}\delta_{b_3d_3} + \delta_{a_1c_1}\delta_{a_2c_3}\delta_{a_3c_2}\delta_{b_1d_1}\delta_{b_2d_3}\delta_{b_3d_2} \\
& + \delta_{a_1c_2}\delta_{a_2c_1}\delta_{a_3c_3}\delta_{b_1d_2}\delta_{b_2d_1}\delta_{b_3d_3} + \delta_{a_1c_2}\delta_{a_2c_3}\delta_{a_3c_1}\delta_{b_1d_2}\delta_{b_2d_3}\delta_{b_3d_1} \\
& + \delta_{a_1c_3}\delta_{a_2c_1}\delta_{a_3c_2}\delta_{b_1d_3}\delta_{b_2d_1}\delta_{b_3d_2} + \delta_{a_1c_3}\delta_{a_2c_2}\delta_{a_3c_1}\delta_{b_1d_3}\delta_{b_2d_2}\delta_{b_3d_1} \Big) \\
- \frac{1}{N_c^4-5N_c^2+4} \cdot \Big(& \delta_{a_1c_1}\delta_{a_2c_2}\delta_{a_3c_3}\delta_{b_1d_1}\delta_{b_2d_3}\delta_{b_3d_2} + \delta_{a_1c_1}\delta_{a_2c_3}\delta_{a_3c_2}\delta_{b_1d_1}\delta_{b_2d_2}\delta_{b_3d_3} \\
& + \delta_{a_1c_2}\delta_{a_2c_1}\delta_{a_3c_3}\delta_{b_1d_2}\delta_{b_2d_3}\delta_{b_3d_1} + \delta_{a_1c_2}\delta_{a_2c_3}\delta_{a_3c_1}\delta_{b_1d_2}\delta_{b_2d_1}\delta_{b_3d_3} \\
& + \delta_{a_1c_3}\delta_{a_2c_1}\delta_{a_3c_2}\delta_{b_1d_3}\delta_{b_2d_2}\delta_{b_3d_1} + \delta_{a_1c_3}\delta_{a_2c_2}\delta_{a_3c_1}\delta_{b_1d_3}\delta_{b_2d_1}\delta_{b_3d_2} \Big) \\
- \frac{1}{(N_c^2-1)(N_c^2-4)} \cdot \Big(& \delta_{a_1c_1}\delta_{a_2c_2}\delta_{a_3c_3}\delta_{b_1d_2}\delta_{b_2d_1}\delta_{b_3d_3} + \delta_{a_1c_1}\delta_{a_2c_3}\delta_{a_3c_2}\delta_{b_1d_3}\delta_{b_2d_1}\delta_{b_3d_3} \\
& + \delta_{a_1c_2}\delta_{a_2c_1}\delta_{a_3c_3}\delta_{b_1d_1}\delta_{b_2d_2}\delta_{b_3d_3} + \delta_{a_1c_2}\delta_{a_2c_3}\delta_{a_3c_1}\delta_{b_1d_3}\delta_{b_2d_2}\delta_{b_3d_1} \\
& + \delta_{a_1c_3}\delta_{a_2c_1}\delta_{a_3c_2}\delta_{b_1d_1}\delta_{b_2d_3}\delta_{b_3d_2} + \delta_{a_1c_3}\delta_{a_2c_2}\delta_{a_3c_1}\delta_{b_1d_2}\delta_{b_2d_3}\delta_{b_3d_1} \\
& + \delta_{a_1c_1}\delta_{a_2c_2}\delta_{a_3c_3}\delta_{b_1d_3}\delta_{b_2d_2}\delta_{b_3d_1} + \delta_{a_1c_1}\delta_{a_2c_3}\delta_{a_3c_2}\delta_{b_1d_2}\delta_{b_2d_3}\delta_{b_3d_1} \\
& + \delta_{a_1c_2}\delta_{a_2c_1}\delta_{a_3c_3}\delta_{b_1d_3}\delta_{b_2d_1}\delta_{b_3d_2} + \delta_{a_1c_2}\delta_{a_2c_3}\delta_{a_3c_1}\delta_{b_1d_1}\delta_{b_2d_3}\delta_{b_3d_2} \\
& + \delta_{a_1c_3}\delta_{a_2c_1}\delta_{a_3c_2}\delta_{b_1d_2}\delta_{b_2d_1}\delta_{b_3d_3} + \delta_{a_1c_3}\delta_{a_2c_2}\delta_{a_3c_1}\delta_{b_1d_1}\delta_{b_2d_2}\delta_{b_3d_3} \Big) \\
+ \frac{2}{N_c(N_c^2-1)(N_c^2-4)} \cdot \Big(& \delta_{a_1c_1}\delta_{a_2c_2}\delta_{a_3c_3}\delta_{b_1d_2}\delta_{b_2d_3}\delta_{b_3d_1} + \delta_{a_1c_1}\delta_{a_2c_3}\delta_{a_3c_2}\delta_{b_1d_3}\delta_{b_2d_2}\delta_{b_3d_1} \\
& + \delta_{a_1c_2}\delta_{a_2c_1}\delta_{a_3c_3}\delta_{b_1d_1}\delta_{b_2d_3}\delta_{b_3d_2} + \delta_{a_1c_2}\delta_{a_2c_3}\delta_{a_3c_1}\delta_{b_1d_3}\delta_{b_2d_1}\delta_{b_3d_2} \\
& + \delta_{a_1c_3}\delta_{a_2c_1}\delta_{a_3c_2}\delta_{b_1d_1}\delta_{b_2d_2}\delta_{b_3d_3} + \delta_{a_1c_3}\delta_{a_2c_2}\delta_{a_3c_1}\delta_{b_1d_2}\delta_{b_2d_1}\delta_{b_3d_3} \\
& + \delta_{a_1c_1}\delta_{a_2c_2}\delta_{a_3c_3}\delta_{b_1d_3}\delta_{b_2d_1}\delta_{b_3d_2} + \delta_{a_1c_2}\delta_{a_2c_3}\delta_{a_3c_2}\delta_{b_1d_1}\delta_{b_2d_2}\delta_{b_3d_3} \\
& + \delta_{a_1c_3}\delta_{a_2c_2}\delta_{a_3c_1}\delta_{b_1d_1}\delta_{b_2d_3}\delta_{b_3d_2} + \delta_{a_1c_2}\delta_{a_2c_1}\delta_{a_3c_3}\delta_{b_1d_3}\delta_{b_2d_2}\delta_{b_3d_1} \\
& + \delta_{a_1c_1}\delta_{a_2c_3}\delta_{a_3c_2}\delta_{b_1d_2}\delta_{b_2d_1}\delta_{b_3d_3} + \delta_{a_1c_2}\delta_{a_2c_1}\delta_{a_3c_2}\delta_{b_1d_2}\delta_{b_2d_3}\delta_{b_3d_1} \Big). \qquad \text{(A.11)}
\end{aligned}
$$

In order to ensure correctness of the formula, we can compute

$$\begin{aligned}\mathcal{I} &= \int \mathrm{d}U \,\mathrm{tr}\, U \,\mathrm{tr}\, U^\dagger \,\mathrm{tr}\, U \,\mathrm{tr}\, U^\dagger \,\mathrm{tr}\, U \,\mathrm{tr}\, U^\dagger \\ &= \int \mathrm{d}U U_{a_1a_1} U^\dagger_{c_1c_1} U_{a_2a_2} U^\dagger_{c_2c_2} U_{a_3a_3} U^\dagger_{c_3c_3} = \int \mathrm{d}U L^3 L^{*3},\end{aligned}$$

where the Einstein sum convention over the indices a_i and c_i is applied. Then we obtain easily

$$\begin{aligned}\mathcal{I} =& \frac{N_c^2-2}{N_c(N_c^4-5N_c^2+4)} \cdot 6N_c^3 - \frac{1}{N_c^4-5N_c^2+4} \cdot 6N_c^2 \\ & - \frac{1}{(N_c^2-1)(N_c^2-4)} \cdot 12N_c^2 + \frac{2}{N_c(N_c^2-1)(N_c^2-4)} \cdot 12N_c = 6. \end{aligned} \tag{A.12}$$

The results in (A.2), (A.4) and (A.12) agrees with results computed using generating functions in [90], which ensures the correctness of our computations. In addition, we observe an interesting property of the $\mathrm{SU}(N_c)$ group integration that for an equal power of L and L^*, the integral

$$\int \mathrm{d}L^n L^{*n} \tag{A.13}$$

is independent of N_c for $N_c > 2$.

Appendix B

W_{nm} terms

An important group dependent quantity of interest appearing in the effective action is the traces over rational functions containing temporal Wilson line, and their general form reads

$$W_{nm} = \mathrm{tr}\,\frac{(h_1 W)^m}{(1+h_1 W)^n}, \tag{B.1}$$

It is convenient for our analytic and numerical calculations to reformulate this quantity in terms of Polyakov loops. This can be done using the expression for the static determinant

$$\begin{aligned} G(\alpha,\beta) &= \log\det(\alpha+\beta h_1 W), \\ &= \log(\alpha^3+\alpha^2\beta h_1 L + \alpha\beta^2 h_1^2 L* + \beta^3 h_1^3). \end{aligned} \tag{B.2}$$

The quantity W_{nm} can then be computed by taking derivatives with respect to α and β at $\alpha=\beta=1$ as follows

$$W_{nm} = \frac{(-1)^{n-1}}{(n-1)!}\frac{\partial^{(n-m)}}{\partial\alpha^{(n-m)}}\frac{\partial^m}{\partial\beta^m}G(\alpha,\beta)\bigg|_{\alpha=\beta=1}. \tag{B.3}$$

As an example, let us consider the case $m=1, n=2$, using eqn. B.2 and B.3 we obtain

$$\begin{aligned} W_{21} = \mathrm{tr}\,\frac{h_1 W}{(1+h_1 W)^2} &= -\frac{\partial}{\partial\alpha}\frac{\partial}{\partial\beta}G(\alpha,\beta)\bigg|_{\alpha=\beta=1} \\ &= \frac{h_1\left(L+4h_1^3+4h_1 L^*+h_1^4 L^*+h_1^2(9+LL^*)\right)}{(1+h_1 L+h_1^2 L^*+h_1^3)^2}. \end{aligned} \tag{B.4}$$

Appendix C

Coefficients χ_L and f

As was remarked in the introduction, it is indeed not possible to publish all the expansion coefficients in this work since there several thousands of them. Thus, only some specific cases which were reduced to one-variable series are printed here. Furthermore, it was emphasized earlier that the equation of state can be easily obtained from the log Z series, which is valid up to the phase transition. Although the study of the equation of state is not in our main focus, for completeness we provide the coefficients to the 13th order of the free energy for specific values of h and μ.

	zero μ	finite μ	imaginary μ_i
n	$a_n(h = 0.00073, \mu = 0)$	$a_n(h = 0.001, \mu = 0.9)$	$a_n(h = 0.0015, \mu_i = \pi/3)$
0	$2.00292 \cdot 10^0$	$2.00573 \cdot 10^0$	$2.00300 \cdot 10^0$
1	$1.20526 \cdot 10^1$	$1.21033 \cdot 10^1$	$1.20541 \cdot 10^1$
2	$6.05265 \cdot 10^1$	$6.10349 \cdot 10^1$	$6.05415 \cdot 10^1$
3	$3.04304 \cdot 10^2$	$3.08466 \cdot 10^2$	$3.04431 \cdot 10^2$
4	$1.60359 \cdot 10^3$	$1.63419 \cdot 10^3$	$1.60457 \cdot 10^3$
5	$8.14895 \cdot 10^3$	$8.35948 \cdot 10^3$	$8.15596 \cdot 10^3$
6	$4.27868 \cdot 10^4$	$4.41705 \cdot 10^4$	$4.28353 \cdot 10^4$
7	$2.20149 \cdot 10^5$	$2.28954 \cdot 10^5$	$2.20475 \cdot 10^5$
8	$1.15583 \cdot 10^6$	$1.21050 \cdot 10^6$	$1.15797 \cdot 10^6$
9	$5.98944 \cdot 10^6$	$6.32248 \cdot 10^6$	$6.00321 \cdot 10^6$
10	$3.14946 \cdot 10^7$	$3.34933 \cdot 10^7$	$3.15821 \cdot 10^7$
11	$1.64075 \cdot 10^8$	$1.75925 \cdot 10^8$	$1.64623 \cdot 10^8$
12	$8.83686 \cdot 10^8$	$9.53410 \cdot 10^8$	$8.87094 \cdot 10^8$
13	$4.74047 \cdot 10^9$	$5.14824 \cdot 10^9$	$4.76150 \cdot 10^9$

Table C.1: Coefficients of the Polyakov loop susceptibility χ_L for zero, finite and imaginary chemical potential.

	zero μ	finite μ	imaginary μ_i
n	$a_n(h = 0.00073, \mu = 0)$	$a_n(h = 0.0012, \mu = 1.0)$	$a_n(h = 0.0013, \mu_i = \pi/4)$
0	$2.13471 \cdot 10^{-6}$	$5.89918 \cdot 10^{-6}$	$6.74758 \cdot 10^{-6}$
1	$1.28176 \cdot 10^{-5}$	$3.58127 \cdot 10^{-5}$	$4.04483 \cdot 10^{-5}$
2	$6.41817 \cdot 10^{-5}$	$1.83240 \cdot 10^{-4}$	$2.01870 \cdot 10^{-4}$
3	$3.21501 \cdot 10^{-4}$	$9.42655 \cdot 10^{-4}$	$1.00701 \cdot 10^{-3}$
4	$6.00169 \cdot 10^{0}$	$6.00508 \cdot 10^{0}$	$6.00526 \cdot 10^{0}$
5	$8.53664 \cdot 10^{-3}$	$2.65332 \cdot 10^{-2}$	$2.64835 \cdot 10^{-2}$
6	$4.40446 \cdot 10^{1}$	$4.41429 \cdot 10^{1}$	$4.41377 \cdot 10^{1}$
7	$3.62284 \cdot 10^{1}$	$3.67570 \cdot 10^{1}$	$3.67004 \cdot 10^{1}$
8	$5.05193 \cdot 10^{2}$	$5.08081 \cdot 10^{2}$	$5.07637 \cdot 10^{2}$
9	$6.94145 \cdot 10^{2}$	$7.09778 \cdot 10^{2}$	$7.06613 \cdot 10^{2}$
10	$7.29214 \cdot 10^{3}$	$7.37758 \cdot 10^{3}$	$7.35672 \cdot 10^{3}$
11	$1.40984 \cdot 10^{4}$	$1.45623 \cdot 10^{4}$	$1.44292 \cdot 10^{4}$
12	$2.43094 \cdot 10^{5}$	$2.45666 \cdot 10^{5}$	$2.44853 \cdot 10^{5}$
13	$6.65170 \cdot 10^{5}$	$6.79387 \cdot 10^{5}$	$6.74481 \cdot 10^{5}$

Table C.2: Coefficients of the free energy f for zero, finite and imaginary chemical potential.

Appendix D

Graph representations of the $\mathcal{O}(\kappa^6)$ effective action

As mentioned in section 3.4, in this appendix we present the rest of the K_6^1 expressions, and an incomplete list of graph representations for the $\mathcal{O}(\kappa^6)$ effective theory because the whole graph representations are just too long to print. We will make the whole graph representations of K_6 present somewhere else. At the $\mathcal{O}(\kappa^6)$ effective theory, we still managed to get its complete set of graph representations, and no graph generation program is required. However, to derive the effective theory at higher orders in κ a graph generating algorithm is necessary because the number of graphs will increase exponentially. A starting point for this program is to modify the program provided in [83] which is used for an effective theory in the cold and dense regime. In addition, we note that the graph representations listed here are before the resummation, and in order to obtain the resummed action one needs to pay attention to terms contributing to the resummation of lower orders.

Let us present the rest expressions of K_6^1 contributions $K_6^{1b}, \ldots, K_6^{1e}$

$$
\begin{aligned}
Z_6^{1b} = \int \mathscr{D}U_i \sum_{i,t_n,\vec{n}} \mathrm{tr}\Big[& \triangle_{t_{n_1}t_{n_1}}(\vec{n})\Gamma_+^i U_i(t_{n_1},\vec{n}) \cdot \triangle_{t_{n_1}t_{n_2}}(\vec{n}+\hat{i})\Gamma_+^i U_i(t_{n_2},\vec{n}+\hat{i}) \\
& \triangle_{t_{n_2}t_{n_3}}(\vec{n}+2\hat{i})\Gamma_+^j U_j(t_{n_3},\vec{n}+2\hat{i}) \cdot \triangle_{t_{n_3}t_{n_3}}(\vec{n}+2\hat{i}+\hat{j})\Gamma_-^i U_i^\dagger(t_{n_3},\vec{n}+2\hat{i}) \\
& \triangle_{t_{n_3}t_{n_2}}(\vec{n}+2\hat{i})\Gamma_-^i U_i^\dagger(t_{n_2},\vec{n}+\hat{i}) \cdot \triangle_{t_{n_2}t_{n_1}}(\vec{n}+\hat{i})\Gamma_-^i U_i^\dagger(t_{n_1},\vec{n})\Big].
\end{aligned} \tag{D.1}
$$

$$
\begin{aligned}
Z_6^{1c} = \int \mathscr{D}U_i \sum_{i,t_n,\vec{n}} \mathrm{tr}\Big[& \triangle_{t_{n_1}t_{n_1}}(\vec{n})\Gamma_+^i U_i(t_{n_1},\vec{n}) \cdot \triangle_{t_{n_1}t_{n_2}}(\vec{n}+\hat{i})\Gamma_+^j U_j(t_{n_2},\vec{n}+\hat{i}) \\
& \triangle_{t_{n_2}t_{n_3}}(\vec{n}+\hat{i}+\hat{j})\Gamma_+^i U_i(t_{n_3},\vec{n}+\hat{i}+\hat{j}) \cdot \triangle_{t_{n_3}t_{n_3}}(\vec{n}+2\hat{i}+\hat{j})\Gamma_-^i U_i^\dagger(t_{n_3},\vec{n}+\hat{i}+\hat{j}) \\
& \triangle_{t_{n_3}t_{n_2}}(\vec{n}+\hat{i}+\hat{j})\Gamma_-^j U_j^\dagger(t_{n_2},\vec{n}+\hat{i}) \cdot \triangle_{t_{n_2}t_{n_1}}(\vec{n}+\hat{i})\Gamma_-^i U_i^\dagger(t_{n_1},\vec{n})\Big].
\end{aligned} \tag{D.2}
$$

$$Z_6^{1d} = \int \mathscr{D}U_i \sum_{i,t_n,\vec{n}} \mathrm{tr}\Big[\triangle_{t_{n_1}t_{n_1}}(\vec{n})\Gamma^i_+ U_i(t_{n_1},\vec{n}) \cdot \triangle_{t_{n_1}t_{n_2}}(\vec{n}+\hat{i})\Gamma^j_+ U_j(t_{n_2},\vec{n}+\hat{i})$$
$$\triangle_{t_{n_2}t_{n_3}}(\vec{n}+\hat{i}+\hat{j})\Gamma^j_+ U_j(t_{n_3},\vec{n}+\hat{i}+\hat{j}) \cdot \triangle_{t_{n_3}t_{n_3}}(\vec{n}+2\hat{i}+\hat{j})\Gamma^j_- U^\dagger_j(t_{n_3},\vec{n}+\hat{i}+\hat{j})$$
$$\triangle_{t_{n_3}t_{n_2}}(\vec{n}+\hat{i}\hat{j})\Gamma^j_- U^\dagger_j(t_{n_2},\vec{n}+\hat{i}) \cdot \triangle_{t_{n_2}t_{n_1}}(\vec{n}+\hat{i})\Gamma^i_- U^\dagger_i(t_{n_1},\vec{n})\Big]. \tag{D.3}$$

$$Z_6^{1e} = \int \mathscr{D}U_i \sum_{i,t_n,\vec{n}} \mathrm{tr}\Big[\triangle_{t_{n_1}t_{n_1}}(\vec{n})\Gamma^i_+ U_i(t_{n_1},\vec{n}) \cdot \triangle_{t_{n_1}t_{n_2}}(\vec{n}+\hat{i})\Gamma^j_+ U_j(t_{n_2},\vec{n}+\hat{i})$$
$$\triangle_{t_{n_2}t_{n_3}}(\vec{n}+\hat{i}+\hat{j})\Gamma^k_+ U_k(t_{n_3},\vec{n}+\hat{i}+\hat{j}) \cdot \triangle_{t_{n_3}t_{n_3}}(\vec{n}+\hat{i}+\hat{j}+\hat{k})\Gamma^k_- U^\dagger_k(t_{n_3},\vec{n}+\hat{i}+\hat{j})$$
$$\triangle_{t_{n_3}t_{n_2}}(\vec{n}+\hat{i}+\hat{j})\Gamma^j_- U^\dagger_j(t_{n_2},\vec{n}+\hat{i}) \cdot \triangle_{t_{n_2}t_{n_1}}(\vec{n}+\hat{i})\Gamma^i_- U^\dagger_i(t_{n_1},\vec{n})\Big]. \tag{D.4}$$

Here the spatial directions are different, i.e., $i \neq j \neq k$. Their graph representations are presented in tab. D.1.

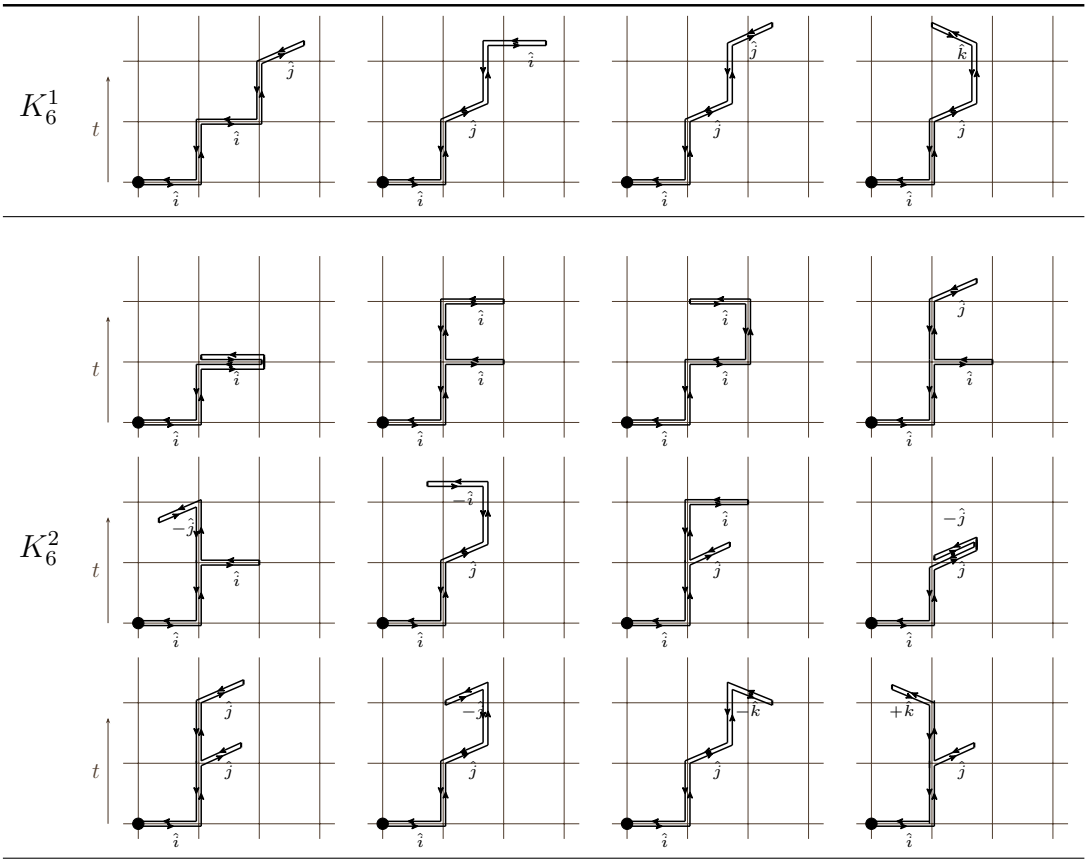

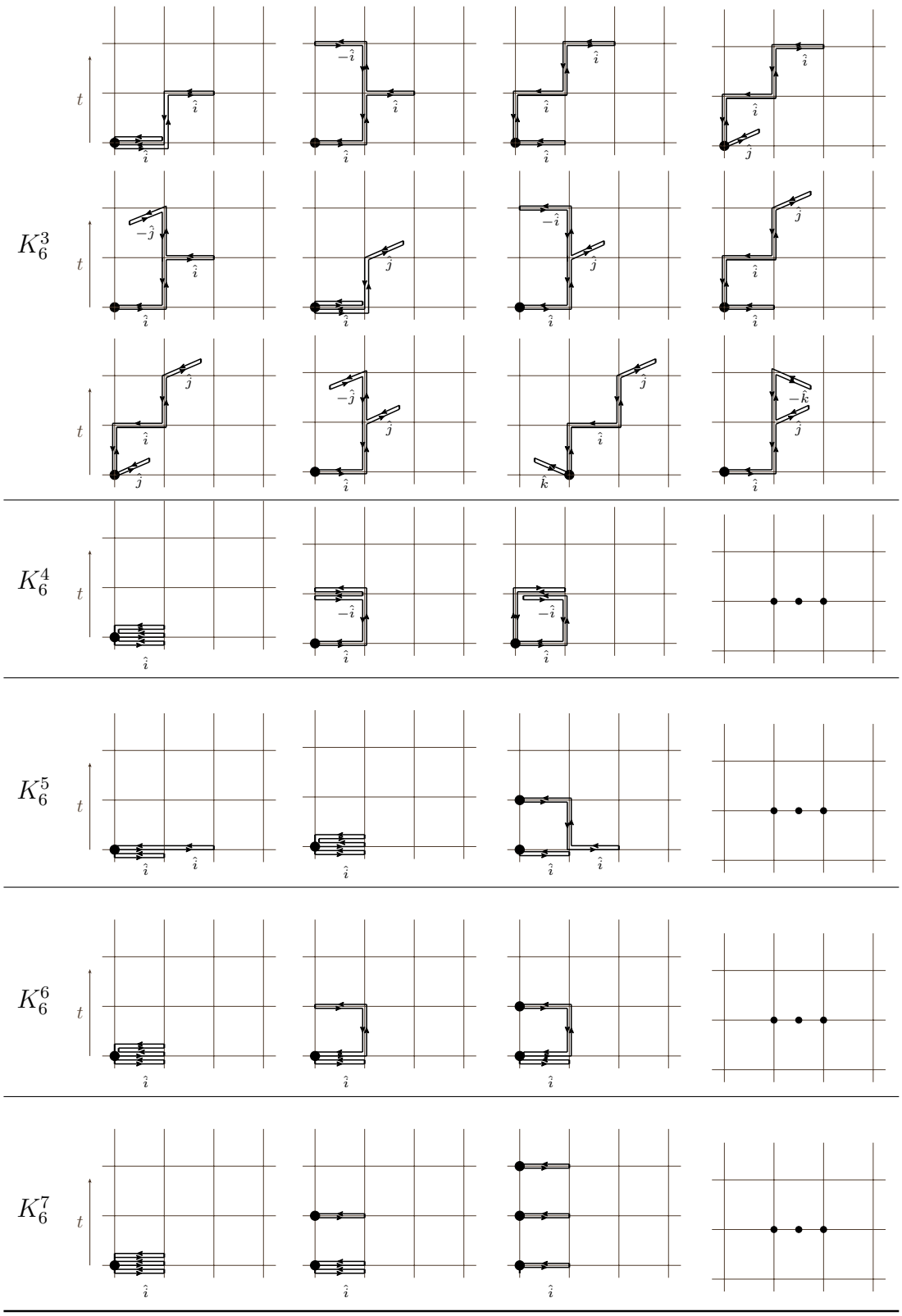

Table D.1: Graph representations associated to $\mathcal{O}(\kappa^6)$ contributions of the effective theory.

Bibliography

[1] M. Gell-Mann, *A Schematic Model of Baryons and Mesons*, *Phys. Lett.* **8** (1964) 214–215.

[2] G. Zweig, *An SU(3) model for strong interaction symmetry and its breaking. Version 2*, in *Developments in the quark theory of hadrons. Vol. 1. 1964 - 1978* (D. B. Lichtenberg and S. P. Rosen, eds.), pp. 22–101, 2, 1964.

[3] M. Luscher, *Computational Strategies in Lattice QCD*, in *Les Houches Summer School: Session 93: Modern perspectives in lattice QCD: Quantum field theory and high performance computing*, pp. 331–399, 2, 2010. arXiv:1002.4232.

[4] D. H. Rischke, *The Quark gluon plasma in equilibrium*, *Prog. Part. Nucl. Phys.* **52** (2004) 197–296, [nucl-th/0305030].

[5] F. Wilczek, *Did the Big Bang boil?*, *Nature* **443** (2006) 637–638.

[6] Y. Aoki, G. Endrodi, Z. Fodor, S. Katz, and K. Szabo, *The Order of the quantum chromodynamics transition predicted by the standard model of particle physics*, *Nature* **443** (2006) 675–678, [hep-lat/0611014].

[7] F. Karsch, T. Neuhaus, A. Patkos, and J. Rank, *Critical Higgs mass and temperature dependence of gauge boson masses in the SU(2) gauge Higgs model*, *Nucl. Phys. B Proc. Suppl.* **53** (1997) 623–625, [hep-lat/9608087].

[8] K. Kajantie, M. Laine, K. Rummukainen, and M. E. Shaposhnikov, *Is there a hot electroweak phase transition at m(H) larger or equal to m(W)?*, *Phys. Rev. Lett.* **77** (1996) 2887–2890, [hep-ph/9605288].

[9] V. A. Rubakov and D. S. Gorbunov, *Introduction to the Theory of the Early Universe: Hot big bang theory*. World Scientific, Singapore, 2017.

[10] A. M. Halasz, A. Jackson, R. Shrock, M. A. Stephanov, and J. Verbaarschot, *On the phase diagram of QCD*, *Phys. Rev. D* **58** (1998) 096007, [hep-ph/9804290].

[11] J. B. Kogut and M. A. Stephanov, *The phases of quantum chromodynamics: From confinement to extreme environments*, vol. 21. Cambridge University Press, 12, 2004.

[12] K. Rajagopal and F. Wilczek, *The Condensed matter physics of QCD*, in *At the frontier of particle physics. Handbook of QCD. Vol. 1-3* (M. Shifman and B. Ioffe, eds.), pp. 2061–2151, 11, 2000. hep-ph/0011333.

[13] M. G. Alford, *Color superconducting quark matter*, *Ann. Rev. Nucl. Part. Sci.* **51** (2001) 131–160, [hep-ph/0102047].

[14] M. A. Stephanov, *QCD phase diagram and the critical point*, *Prog. Theor. Phys. Suppl.* **153** (2004) 139–156, [hep-ph/0402115].

[15] P. de Forcrand, S. Kim, and O. Philipsen, *A QCD chiral critical point at small chemical potential: Is it there or not?*, *PoS* **LATTICE2007** (2007) 178, [arXiv:0711.0262].

[16] P. de Forcrand and O. Philipsen, *The Chiral critical line of N(f) = 2+1 QCD at zero and non-zero baryon density*, *JHEP* **01** (2007) 077, [hep-lat/0607017].

[17] S. Gavin, A. Gocksch, and R. D. Pisarski, *QCD and the chiral critical point*, *Phys. Rev. D* **49** (1994) R3079–R3082, [hep-ph/9311350].

[18] E. Laermann and O. Philipsen, *The Status of lattice QCD at finite temperature*, *Ann. Rev. Nucl. Part. Sci.* **53** (2003) 163–198, [hep-ph/0303042].

[19] P. de Forcrand, *Simulating QCD at finite density*, *PoS* **LAT2009** (2009) 010, [arXiv:1005.0539].

[20] O. Philipsen, *Lattice QCD at non-zero temperature and baryon density*, in *Les Houches Summer School: Session 93: Modern perspectives in lattice QCD: Quantum field theory and high performance computing*, pp. 273–330, 9, 2010. arXiv:1009.4089.

[21] G. Aarts, E. Seiler, and I.-O. Stamatescu, *The Complex Langevin method: When can it be trusted?*, *Phys. Rev. D* **81** (2010) 054508, [arXiv:0912.3360].

[22] G. Aarts, F. A. James, E. Seiler, and I.-O. Stamatescu, *Complex Langevin: Etiology and Diagnostics of its Main Problem*, *Eur. Phys. J. C* **71** (2011) 1756, [arXiv:1101.3270].

[23] R. V. Gavai and S. Gupta, *Pressure and nonlinear susceptibilities in QCD at finite chemical potentials*, *Phys. Rev. D* **68** (2003) 034506, [hep-lat/0303013].

[24] C. R. Allton, S. Ejiri, S. J. Hands, O. Kaczmarek, F. Karsch, E. Laermann, C. Schmidt, and L. Scorzato, *The QCD thermal phase transition in the presence of a small chemical potential*, *Phys. Rev. D* **66** (2002) 074507, [hep-lat/0204010].

[25] C. R. Allton, M. Doring, S. Ejiri, S. J. Hands, O. Kaczmarek, F. Karsch, E. Laermann, and K. Redlich, *Thermodynamics of two flavor QCD to sixth order in quark chemical potential*, *Phys. Rev. D* **71** (2005) 054508, [hep-lat/0501030].

[26] P. de Forcrand and O. Philipsen, *The QCD phase diagram for small densities from imaginary chemical potential*, *Nucl. Phys. B* **642** (2002) 290–306, [hep-lat/0205016].

[27] J. Langelage, S. Lottini, and O. Philipsen, *Centre symmetric 3d effective actions for thermal SU(N) Yang-Mills from strong coupling series*, *JHEP* **02** (2011) 057, [arXiv:1010.0951]. [Erratum: JHEP 07, 014 (2011)].

[28] M. Fromm, J. Langelage, S. Lottini, and O. Philipsen, *The QCD deconfinement transition for heavy quarks and all baryon chemical potentials*, *JHEP* **01** (2012) 042, [arXiv:1111.4953].

[29] J. Langelage, M. Neuman, and O. Philipsen, *Heavy dense QCD and nuclear matter from an effective lattice theory*, *JHEP* **09** (2014) 131, [arXiv:1403.4162].

[30] J. Glesaaen, M. Neuman, and O. Philipsen, *Equation of state for cold and dense heavy QCD*, *JHEP* **03** (2016) 100, [arXiv:1512.05195].

[31] J. Kim, A. Q. Pham, O. Philipsen, and J. Scheunert, *The Yang-Mills deconfinement transition from a high temperature expansion*, *PoS* **LATTICE2019** (2019) 065, [arXiv:1912.01705].

[32] J. Kim, A. Q. Pham, O. Philipsen, and J. Scheunert, *The SU(3) spin model with chemical potential by series expansion techniques*, *JHEP* **10** (2020) 051, [arXiv:2007.04187].

[33] O. Philipsen and J. Scheunert, *QCD in the heavy dense regime for general N_c: on the existence of quarkyonic matter*, *JHEP* **11** (2019) 022, [arXiv:1908.03136].

[34] P. Butera, M. Comi, and G. Marchesini, *A New Algorithm for High Temperature Series: The Planar Rotator Model*, *Phys. Rev. B* **33** (1986) 4725–4733.

[35] C. Domb, M. Green, and J. Lebowitz, *Phase Transitions and Critical Phenomena*. No. Bd. 3 in Phase Transitions and Critical Phenomena. Academic Press, 1972.

[36] J. Oitmaa, C. Hamer, and W. Zheng, *Series expansion methods for strongly interacting lattice models*. Cambridge University Press, 2006.

[37] D. J. Gross and F. Wilczek, *Ultraviolet Behavior of Nonabelian Gauge Theories*, *Phys. Rev. Lett.* **30** (1973) 1343–1346.

[38] H. Politzer, *Reliable Perturbative Results for Strong Interactions?*, *Phys. Rev. Lett.* **30** (1973) 1346–1349.

[39] S. R. Coleman and D. J. Gross, *Price of asymptotic freedom*, *Phys. Rev. Lett.* **31** (1973) 851–854.

[40] D. Gross and F. Wilczek, *Asymptotically Free Gauge Theories - I*, *Phys. Rev. D* **8** (1973) 3633–3652.

[41] H. Georgi and H. Politzer, *Electroproduction scaling in an asymptotically free theory of strong interactions*, *Phys. Rev. D* **9** (1974) 416–420.

[42] T. Appelquist and H. Politzer, *Orthocharmonium and e+ e- Annihilation*, *Phys. Rev. Lett.* **34** (1975) 43.

[43] A. De Rujula and S. Glashow, *Is Bound Charm Found?*, *Phys. Rev. Lett.* **34** (1975) 46–49.

[44] G. Endrodi, *QCD thermodynamics with dynamical fermions*. PhD thesis, Eötvös Loránd University, 4, 2011. arXiv:1104.3730.

[45] K. G. Wilson, *Confinement of Quarks*, *Phys. Rev. D* (1974) 45–59.

[46] M. Creutz, *Monte Carlo Study of Quantized SU(2) Gauge Theory*, *Phys. Rev. D* **21** (1980) 2308–2315.

[47] L. D. McLerran and B. Svetitsky, *A Monte Carlo Study of SU(2) Yang-Mills Theory at Finite Temperature*, .

[48] C. Gattringer and C. B. Lang, *Quantum chromodynamics on the lattice*, *Lect. Notes Phys.* **788** (2010) 1–343.

[49] M. Creutz, *Quarks, gluons and lattices*. Cambridge Monographs on Mathematical Physics. Cambridge Univ. Press, Cambridge, UK, 6, 1985.

[50] I. Montvay and G. Munster, *Quantum fields on a lattice*. Cambridge Monographs on Mathematical Physics. Cambridge University Press, 3, 1997.

[51] H. B. Nielsen and M. Ninomiya, *No Go Theorem for Regularizing Chiral Fermions*, *Phys. Lett. B* **105** (1981) 219–223.

[52] P. H. Ginsparg and K. G. Wilson, *A Remnant of Chiral Symmetry on the Lattice*, *Phys. Rev. D* **25** (1982) 2649.

[53] K. Symanzik, *Continuum Limit and Improved Action in Lattice Theories. 1. Principles and phi**4 Theory*, *Nucl. Phys. B* **226** (1983) 187–204.

[54] K. Symanzik, *Continuum Limit and Improved Action in Lattice Theories. 2. O(N) Nonlinear Sigma Model in Perturbation Theory*, *Nucl. Phys. B* **226** (1983) 205–227.

[55] B. Sheikholeslami and R. Wohlert, *Improved Continuum Limit Lattice Action for QCD with Wilson Fermions*, *Nucl. Phys. B* **259** (1985) 572.

[56] R. Feynman, A. Hibbs, and D. Styer, *Quantum Mechanics and Path Integrals*. Dover Books on Physics. Dover Publications, 2010.

[57] E. S. Abers and B. W. Lee, *Gauge Theories*, *Phys. Rept.* **9** (1973) 1–141.

[58] L. D. Faddeev and V. N. Popov, *Feynman Diagrams for the Yang-Mills Field*, *Phys. Lett. B* **25** (1967) 29–30.

[59] B. Brandt, *Lectures on lattice gauge theory*. Goethe University Frankfurt, 2019.

[60] C. G. Callan, Jr., *Broken scale invariance in scalar field theory*, *Phys. Rev. D* **2** (1970) 1541–1547.

[61] K. Symanzik, *Small distance behavior in field theory and power counting*, *Commun. Math. Phys.* **18** (1970) 227–246.

[62] S. Capitani, *Lattice perturbation theory*, *Phys. Rept.* **382** (2003) 113–302, [hep-lat/0211036].

[63] P. Weisz, *Renormalization and lattice artifacts*, in *Les Houches Summer School: Session 93: Modern perspectives in lattice QCD: Quantum field theory and high performance computing*, pp. 93–160, 4, 2010. arXiv:1004.3462.

[64] J. I. Kapusta and C. Gale, *Finite-temperature field theory: Principles and applications*. Cambridge Monographs on Mathematical Physics. Cambridge University Press, 2011.

[65] H. Satz, *Extreme states of matter in strong interaction physics. An introduction*, vol. 841. Springer Verlag, New York, 2012.

[66] P. Hasenfratz and F. Karsch, *Chemical Potential on the Lattice*, *Phys. Lett. B* **125** (1983) 308–310.

[67] M. Cheng et al., *The QCD equation of state with almost physical quark masses*, *Phys. Rev. D* **77** (2008) 014511, [arXiv:0710.0354].

[68] R. V. Gavai, S. Gupta, and S. Mukherjee, *The Speed of sound and specific heat in the QCD plasma: Hydrodynamics, fluctuations and conformal symmetry*, *Phys. Rev. D* **71** (2005) 074013, [hep-lat/0412036].

[69] H.-T. Ding, F. Karsch, and S. Mukherjee, *Thermodynamics of strong-interaction matter from Lattice QCD*, *Int. J. Mod. Phys. E* **24** (2015), no. 10 1530007, [arXiv:1504.05274].

[70] O. Philipsen, *The QCD equation of state from the lattice*, *Prog. Part. Nucl. Phys.* **70** (2013) 55–107, [arXiv:1207.5999].

[71] B. Brandt, *Chiral properties of two-flavor QCD at zero and non-zero temperature*. PhD Thesis-University Mainz, 9, 2012.

[72] L. D. McLerran and B. Svetitsky, *Quark Liberation at High Temperature: A Monte Carlo Study of SU(2) Gauge Theory*, *Phys. Rev. D* **24** (1981) 450.

[73] G. 't Hooft, *A Property of Electric and Magnetic Flux in Nonabelian Gauge Theories*, *Nucl. Phys. B* **153** (1979) 141–160.

[74] K. Osterwalder and E. Seiler, *Gauge Field Theories on the Lattice*, *Annals Phys.* **110** (1978) 440.

[75] C. Itzykson and J. M. Drouffe, *Statistical field theory. Vol. 2*. Cambridge Monographs on Mathematical Physics. CUP, 1989.

[76] J.-M. Drouffe and J.-B. Zuber, *Strong Coupling and Mean Field Methods in Lattice Gauge Theories*, *Phys. Rept.* **102** (1983) 1.

[77] H. Weyl, *The Classical Groups: Their Invariants and Representations*. Princeton University Press, 2016.

[78] A. A. Migdal, *Recursion Equations in Gauge Theories*, *Sov. Phys. JETP* **42** (1975) 413.

[79] B. Svetitsky and L. G. Yaffe, *Critical Behavior at Finite Temperature Confinement Transitions*, *Nucl. Phys. B* **210** (1982) 423–447.

[80] G. Bergner, J. Langelage, and O. Philipsen, *Numerical corrections to the strong coupling effective Polyakov-line action for finite T Yang-Mills theory*, *JHEP* **11** (2015) 010, [arXiv:1505.01021].

[81] M. Neuman, *Effective theory for heavy quark QCD at finite temperature and density with stochastic quantization*. PhD Thesis-Goethe University Frankfurt, 2015.

[82] F. Green and F. Karsch, *Mean Field Analysis of SU(N) Deconfining Transitions in the Presence of Dynamical Quarks*, *Nucl. Phys. B* **238** (1984) 297–306.

[83] J. Glesaaen, *Heavy quark QCD at finite temperature and density using an effective theory.* PhD Thesis-Goethe University Frankfurt, 2016.

[84] J. Glesaaen, *hopping-large-nt: First release*, *Zenodo* (2016).

[85] A. S. Christensen, J. C. Myers, and P. D. Pedersen, *Large N lattice QCD and its extended strong-weak connection to the hypersphere*, *JHEP* **02** (2014) 028, [arXiv:1312.3519].

[86] M. Sykes, J. Essam, B. Heap, and B. Hiley, *Lattice constant systems and graph theory*, *Journal of Mathematical Physics* **7** (1966), no. 9 1557–1572.

[87] J. W. Essam and M. E. Fisher, *Some Basic Definitions in Graph Theory*, *Rev. Mod. Phys.* **42** (1970) 271–288.

[88] M. Sykes, *Some counting theorems in the theory of the ising model and the excluded volume problem*, *Journal of Mathematical Physics* **2** (1961), no. 1 52–62.

[89] O. Ore, *Theory of Graphs.* American Mathematical Society colloquium publications. American Mathematical Society, 1962.

[90] C. Gattringer, *Flux representation of an effective Polyakov loop model for QCD thermodynamics*, *Nucl. Phys. B* **850** (2011) 242–252, [arXiv:1104.2503].

[91] A. Guttman, *Asymptotic analysis of power-series expansions*, *Phase transitions and critical phenomena* (1989).

[92] G. A. Baker, G. A. Baker Jr, P. Graves-Morris, G. Baker, and S. S. Baker, *Pade Approximants: Encyclopedia of Mathematics and It's Applications, Vol. 59 George A. Baker, Jr., Peter Graves-Morris*, vol. 59. Cambridge University Press, 1996.

[93] J. Chisholm, *Rational approximants defined from double power series*, *Mathematics of Computation* **27** (1973), no. 124 841–848.

[94] J. Chisholm and R. H. Jones, *Relative scale covariance of n-variable approximants*, *Proceedings of the Royal Society of London. A. Mathematical and Physical Sciences* **344** (1975), no. 1639 465–470.

[95] J. Chisholm and P. Graves-Morris, *Generalizations of the theorem of de montessus to two-variable approximants*, *Proceedings of the Royal Society of London. A. Mathematical and Physical Sciences* **342** (1975), no. 1630 341–372.

[96] M. Newman and G. Barkema, *Monte Carlo Methods in Statistical Physics.* Clarendon Press, 1999.

[97] S. Duane, A. D. Kennedy, B. J. Pendleton, and D. Roweth, *Hybrid Monte Carlo*, *Phys. Lett. B* **195** (1987) 216–222.

[98] C. Morningstar and M. J. Peardon, *Analytic smearing of SU(3) link variables in lattice QCD*, *Phys. Rev. D* **69** (2004) 054501, [hep-lat/0311018].

[99] M. Luscher, *Schwarz-preconditioned HMC algorithm for two-flavour lattice QCD*, *Comput. Phys. Commun.* **165** (2005) 199–220, [hep-lat/0409106].

[100] Z. Fodor and S. D. Katz, *Critical point of QCD at finite T and mu, lattice results for physical quark masses*, *JHEP* **04** (2004) 050, [hep-lat/0402006].

[101] M. D'Elia and M.-P. Lombardo, *Finite density QCD via imaginary chemical potential*, *Phys. Rev. D* **67** (2003) 014505, [hep-lat/0209146].

[102] C. R. Allton, S. Ejiri, S. J. Hands, O. Kaczmarek, F. Karsch, E. Laermann, and C. Schmidt, *The Equation of state for two flavor QCD at nonzero chemical potential*, *Phys. Rev. D* **68** (2003) 014507, [hep-lat/0305007].

[103] J. R. Klauder, *Stochastic quantization*, *Acta Phys. Austriaca Suppl.* **25** (1983) 251–281.

[104] G. Parisi, *On complex probabilities*, *Phys. Lett. B* **131** (1983) 393–395.

[105] G. Parisi and Y.-s. Wu, *Perturbation Theory Without Gauge Fixing*, *Sci. Sin.* **24** (1981) 483.

[106] E. Seiler, D. Sexty, and I.-O. Stamatescu, *Gauge cooling in complex Langevin for QCD with heavy quarks*, *Phys. Lett. B* **723** (2013) 213–216, [arXiv:1211.3709].

[107] B. Efron and R. J. Tibshirani, *An Introduction to the Bootstrap*. No. 57 in Monographs on Statistics and Applied Probability. Chapman & Hall/CRC, Boca Raton, Florida, USA, 1993.

[108] A. Sciarra, *The QCD phase diagram at purely imaginary chemical potential from the lattice*. PhD thesis, Johann Wolfgang Goethe Universität, 2016.

[109] H. Stanley, *Introduction to Phase Transitions and Critical Phenomena*. International series of monographs on physics. Oxford University Press, 1971.

[110] J. Kim, A. Q. Pham, and O. Philipsen, *Deconfinement critical point of a heavy quark effective lattice theories*, in *38th International Symposium on Lattice Field Theory*, 12, 2021. arXiv:2112.06505.

[111] M. Hellmund and W. Janke, *High-temperature series expansions for the q-state Potts model on a hypercubic lattice and critical properties of percolation*, *Phys. Rev. E* **74** (2006) 051113, [cond-mat/0607423].

[112] J. Fingberg, U. M. Heller, and F. Karsch, *Scaling and asymptotic scaling in the SU(2) gauge theory*, *Nucl. Phys. B* **392** (1993) 493–517, [hep-lat/9208012].

[113] M. G. Alford, S. Chandrasekharan, J. Cox, and U. J. Wiese, *Solution of the complex action problem in the Potts model for dense QCD*, *Nucl. Phys. B* **602** (2001) 61–86, [hep-lat/0101012].

[114] S. Kim, P. de Forcrand, S. Kratochvila, and T. Takaishi, *The 3-state Potts model as a heavy quark finite density laboratory*, *PoS* **LAT2005** (2006) 166, [hep-lat/0510069].

[115] **WHOT-QCD** Collaboration, S. Ejiri and et al., *End point of the first-order phase transition of QCD in the heavy quark region by reweighting from quenched QCD*, *Phys. Rev. D* **101** (2020), no. 5 054505, [arXiv:1912.10500].

[116] P. Butera and M. Comi, *Critical universality and hyperscaling revisited for Ising models of general spin using extended high temperature series*, *Phys. Rev. B* **65** (2002) 144431, [hep-lat/0112049].

[117] P. de Forcrand and O. Philipsen, *The Chiral critical point of N(f) = 3 QCD at finite density to the order (mu/T)**4*, *JHEP* **11** (2008) 012, [arXiv:0808.1096].

[118] M. D'Elia and F. Sanfilippo, *Thermodynamics of two flavor QCD from imaginary chemical potentials*, *Phys. Rev. D* **80** (2009) 014502, [arXiv:0904.1400].

[119] P. de Forcrand and O. Philipsen, *Constraining the QCD phase diagram by tricritical lines at imaginary chemical potential*, *Phys. Rev. Lett.* **105** (2010) 152001, [arXiv:1004.3144].

[120] A. Roberge and N. Weiss, *Gauge Theories With Imaginary Chemical Potential and the Phases of QCD*, *Nucl. Phys. B* **275** (1986) 734–745.

[121] C. Czaban, F. Cuteri, O. Philipsen, C. Pinke, and A. Sciarra, *Roberge-Weiss transition in $N_f = 2$ QCD with Wilson fermions and $N_\tau = 6$*, *Phys. Rev. D* **93** (2016), no. 5 054507, [arXiv:1512.07180].

[122] O. Philipsen and C. Pinke, *Nature of the Roberge-Weiss transition in $N_f = 2$ QCD with Wilson fermions*, *Phys. Rev. D* **89** (2014), no. 9 094504, [arXiv:1402.0838].

[123] M. Salg, *The deconfinement transition in an effective theory for heavy quark lattice QCD to $\mathcal{O}(\kappa^4)$*. Master thesis, Johann Wolfgang Goethe Universität, 2020.

[124] K. Binder, *Finite size scaling analysis of Ising model block distribution functions*, *Z. Phys. B* **43** (1981) 119–140.

[125] C. Bonati, G. Cossu, M. D'Elia, and F. Sanfilippo, *The Roberge-Weiss endpoint in N_f = 2 QCD*, *Phys. Rev. D* **83** (2011) 054505, [arXiv:1011.4515].

[126] O. Philipsen and A. Sciarra, *Finite Size and Cut-Off Effects on the Roberge-Weiss Transition in $N_f = 2$ QCD with Staggered Fermions*, *Phys. Rev. D* **101** (2020), no. 1 014502, [arXiv:1909.12253].

[127] A. Pelissetto and E. Vicari, *Critical phenomena and renormalization group theory*, *Phys. Rept.* **368** (2002) 549–727, [cond-mat/0012164].

[128] F. Cuteri, O. Philipsen, A. Schön, and A. Sciarra, *Deconfinement critical point of lattice QCD with N_f=2 Wilson fermions*, *Phys. Rev. D* **103** (2021), no. 1 014513, [arXiv:2009.14033].

[129] A. M. Ferrenberg and R. H. Swendsen, *Optimized Monte Carlo analysis*, *Phys. Rev. Lett.* **63** (1989) 1195–1198.

[130] A. M. Ferrenberg and R. H. Swendsen, *New Monte Carlo Technique for Studying Phase Transitions*, *Phys. Rev. Lett.* **61** (1988) 2635–2638.

[131] K. Zhou, G. Endrődi, L.-G. Pang, and H. Stöcker, *Regressive and generative neural networks for scalar field theory*, *Phys. Rev. D* **100** (2019), no. 1 011501, [arXiv:1810.12879].

[132] Y. Mori, K. Kashiwa, and A. Ohnishi, *Application of a neural network to the sign problem via the path optimization method*, *PTEP* **2018** (2018), no. 2 023B04, [arXiv:1709.03208].

[133] M. Creutz, *On invariant integration over SU(N)*, *J. Math. Phys.* **19** (1978) 2043.